

SELECTIVE ETCHING OF COMPOUND SEMICONDUCTORS

BY

DAVID C. HAYS

A THESIS PRESENTED TO THE GRADUATE SCHOOL  
OF THE UNIVERSITY OF FLORIDA IN PARTIAL FULFILLMENT  
OF THE REQUIREMENTS FOR THE DEGREE OF  
MASTER OF SCIENCE

UNIVERSITY OF FLORIDA

1999

## ACKNOWLEDGEMENTS

I would first like to thank my advisor, Dr. Stephen J. Pearton, for giving me the chance to continue my education under such a dynamic and well respected researcher. His support, advice, and guidance are greatly appreciated and are the foundation for this work.

I would also like to thank my committee members, Dr. Cammy R. Abernathy and Dr. Rajiv K. Singh, for their expert help, suggestions, and time.

I wish to thank the members, past and present, of the Pearton and Abernathy research groups for their friendship, cooperation, and time.

Finally, I would like to thank my parents whose love, guidance, and support carried me through both the good times and the bad. This work would not be possible without them.

Funding for this research was provided by the National Science Foundation.

## TABLE OF CONTENTS

	<u>Page</u>
ACKNOWLEDGEMENTS .....	ii
LIST OF TABLES .....	v
LIST OF FIGURES .....	vi
ABSTRACT .....	xiii
CHAPTERS	
1 INTRODUCTION .....	1
2 REVIEW OF LITERATURE .....	5
2.1 Wet Etching .....	5
2.2 Dry Etching .....	8
3 WET ETCHING OF THE GaAs/AlGaAs SYSTEM .....	26
3.1 Materials and Methods .....	26
3.2 Results and Discussion .....	27
4 DRY ETCHING OF GaAs/AlGaAs/InGaP .....	39
4.1 Materials and Methods .....	39
4.2 Results and Discussion .....	39
5 DRY ETCHING OF InN/GaN/AlN .....	68
5.1 Materials and Methods .....	68
5.2 Results and Discussion .....	68
6 HIGH RATE DRY ETCHING OF Si .....	99

6.1 Materials and Methods .....	99
6.2 Results and Discussion .....	100
7 SUMMARY .....	115
LIST OF REFERENCES .....	118
BIOGRAPHICAL SKETCH .....	123

## LIST OF TABLES

<u>Table</u>	<u>Page</u>
1. Important reactions in a plasma .....	10
2. Dry etch selectivities for GaAs/AlGaAs and GaAs/InGaP under conventional RIE conditions and under high density plasma conditions in different plasma chemistries .....	67
3. Average bond energies for feedstock gases .....	102

## LIST OF FIGURES

<u>Figure</u>	<u>page</u>
1. Schematic of a simplified plasma etch reactor .....	13
2. Potential distribution in a parallel-plate plasma reactor .....	16
3. The four basic mechanisms of plasma etching .....	18
4. Schematic of a typical Inductively Coupled Plasma (ICP) reactor .....	25
5. Etch rates of GaAs and AlGaAs at 21°C as a function of the ratio of citric acid to hydrogen peroxide .....	28
6. Etch rates of GaAs and AlGaAs at 38°C as a function of the ratio of citric acid to hydrogen peroxide .....	29
7. Selectivities of GaAs over AlGaAs at 21°C and 38°C as a function of the ratio of citric acid to hydrogen peroxide .....	30
8. Etch rates of GaAs and AlGaAs in a 3citric acid:1H <sub>2</sub> O <sub>2</sub> solution as a function of temperature .....	32
9. Etch rates of GaAs and AlGaAs in a 8citric acid :1H <sub>2</sub> O <sub>2</sub> solution as a function of temperature .....	33
10. RMS surface roughness for GaAs and AlGaAs at 21°C as a function of the ratio of citric acid to hydrogen peroxide .....	34
11. AFM scans of GaAs(left) and AlGaAs(right) etched in various concentrations of citric acid:H <sub>2</sub> O <sub>2</sub> solutions at 21°C .....	35
12. AES surface scan of unetched AlGaAs .....	36
13. AES surface scan of AlGaAs etched in 20citric acid:1H <sub>2</sub> O <sub>2</sub> .....	37
14. AES depth profile of AlGaAs etched in 20citric acid:1H <sub>2</sub> O <sub>2</sub> .....	3

15. Etch rates of GaAs, AlGaAs, and InGaP(top) and resultant selectivities for GaAs over AlGaAs and InGaP(bottom) as a function of BCl <sub>3</sub> percentage in ICP BCl <sub>3</sub> /SF <sub>6</sub> discharges (200W source power, 50W rf chuck power, 5mTorr) .....	41
16. Etch rates of GaAs, AlGaAs, and InGaP(top) and resultant selectivities for GaAs over AlGaAs and InGaP(bottom) as a function of source power in ICP 12BCl <sub>3</sub> /3SF <sub>6</sub> discharges (50W rf chuck power, 5mTorr) .....	42
17. Etch rates of GaAs, AlGaAs, and InGaP(top) and resultant selectivities for GaAs over AlGaAs and InGaP(bottom) as a function of pressure in ICP 12BCl <sub>3</sub> /3SF <sub>6</sub> discharges (200W source power, 50W rf chuck power) .....	43
18. Etch rates of GaAs, AlGaAs, and InGaP(top) and resultant selectivities for GaAs over AlGaAs and InGaP(bottom) as a function of pressure in RIE 12BCl <sub>3</sub> /3SF <sub>6</sub> discharges (50W rf chuck power) .....	44
19. Etch rates of GaAs, AlGaAs, and InGaP(top) and resultant selectivities for GaAs over AlGaAs and InGaP(bottom) as a function of rf chuck power in ICP 12BCl <sub>3</sub> /3SF <sub>6</sub> discharges (200W source power, 5mTorr) .....	46
20. Etch rates of GaAs, AlGaAs, and InGaP(top) and resultant selectivities for GaAs over AlGaAs and InGaP(bottom) as a function of BCl <sub>3</sub> percentage in ICP BCl <sub>3</sub> /NF <sub>3</sub> discharges (200W source power, 50W rf chuck power, 5mTorr) .....	47
21. Etch rates of GaAs, AlGaAs, and InGaP(top) and resultant selectivities for GaAs over AlGaAs and InGaP(bottom) as a function of source power in ICP 12BCl <sub>3</sub> /3NF <sub>3</sub> discharges (50W rf chuck power, 5mTorr) .....	48
22. Etch rates of GaAs, AlGaAs, and InGaP(top) and resultant selectivities for GaAs over AlGaAs and InGaP(bottom) as a function of pressure in ICP 12BCl <sub>3</sub> /3NF <sub>3</sub> discharges (200W source power, 50W rf chuck power) .....	50
23. Etch rates of GaAs, AlGaAs, and InGaP(top) and resultant selectivities for GaAs over AlGaAs and InGaP(bottom) as a function of rf chuck power in ICP 12BCl <sub>3</sub> /3NF <sub>3</sub> discharges (200W source power, 5mTorr) .....	51

24. AFM scans of InGaP control sample (top), and samples etched in $12\text{BCl}_3/3\text{SF}_6$ (middle), and $12\text{BCl}_3/3\text{NF}_3$ (bottom) (200W source power, 150W rf chuck power, 5mTorr) .....	52
25. AFM scans of GaAs control sample (top), and samples etched in $12\text{BCl}_3/3\text{SF}_6$ (middle), and $12\text{BCl}_3/3\text{NF}_3$ (bottom) (200W source power, 150W rf chuck power, 5mTorr) .....	53
26. AFM scans of AlGaAs control sample (top), and samples etched in $12\text{BCl}_3/3\text{SF}_6$ (middle), and $12\text{BCl}_3/3\text{NF}_3$ (bottom) (200W source power, 150W rf chuck power, 5mTorr) .....	54
27. AES surface scans of GaAs etched in $12\text{BCl}_3/3\text{SF}_6$ (top), and $12\text{BCl}_3/3\text{NF}_3$ (bottom) (0W source power, 50W rf chuck power, 10mTorr) .....	55
28. Etch rates of GaAs, AlGaAs, and InGaP(top) and resultant selectivities for GaAs over AlGaAs and InGaP(bottom) as a function of ICl percentage in ICP ICl/Ar discharges (750W source power, 250W rf chuck power, 5mTorr) .....	57
29. Etch rates of GaAs, AlGaAs, and InGaP(top) and resultant selectivities for GaAs over AlGaAs and InGaP(bottom) as a function of IBr percentage in ICP IBr/Ar discharges (750W source power, 250Wrf chuck power, 5mTorr) .....	58
30. AFM scans of GaAs etched in $2\text{ICl}/13\text{Ar}$ (top) and $2\text{IBr}/13\text{Ar}$ (bottom) (750W source power, 250W rf chuck power, 5mTorr) .....	59
31. AES surface scan (top) and depth profile (bottom) of GaAs etched in $2\text{ICl}/13\text{Ar}$ plasma at 750W source power, 250W rf chuck power and 5mTorr .....	60
32. AES surface scan (top) and depth profile (bottom) of GaAs etched in $2\text{IBr}/13\text{Ar}$ plasma at 750W source power, 250W rf chuck power and 5mTorr .....	61
33. Etch rates of GaAs, AlGaAs, and InGaP(top) and resultant selectivities for GaAs over AlGaAs and InGaP(bottom) as a function of rf chuck power in ICP $2\text{ICl}/13\text{Ar}$ discharges (750W source power, 5mTorr) .....	62
34. Etch rates of GaAs, AlGaAs, and InGaP(top) and resultant selectivities for GaAs over AlGaAs and InGaP(bottom) as a function of rf chuck power in ICP $2\text{IBr}/13\text{Ar}$ discharges (750W source power, 5mTorr) .....	63

35. Etch rates of GaAs and InGaP and resultant selectivity for InGaP over GaAs as a function of BI <sub>3</sub> percentage at 750W source power, 150W rf chuck power(top), source power at fixed rf power of 150W(center) and rf power at fixed ICP power of 750W(bottom) in ICP BI <sub>3</sub> /Ar discharges (5mTorr) .....	65
36. Etch rates of GaAs and InGaP and resultant selectivity for InGaP over GaAs as a function of BBr <sub>3</sub> percentage at 750W source power 250W rf chuck power(top), source power at fixed rf chuck power of 250W(center) and rf power at fixed ICP power of 750W(bottom) in ICP BBr <sub>3</sub> /Ar discharges (5mtorr) .....	66
37. Etch rates of binary nitrides(top) and selectivity for InN over the other two materials(bottom) as a function of ICl percentage in ICP discharges (750W source power, 250W rf chuck power, 5mTorr) .....	69
38. Etch rates of binary nitrides(top) and selectivity for InN over the other two materials(bottom) as a function of source power in ICP discharges (250W rf chuck power, 5mTorr) of 2ICl/13Ar .....	71
39. Etch rates of binary nitrides(top) and selectivity for InN over the other two materials(bottom) as a function of pressure in ICP discharges (750W source power, 250W rf chuck power) of 2ICl/13Ar .....	72
40. Etch rates of binary nitrides(top) and selectivity for InN over the other two materials(bottom) as a function of rf chuck power in ICP discharges (750Wsource power, 5mTorr) of 2ICl/13Ar .....	73
41. Etch rates of binary nitrides(top) and selectivity for InN over the other two materials(bottom) as a function of IBr percentage in ICP discharges (750W source power, 250W rf chuck power, 5mTorr) .....	75
42. Etch rates of binary nitrides(top) and selectivity for InN over the other two materials(bottom) as a function of source power in ICP discharges (250W rf chuck power, 5mTorr) of 2IBr/13Ar .....	76
43. Etch rates of binary nitrides(top) and selectivity for InN over the other two materials(bottom) as a function of pressure in ICP discharges (750W source power, 250W rf chuck power) of 2IBr/13Ar .....	77

44. Etch rates of binary nitrides(top) and selectivity for InN over the other two materials(bottom) as a function of rf chuck power in ICP discharges (750W source power, 5mTorr) of 2IBr/13Ar .....	78
45. AFM scans for GaN etched in 2ICl/13Ar (top) and 2IBr/13Ar (bottom) (750 W source power, 250W rf chuck power, 5mTorr) .....	79
46. AES surface scan (top) and depth profile (bottom) of GaN (2ICl/13Ar, 750W source power, 250W rf chuck power, 5mTorr) .....	81
47. Effect of chlorine concentration on etch rates of InN (top) and AlN (b) with Cl <sub>2</sub> /He, Cl <sub>2</sub> /Ar and Cl <sub>2</sub> /Xe plasma chemistries (750 W source power, 250 W rf chuck power, 5 mTorr) .....	82
48. Effect of chlorine concentration on etch rates of GaN (top) and on dc bias and ion flux at the sheath edge (bottom) with Cl <sub>2</sub> /He, Cl <sub>2</sub> /Ar and Cl <sub>2</sub> /Xe plasma chemistries (750 W source power, 250 W rf chuck power, 5 mTorr) .....	83
49. Effect of rf chuck power on etch rates of InN (top) and AlN (bottom) with 2Cl <sub>2</sub> /13He, 2Cl <sub>2</sub> /13Ar and 2Cl <sub>2</sub> /13Xe plasma chemistries (750 W source power, 5 mTorr) .....	85
50. Effect of rf chuck power on etch rates of GaN (top) and on dc bias and ion flux at the sheath edge (bottom) with 2Cl <sub>2</sub> /13He, 2Cl <sub>2</sub> /13Ar and 2Cl <sub>2</sub> /13Xe plasma chemistries (750 W source power, 5 mTorr) .....	86
51. Effect of rf chuck power on the ion fluxes generated by capacitive discharge and inductively coupled discharge with 2Cl <sub>2</sub> /13He, 2Cl <sub>2</sub> /13Ar and 2Cl <sub>2</sub> /13 Xe plasma chemistries (750 W source power, 5 mTorr) .....	89
52. Effect of ICP source power on etch rates of InN (top) and AlN (bottom) with 2Cl <sub>2</sub> /13 He, 2Cl <sub>2</sub> /13Ar and 2Cl <sub>2</sub> /13Xe plasma chemistries (250 W rf chuck power, 5 mTorr) .....	90
53. Effect of ICP source power on etch rates of GaN (top) and on dc bias and ion flux at the sheath edge (bottom) with 2Cl <sub>2</sub> /13He, 2Cl <sub>2</sub> /13Ar and 2Cl <sub>2</sub> /13Xe plasma chemistries (250 W rf chuck power, 5 mTorr) .....	91

54. Effect of chlorine concentration on the selectivity for InN over GaN (top) and AlN (bottom) (750 W source power, 250 W rf chuck power, 5 mTorr) .....	93
55. Effect of rf chuck power on the selectivity for InN over GaN (top) and AlN (bottom) (750 W source power, 5 mTorr, 2Cl <sub>2</sub> /13noble gas) .....	94
56. Effect of ICP source power on the selectivity for InN over GaN (top) and AlN (bottom) (250 W rf chuck power, 5 mTorr, 2Cl <sub>2</sub> /13noble gas) .....	95
57. AFM scans of GaN etched with Cl <sub>2</sub> /He (top), Cl <sub>2</sub> /Ar (middle), and Cl <sub>2</sub> /Xe (bottom) at 750W source power, 250W rf chuck power, and 5mTorr .....	97
58. AES surface scans of GaN etched in Cl <sub>2</sub> /He (top), Cl <sub>2</sub> /Ar (middle), and Cl <sub>2</sub> /Xe (bottom) at 750W source power, 250W rf chuck power, and 5mTorr .....	98
59. Si etch rate (top) and etch yield (bottom) as a function of ICP source power in pure SF <sub>6</sub> , NF <sub>3</sub> , PF <sub>5</sub> , or BF <sub>3</sub> discharges (35mTorr, 0W rf chuck power) .....	101
60. Si etch rate (top) and etch yield (bottom) as a function of ICP source power in pure SF <sub>6</sub> , NF <sub>3</sub> , PF <sub>5</sub> , or BF <sub>3</sub> discharges (35mTorr, 5W rf chuck power) .....	103
61. OES spectra from BF <sub>3</sub> (top) and PF <sub>5</sub> (bottom) discharges during etching of Si .....	105
62. OES spectra from NF <sub>3</sub> (top) and SF <sub>6</sub> (bottom) discharges during etching of Si .....	106
63. SEM micrographs of Si surfaces after etching in SF <sub>6</sub> (top left), NF <sub>3</sub> (top right), PF <sub>5</sub> (bottom left), and BF <sub>3</sub> (bottom right) .....	107
64. AFM scans of Si surfaces before and after etching in SF <sub>6</sub> , NF <sub>3</sub> , PF <sub>5</sub> , and BF <sub>3</sub> .....	108
65. RMS roughness of Si surfaces after etching in SF <sub>6</sub> , NF <sub>3</sub> , PF <sub>5</sub> , and BF <sub>3</sub> .....	110
66. AES surface scans of Si before (top) and after SF <sub>6</sub> (center) or NF <sub>3</sub> (bottom) etching .....	111

67. Si etch rate as a function of Pressure (top), rf power (middle), and ICP power (bottom) in $\text{NF}_3$ discharges .....	112
68. AFM scans of Si surfaces before (top) and after (center and bottom) $\text{NF}_3$ etching without (center) or with (bottom) rf biasing of the chuck position .....	114

Abstract of Thesis Presented to the Graduate School  
of the University of Florida in Partial Fulfillment of the  
Requirements for the Degree of Master of Science

## SELECTIVE ETCHING OF COMPOUND SEMICONDUCTORS

By

David Hays

August, 1999

Chairman: Stephen J. Pearton  
Major Department: Materials Science and Engineering

The etching characteristics of GaAs and AlGaAs in citric acid/hydrogen peroxide ( $C_6H_8O_7/H_2O_2$ ) etching solution at volume ratios of 1:1 to 50:1 were studied. The results show that by varying the concentration of the solution we can vary the selectivity from over 70:1 to a reverse selectivity of 1:1.3. Etching with low citric acid to  $H_2O_2$  ratios is diffusion limited for AlGaAs with an activation energy of 6.33 kcal/mol, but it is reaction-limited for GaAs with an activation energy of 13.7 kcal/mol. However, etching with high citric acid to  $H_2O_2$  ratios is reaction-limited for both GaAs and AlGaAs with activation energies of 11.3 kcal/mol and 13.13 kcal/mol, respectively.

Selective etching of GaAs over AlGaAs and InGaP was also examined in different plasma chemistries ( $BCl_3/SF_6$ ,  $BCl_3/NF_3$ , IBr, ICl,  $BI_3$ , and  $BBr_3$ ) in a high density plasma reactor. The normal etch stop reactions involving formation of involatile  $AlF_3$ ,  $InF_3$ , or  $InCl_3$  are found to be less effective under high density conditions because of the higher ion-assisted etch product desorption efficiency. Addition of  $SF_6$  to  $BCl_3$

produces higher selectivities than  $\text{NF}_3$  as an additive, while  $\text{IBr}$ ,  $\text{ICl}$  and  $\text{BBr}_3$  are essentially non-selective for both heterostructure systems. Selective etching of  $\text{InGaP}$  over  $\text{GaAs}$  is achieved using the  $\text{BI}_3$  chemistry.

Two interhalogen chemistries,  $\text{ICl}$  and  $\text{IBr}$ , as well as  $\text{He}$ ,  $\text{Ar}$ , and  $\text{Xe}$  additives to chlorine based chemistries were examined for selective dry etching of  $\text{InN}$  over  $\text{GaN}$  and  $\text{AlN}$ . Maximum selectivities of 55 for  $\text{InN}/\text{GaN}$  and 20 for  $\text{InN}/\text{AlN}$  were achieved with  $\text{ICl}$ , and 30 for  $\text{InN}/\text{GaN}$  and 14 for  $\text{InN}/\text{AlN}$ , respectively, with  $\text{IBr}$ . There are two reasons for these results – the relatively high volatility of the  $\text{InI}_3$  etch product and the lower bond strength of  $\text{InN}$  relative to the other two binary nitrides. Both interhalogen plasma chemistries appear promising for use in electronic device fabrication. It was confirmed that the efficient breaking of the III-nitrogen bond is crucial for higher etch rates. The  $\text{InN}$  etching was dominated by physical sputtering;  $\text{GaN}$  and  $\text{AlN}$  etch rates were limited by initial breaking of the III-nitrogen bond. Maximum selectivities of  $\sim 80$  for  $\text{InN}$  over  $\text{GaN}$  and  $\text{AlN}$  were obtained with the  $\text{Cl}_2$ -based discharges.

Four different  $\text{F}_2$ -based gases ( $\text{SF}_6$ ,  $\text{NF}_3$ ,  $\text{PF}_5$ , and  $\text{BF}_3$ ) were examined for high rate Inductively Coupled Plasma etching of  $\text{Si}$ . Etch rates up to  $\sim 8\mu\text{m}/\text{min}$  were achieved with pure  $\text{SF}_6$  discharges at high source power (1500W) and pressure (35mTorr). A direct comparison of the four feedstock gases under the same plasma conditions showed the  $\text{Si}$  etch rate to increase in the order  $\text{BF}_3 < \text{NF}_3 < \text{PF}_5 < \text{SF}_6$ . This is in good correlation with the average bond energies of the gases, except for  $\text{NF}_3$ , which is the least strongly bound. Optical emission spectroscopy showed that the ICP source efficiently dissociated  $\text{NF}_3$ , but the etched  $\text{Si}$  surface morphologies were significantly worse with this gas than with the other 3 gases.









## CHAPTER 2 REVIEW OF LITERATURE

### 2.1 Wet Etching

#### 2.1.1 General Principles of Wet Etching

The term *etching* is used to describe any technique by which material can be uniformly removed from a wafer, or locally removed as in the transfer of patterns during fabrication of a microcircuit.<sup>(45)</sup> The basic mechanism of wet chemical etches of semiconductors is the formation of an oxide, or oxides on the surface, and the subsequent dissolution of the oxidized products by either acids or bases.<sup>(46)</sup> Wet chemical etching of any material can be thought of as a sequence of five steps:<sup>(45)</sup>

- 1) Transport of the reactant to the surface
- 2) Adsorption of the reactant
- 3) Reaction at the surface
- 4) Desorption of reaction products
- 5) Removal of reaction products away from the surface

Each of these three steps can function as a rate limiter and dominate the entire process. If the etch rate is controlled by the rate at which the reactant species can reach the surface, or the rate at which the reaction products are removed, the process is said to be diffusion-limited. If the etch rate is only limited by the rate of chemical reactions at

the surface then the process is said to be reaction-rate limited.<sup>(47)</sup> Some distinctions between the two rate limiting steps are as follows:

The attributes of diffusion controlled reactions are

- 1) The activation energy is viscosity controlled, 1-6 kcal/mol
- 2) The reaction rate increases with agitation
- 3) All substances and crystal orientations etch at the same rate
- 4) The activation energy increases with stirring
- 5) The etch depth is proportional to the square root of etch time

The attributes of reaction-rate controlled reactions are

- 1) The rate changes with etchant concentration
- 2) The rate is not sensitive to agitation
- 3) The activation energy is typically 8-20 kcal/mol
- 4) The etch depth is linearly dependent on etch time

As with all chemical reactions, etching is sensitive to temperature. A 10°C increase in temperature can increase the etch rate by as much as a factor of two. Another consideration is the aging of etchant solutions. Some solutions may change composition over time, depending on temperature and storage. All of these factors must be considered in establishing reproducible and controllable etching processes.<sup>(47)</sup>

### 2.1.2 Etching Solutions for GaAs

Many etchants have been reported for GaAs, however, very few of them are isotropic. This is because the surface activity of the Ga and As faces is quite different. The As face, terminated on arsenic, has two unsatisfied bonds per atom. Consequently,

although some reconstruction occurs in the surface layer, it is still more reactive than the Ga face, and thus etches at a faster rate. As a result, most etches give a polished surface on the As face. The Ga face etches much slower, because it has no unsatisfied bonds, and tends to show up surface features and crystallographic defects. Almost any combination of oxidizer and oxide-dissolver will operate as an etchant. In most GaAs etchants the oxidizer is  $\text{H}_2\text{O}_2$ . The acid is generally one of the more common ones, such as  $\text{H}_3\text{PO}_4$ ,  $\text{HNO}_3$ ,  $\text{H}_2\text{SO}_4$ ,  $\text{HCl}$ , or  $\text{C}_6\text{H}_8\text{O}_7$ . Ammonium hydroxide-hydrogen peroxide mixtures are also popular because of the controlled etch rate of  $\sim 3000 \text{ \AA}/\text{min}$  for a 1ml  $\text{NH}_4\text{OH}$ :700ml  $\text{H}_2\text{O}_2$  solution. There are also mixtures that exhibit strong anisotropy.<sup>(45)</sup>

The  $\text{H}_2\text{SO}_4 / \text{H}_2\text{O}_2$  system is widely used and is often referred to as *Caro's etch*. Sulfuric acid is highly viscous, so that diffusion-limited etching occurs with high concentrations of this acid and are useful for polishing. More dilute mixtures have a reaction-rate limited behavior and are useful in mesa etching or gate recessing.<sup>(45, 47)</sup>

The  $\text{H}_3\text{PO}_4 / \text{H}_2\text{O}_2$  etchants tend to be polishing because phosphoric acid is also quite viscous. For most of the composition ranges the etch rate is linearly dependent on time, but for high phosphoric acid solutions there may be a square root dependence on time.

The  $\text{HCl}$  based systems are characterized by a tendency to form etch profiles that have curved surfaces rather than straight planes.  $\text{HCl}$  based systems are interesting because, unlike most other GaAs etchants, they can provide nearly isotropic etching or minimal mask undercut, but not both simultaneously. Low concentration  $\text{HCl}$  etchants tend to be isotropic, while high concentration  $\text{HCl}$  etchants show minimal mask undercutting.<sup>(47)</sup>

One of the earliest and still very popular etchants for GaAs is based on bromine in methanol. Here, the bromine acts as both the oxidizing agent and the oxide remover. The  $\text{Br}_2\text{-CH}_3\text{OH}$  system can be used over a wide range of concentrations. At low concentrations, its removal rate is linearly proportional to the  $\text{Br}_2$  content. An etch rate of about  $750 \text{ \AA}/\text{min}$  can be obtained with 0.05 vol.%  $\text{Br}_2$  in  $\text{CH}_3\text{OH}$ . Higher  $\text{Br}_2$  concentrations can also be used to obtain a polishing etch.

## 2.2 Dry Etching

### 2.2.1 Plasma Fundamentals

A plasma is a gas which contains equal numbers of positive and negative charges; neutral atoms, radicals, or molecules; in addition to photons emitted from excited species. Radicals are molecule fragments with unsaturated bonds. Positive charge carriers are mostly singly ionized atoms, radicals, or molecules created by impact with energetic electrons. The majority of negative charges are free electrons. In the presence of atoms with high electron affinity, negatively charged ions can be created when these capture plasma electrons. Neutral atoms, radicals, and molecules can be in the ground or excited state. Photons are emitted when excited species lose energy via spontaneous transitions to lower energy states. This latter process is the basis for the “glow” of the discharge.

A plasma can be created by applying an electric field of sufficient magnitude to a gas. The process can be initiated by an incident electron which gains kinetic energy from the applied electric field. The probability for the electron to collide with and transfer energy to a gas atom or molecule depends upon the electron energy, the gas pressure, and

the dimensions of the plasma chamber. When a collision occurs, it results in ionization, excitation, or fragmentation of gas molecules. An ionizing collision generates an electron-ion pair. The two new charged particles are accelerated in the electric field and can in turn collide with and ionize other gas particles. As this process continues, the gas breaks down and a plasma is created. The charged particles can be neutralized by recombination within the plasma or at the chamber walls. For a plasma to be sustained, however, the rate of ionization of gas atoms or molecules must be equal to the rate of electron and ion recombination.

Collisions can result in fragmentation of gas molecules into atoms or molecules of smaller size or, for smaller electron energies, in excitation of atoms or molecules to higher energy levels. Some important chemical and physical processes that occur in a plasma are summarized in Table 1.<sup>(48)</sup> At thermal equilibrium the particles can be assumed to move randomly at an average thermal velocity between collisions, approximated by

$$\mathbf{n}_{th} \cong \sqrt{\frac{3kT}{m}} ,$$

where  $k$  is Boltzmann's constant ( $k = 8.62 \times 10^{-5}$  eV/K),  $T$  the absolute temperature, and  $m$  the particle mass. Because of their very small mass, electrons travel at much higher thermal velocity than gas atoms or molecules. The motion of charged particles under the influence of an electric field is described in terms of a drift velocity,  $v_d$ , given by

$$v_d = \mu E ,$$

where  $\mu$  is the particle mobility, and  $E$  the electric field.

Table 1. Important reactions in a plasma.

Reaction	Example
Positive ionization	$\text{Ar} + e \rightarrow \text{Ar}^+ + 2e$ $\text{O}_2 + e \rightarrow \text{O}_2^+ + 2e$
Dissociative ionization	$\text{CF}_4 + e \rightarrow \text{CF}_3^+ + \text{F} + 2e$
Fragmentation	$\text{CF}_3\text{Cl} + e \rightarrow \text{CF}_3 + \text{Cl}e^-$ $\text{C}_2\text{F}_6 + e \rightarrow 2\text{CF}_3 + e$
Dissociative attachment	$\text{CF}_4 + e \rightarrow \text{CF}_3 + \text{F}^-$
Dissociative ionization with attachment	$\text{CF}_4 + e \rightarrow \text{CF}_3 + \text{F}^- + e$
Excitation	$\text{O}_2 + e \rightarrow \text{O}_2^* + e^-$
Photoemission	$\text{O}_2^* \rightarrow \text{O}_2 + h\nu$

$\text{O}_2^*$  is the excited state of  $\text{O}_2$

Electrons also drift at a much higher velocity than ions. As electrons gain kinetic energy from the electric field, their effective temperatures increase above the gas temperature. While the temperature of the atoms and molecules in the gas remains near ambient, electrons can attain high average energies, typically 1-10 eV, corresponding to an effective electron temperature of  $10^4$ - $10^5$  K.<sup>(49-51)</sup> This energy is transferred to the gas by collision processes in which ions and highly reactive species are created. It is this property of the plasma that allows high-temperature type reactions to occur at low ambient temperatures and permits the use of temperature sensitive materials such as organic resist masks for etching.

The average distance travelled by particles between collisions, called the mean free path  $\lambda$ , depends on the species and gas pressure following the relation

$$\lambda = \frac{5 \times 10^{-3}}{P} \quad (\text{cm}),$$

where  $P$  is the pressure in Torr. The electron density in plasmas of interest ranges from  $10^9 - 10^{12} \text{ cm}^{-3}$ . It follows that the degree of ionization is very small; in typical reactors used for etching only  $10^{-4}$  to  $10^{-7}$  of the gas molecules are ionized.<sup>(52)</sup>

### 2.2.2 Sheath Formation

A simple plasma-etch reactor is shown in Figure 1. It consists of a grounded electrode which is typically connected to the chamber walls, a second electrode to which power is applied, and a partially evacuated chamber which contains a low pressure of a suitable mixture. Most systems use rf rather than dc power to avoid charge accumulation on insulator surfaces. The rf amplitude is in the range of 700-1000 V, and its frequency is typically 13.56 MHz. At such a frequency, most electrons oscillate between the

electrodes, increasing the average electron energy and probability of electron-gas collisions. The rf power source is separated from the second electrode by a coupling capacitor to block dc current components. While the plasma chamber as a whole is neutral, recombination of charges at boundary surfaces surrounding the plasma causes charge depletion near these boundaries and the formation of a boundary layer called the sheath. The resulting gradient in charges gives rise to a net diffusion of carriers to the boundaries. Since electrons diffuse faster than ions, more electrons leave the plasma initially. Consequently, an excess of positive ions is left in the plasma which now assumes a potential  $V_p$  with respect to the grounded walls. The potential  $V_p$  gives rise to a drift current component which enhances the motion of ions and retards the motion of electrons to the grounded walls. When steady-state is reached, the electron and ion fluxes are balanced and the sheath is almost depleted of electrons. As a consequence of the reduced electron concentration, the sheath conductivity decreases considerably below that of the plasma region, and the probability for electron-gas collisions is reduced creating a "dark space" region.

The large difference between electron and ion mobilities also creates a sheath near the powered electrode. Since the coupling capacitor suppresses dc current components, electrons can accumulate at the electrode surface which assumes a negative dc voltage superimposed on the time-average AC potential. The powered electrode reaches a "self-bias" negative voltage,  $V_{DC}$ , with respect to ground.<sup>(53)</sup> Similarly, when an electrically isolated surface (such as an insulating substrate isolated from ground by an insulating film) is in contact with the plasma, it must receive equal electron and ion fluxes at steady-state. Following the same reasoning as above, the isolated surface must acquire a

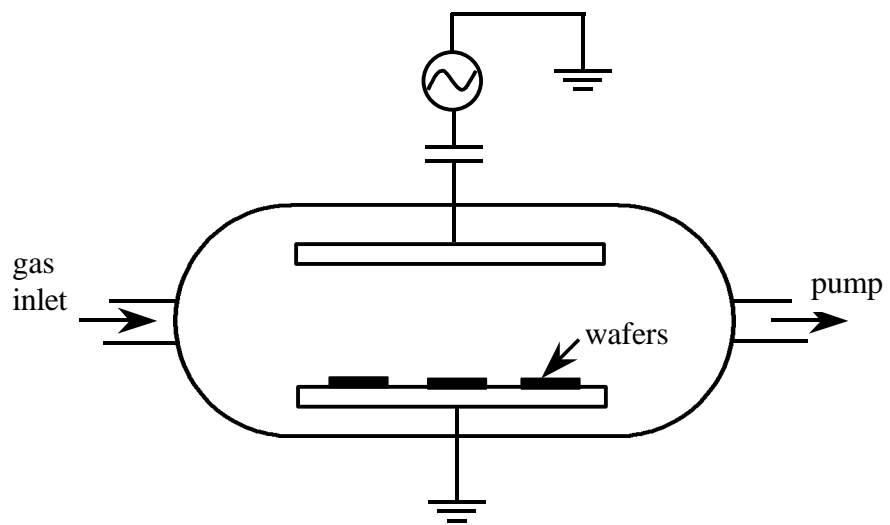


Figure 1. Schematic of a simplified plasma etch reactor.

negative potential with respect to the plasma to retard the motion of electrons and enhance the motion of ions to equalize the fluxes of both carrier types. The potential of the isolated surface with respect to ground is referred to as its floating potential,  $V_F$ . As in the case of the grounded walls and the powered electrode, the isolated surface is surrounded by a sheath of reduced electron concentration. The sheaths are typically a few millimeters thick.

### 2.2.3 Potential Distribution

The potential distribution in a plasma chamber is shown in Figure 2 for a two-electrode parallel plate reactor, with rf power applied to one of the electrodes. The second electrode, which also includes the chamber walls, is at ground potential. The three time-average potentials of importance are the plasma voltage ( $V_p$ ), the “self-bias” voltage of the powered electrode ( $V_{DC}$ ), and the floating voltage ( $V_F$ ). They determine the energies of ions incident on floating surfaces in the plasma and their effect on etching.<sup>(53)</sup> For example, the difference between the plasma and floating potential determines the maximum energy with which ions bombard an electrically floating surface. The plasma, because of its degree of ionization and high conductivity, can for practical purposes be regarded as an equipotential volume. It assumes the highest potential of the system,  $V_p$ . Most of the voltage drops across the sheath because of its high resistance. The sheaths can be represented by parallel-plate capacitors, and the magnitude of  $V_p$  approximated from a capacitive voltage dividing network. If the system is perfectly symmetric, i.e. the electrodes are of equal area and are driven by an rf signal of equal magnitude, the plasma potential is very large and both electrodes are bombarded with

energetic ions to the same extent. Typical planar reactors are, however, asymmetric and the capacitive coupling between electrode and plasma is greater at the larger electrode; the plasma potential is closer to the potential of the larger electrode than to that of the smaller electrode. If the area of the powered electrode is significantly smaller than the grounded area, as is the case for most reactors, the plasma potential is small, in the range ~ 20-50 V above ground, and the larger sheath potential appears at the smaller electrode than at the larger electrode.<sup>(53)</sup> The average sheath potential of the smaller electrode varies from about 0.25 to 0.5 of the peak to peak voltage of the applied rf signal as the reactor goes from a symmetric to a very asymmetric configuration.<sup>(48)</sup> In summary, for very asymmetric designs, a large sheath potential exists at the smaller electrode causing a high-energy ion bombardment of a surface placed on the electrode. The mean voltages across the two sheaths are divided according to the following relationship.

$$\frac{V_{small}}{V_{large}} \cong \left( \frac{A_{large}}{A_{small}} \right)^4$$

#### 2.2.4 Mechanisms of Dry Etching

Etch processes are judged by their rate, selectivity, uniformity, directionality, surface quality, and reproducibility. While typical wet etch techniques exhibit excellent selectivity and allow processing in large batches, they suffer from the inability to transfer pattern sizes smaller than about 1µm with the degree of fidelity and control required for the manufacture of VLSI/ULSI devices. Because wet etching is isotropic, the horizontal pattern dimensions must be much larger than the thickness of the film to be etched due to the inherent undercutting. These problems are solved by replacing isotropic wet chemical

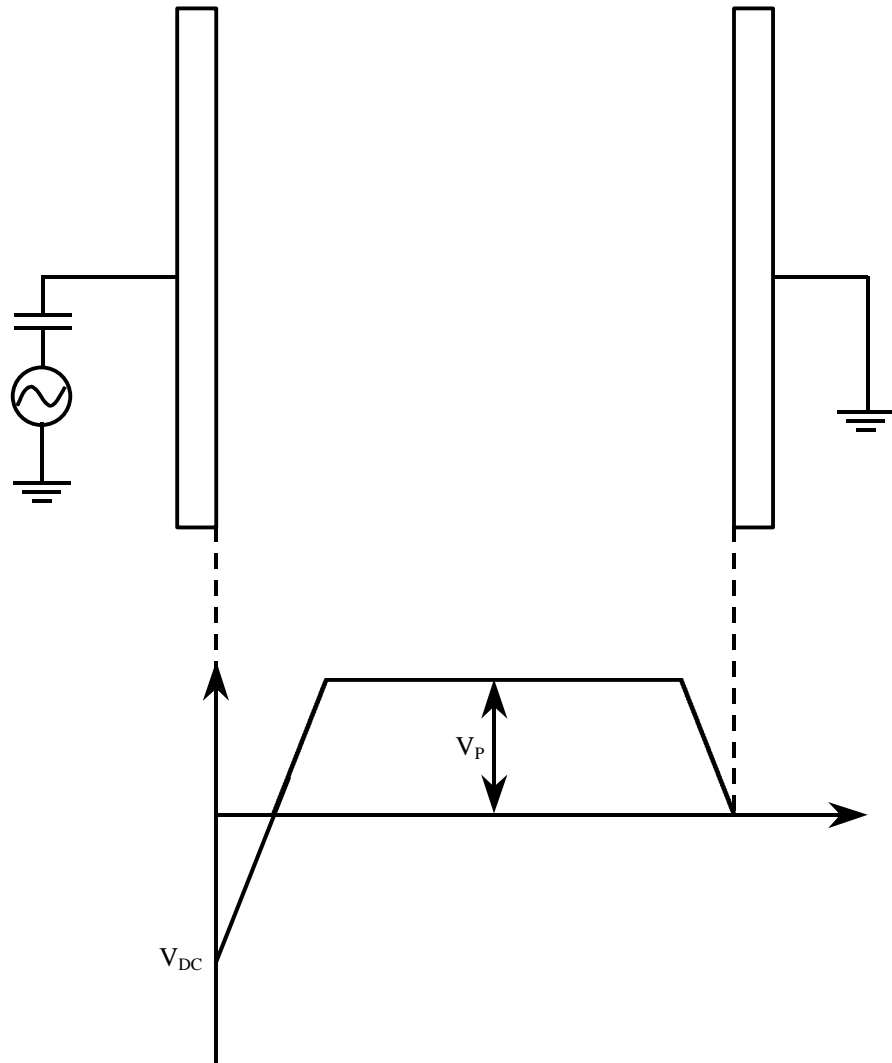


Figure 2. Potential distribution in a parallel-plate plasma reactor.

etching with dry etching techniques. Other advantages of dry over wet etching are the reduced chemical hazard and waste treatment problems, and the ease of process automation and tool clustering.<sup>(48)</sup> Since most dry etch processes use a low pressure gas in the form of a plasma to provide etchants, dry etching has become synonymous with plasma etching. There are, however, non-plasma etch techniques (such as photo-chemical and vapor etching) that are receiving increased attention and fall in the category of dry etching. While a wide variety of phenomena may play a role, etching mechanisms can be grouped into four basic categories, as shown in Figure 3.<sup>(54)</sup>

#### 1) Sputtering

Impinging particles (usually positive ions accelerated across the sheath) impinge on the surface at normal incidence. If the ion energy is above a threshold value, atoms, molecules or ions are ejected from the surface and vertical etch profiles can be obtained. Since sputtering is purely physical and requires high energy, it is the least selective mechanism. Sputtering is also characterized by low etch rate, surface facetting and trenching, and damage to the material from ion bombardment and implantation. The etch rate,  $R$ , is directly proportional to the sputter yield (the number of sputtered atoms or molecules per incident ion), given by

$$R = \frac{6.22sjW}{\mathbf{r}} \quad (\text{nm/min}),$$

where  $s$  is the sputter yield,  $j$  the ion flux ( $\text{mA/cm}^2$ ),  $W$  the molecular weight of the etched material ( $\text{g/mol}$ ), and  $\mathbf{r}$  the density of the material to be etched ( $\text{g/cm}^3$ ).

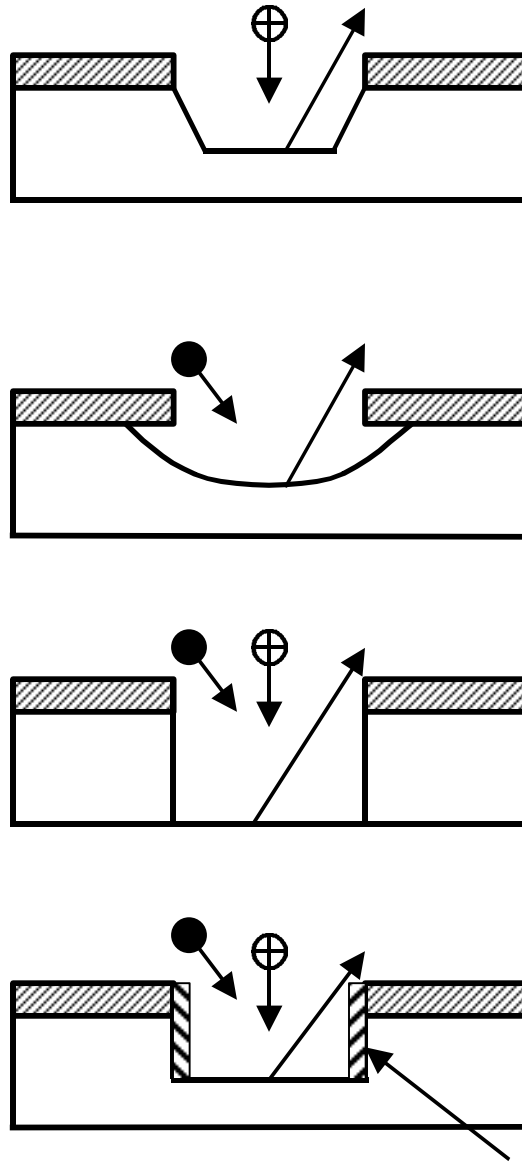


Figure 3. The four basic mechanisms of plasma etching:

- (1) sputtering
- (2) purely chemical
- (3) ion-enhanced energetic mechanisms
- (4) ion-enhanced inhibitor

## 2) Chemical Etching

The gas mixture is chosen to produce reactive species by molecular dissociation into radicals and excitation of neutrals in the plasma. In purely chemical etching, the reactive species migrate to the wafer surface while ion bombardment is suppressed. Because of the absence of physical enhancement, purely chemical etching is essentially isotropic and very selective. The key requirement for successful chemical etching is the volatility (or ability to evaporate) etch products. The number of molecules evaporating from the surface per unit area and unit time,  $n_e$ , is given by <sup>(55,56)</sup>

$$\boxed{\times} \quad (\text{cm}^{-2} \text{ s}^{-1}),$$

where  $P_V$  is the vapor pressure in Torr,  $T$  the temperature in K, and  $M$  the molecular weight in grams. The vapor pressure is given as <sup>(57)</sup>

$$\boxed{\times},$$

where  $C'$  is a material constant, and  $H_V$  is the heat of evaporation in cal/g mol, both published for various materials in. <sup>(58)</sup>

## 3) Energy-driven ion-enhanced etching

A synergistic effect of ion bombardment in the presence of reactive neutral species leads to removal rates that exceed the sum of separate chemical etching and sputtering rates. The energetic ions damage the surface and leave the material more reactive toward incident neutrals. This process offers highly anisotropic features.

#### 4) Inhibitor ion-enhanced etching

The role of ions in this mechanism is to clear the inhibitor from the horizontal surfaces. The protective film is not removed from the vertical walls because only a few scattered ions strike these surfaces. This protective film may originate from polymer-like forming precursors that adsorb during etching or from involatile etch products. This process, if properly controlled, can develop anisotropic features over very large etch depths.

#### 2.2.5 Loading and Microloading

In typical plasma reactors the etch rate is proportional to the concentration of reactive species which, on the average, is determined by the difference between the rates of generation and loss of species. In typical plasma reactors, the main loss mechanism of etchants is their consumption by reaction with the material being etched. Therefore, more reactive neutrals are depleted as the etchable surface area is increased. Since the generation of reactive species is essentially independent of the amount of etchable material present, there is a net loss of reactive species which increases as more etchable area is exposed. The result is a decrease in the etch rate as the exposed surface area is increased. Assuming a simplified case of a single etchant (such as fluorine), the dependence of etch rate  $R$  on the etchable surface area is found as <sup>(58)</sup>

$$R = \frac{G}{b + K A} t$$

where  $b$  is a reaction rate constant,  $t$  is the lifetime of active species in the absence of etchable material,  $G$  is the generation rate of reactive species, and  $K$  a constant for a given material and reactor geometry. The most serious concern caused by the loading

effect is the loss of etch control when nearing the end point. Ideally, as termination of an etch process is approached, the etch rate should decrease to allow stopping the process at the correct time and minimize overetching. With the loading effect, however, less etchable material is exposed near the end point and the etch rate increases rapidly, so that overetching is carried out at a higher rate than normal.

### 2.2.6 Selectivity

Selectivity is a critical etch parameter which refers to the relative etch rate of the film to be etched to the etch rate of another material exposed to the etchant. There are two types of selectivity, one with respect to the masking material and the other with respect to an underlying film. High selectivity with respect to both layers is needed to produce the required pattern resolution with minimal erosion of the mask and attack of the underlying film and other exposed materials.

There are three basic mechanisms for achieving selectivity of one material over another.<sup>(59)</sup> These are:

- (i) selective formation of an etch-inhibiting layer on one of the materials, i.e. the situation where deposition is occurring on one material, while the other is etched under the same conditions.
- (ii) non-reactivity of one of the materials in the particular plasma chemistry employed, such as removal of resist films in an O<sub>2</sub> plasma which does not etch the underlying Si or SiO<sub>2</sub>.
- (iii) non-volatility of a reaction product, such as formation of the non-volatile AlF<sub>3</sub> on the surface of AlGaAs upon removal of an overlying GaAs layer

in  $\text{BCl}_3/\text{SF}_6$  or equivalent chemistry.<sup>(13,60)</sup> Selectivity is nearly always decreased by ion bombardment energy because this accelerates the adsorption, reaction and desorption steps that initially produce the selective etching.<sup>(61,62)</sup>

Typical etch rates are proportional to  $\frac{1}{\exp(E_a/kT)}$ , where  $E_a$  is the activation energy which ranges from 0.1 to 2.0 eV. Therefore, changing the wafer temperature can strongly affect selectivity between materials since different materials have different activation energies and hence different etch rate dependencies upon temperature.

### 2.2.7 Plasma Damage

Wafers in a plasma are exposed to energetic particle and photon bombardment. The radiation consists of ions, electrons, ultraviolet photons, and soft X-rays. While most ions bombard the surface with energies below a few tens of volts, ion energies on the tail of the distribution can be as high as 1000 V, depending on the sheath potential. Average electron energy in the plasma ranges from a few volts to 10 V or more, but electrons reaching the walls are thought to have lower energy owing to the positive plasma potential. When high energy radiation strikes the wafer surface, it can cause both shallow and deep surface disruption, which alters electrical characteristics and degrades device performance. Both reversible and irreversible device damage can occur. In general, the significance of these effects increases with particle energy, and hence with peak rf potential and power. Device damage appears in various forms: atomic displacements caused by ion impact, which have been observed in layers up to 150 Å deep, electron-hole pairs produced by primary ionization from the UV and X-ray photons, and

secondary ionization where electrons formed by primary processes create defect centers. The damage can usually be detected as a change in the capacitance-voltage (CV) signature of MOS capacitors, or in the operating parameters of simple transistor structures, which give threshold voltage, flatband voltage, lifetime, and other parameters.

### 2.2.8 Inductively Coupled Plasma (ICP) Etching

Inductively Coupled Plasma etching has become popular in industry because it offers significant advantages over existing systems, such as Electron Cyclotron Resonance (ECR) tools. Figure 4 shows a schematic of a typical ICP system. RF current, driven at 2 MHz, is supplied to the three coils in opposite directions and causes an alternating magnetic field in the upward and downward directions. It is the rate of change of this magnetic field that induces a rf electric field that confines and accelerates electrons in a circular path. This inductive coupling is very efficient and leads to a high density plasma. Since the electrons are “trapped” in a circular path they have little chance of reaching the sample chuck which results in a low dc self-bias. Another rf source, driven at 13.56 MHz, is applied to the chuck which can control the dc bias. This allows near independent control of both ion flux (ICP power to the coils), and ion energy (rf power to the chuck). Since ICP tools do not use microwave sources or magnets for collimating the plasma, they offer advantages such as easier tuning and lower cost of ownership. ICP, as well as other high density tools, offer much higher etch rates due to the large concentration of ions and radicals. Also, since the electrons are relatively confined, fewer electrons are lost to the walls or electrode compared to RIE, resulting in a lower dc bias and less ion damage. High density tools also operate at much lower process

pressures than low density tools. Lower pressures increase the mean free path of the particles which reduces gas-phase collisions and makes it possible to produce anisotropic etching.

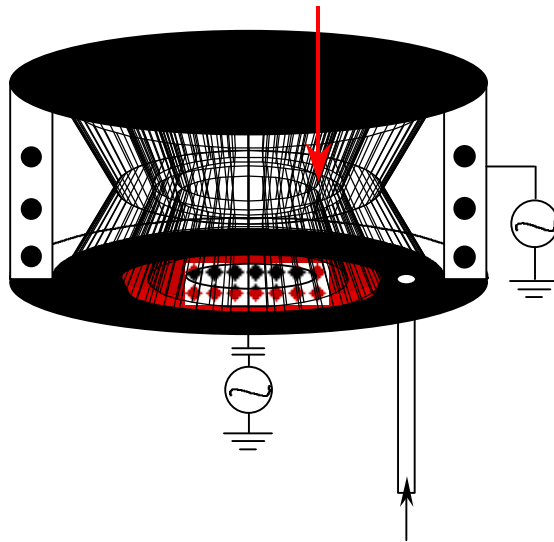


Figure 4. Schematic of a typical Inductively Coupled Plasma (ICP) reactor.

## CHAPTER 3 WET ETCHING OF THE GaAs/AlGaAs SYSTEM

### 3.1 Materials and Methods

The samples used in this study included GaAs substrates grown by liquid encapsulated Czochralski (LEC) which were undoped, semi-insulating (100) orientation and undoped, 5000Å thick  $\text{Al}_{0.22}\text{Ga}_{0.78}\text{As}$  layers grown using triethylgallium (TEG), arsine ( $\text{AsH}_3$ ), and dimethylamine alane (DMAA) in a Metal Organic Molecular Beam Epitaxy system.

Most of the etching was performed at room temperature ( $21^\circ\text{C}$ ), but temperature-controlled baths were used for activation energy determination over the range of  $0\text{-}90^\circ\text{C}$ . All etching experiments used a two part etch mixture. First, anhydrous citric acid crystals were dissolved in deionized water (DI  $\text{H}_2\text{O}$ ) at the ratio of 1g  $\text{C}_6\text{H}_8\text{O}_7$ :1ml DI  $\text{H}_2\text{O}$ . The reaction is endothermic and hinders quick dissolution, so the citric acid is mixed with deionized water at least one day in advance to ensure complete dissolution and room temperature stability. Approximately fifteen minutes before conducting any material etching, the liquid citric acid/water mixture (considered as one part  $\text{C}_6\text{H}_8\text{O}_7$  in this thesis) was mixed with 30% hydrogen peroxide at a given volume ratio (x parts  $\text{C}_6\text{H}_8\text{O}_7$  to 1 part  $\text{H}_2\text{O}_2$  by volume). The fifteen minute delay is used to allow the etchant to return to room temperature, if any temperature changes occur due to mixing

The amount of material removed during etching was determined by masking a portion of the substrate surface, using SPI carbon paint or Apiezon wax, and measuring the resulting step height formed. Etched depths were measured using a Tencor Instrument Alpha-step 100 stylus profilometer, which has a minimum resolution of 20Å. Masking was accomplished by painting over part of the semiconductor surface using a fine tip brush. The etch time varied from ten seconds to fifteen minutes depending on the material etch rate. Etching was stopped by rinsing in DI H<sub>2</sub>O for approximately one minute. The masking material was then removed in acetone, the wafer was rinsed again in DI H<sub>2</sub>O, and finally blown dry using nitrogen gas.

### 3.2 Results and Discussion

The etch rate of GaAs and AlGaAs as a function of the ratio of citric acid to hydrogen peroxide at room temperature (21°C) is shown in Figure 5. The etch rate of GaAs increases sharply from 58Å/min for a ratio of 1:1, to 5700Å/min for a ratio of 2:1. For ratios higher than 2:1 the etch rate of GaAs decreases gradually. The etch rate of AlGaAs shows a dramatic increase from 15Å/min for a 1:1 ratio, to 2170Å/min for a 6:1 ratio. For ratios higher than 6:1 the etch rate of AlGaAs decreases at the same rate as GaAs. When the temperature of the etchant solution was raised to 38°C the etch rates for both GaAs and AlGaAs increased by one and two orders of magnitude, respectively as shown in Figure 6.

The selectivity of GaAs over AlGaAs as a function of the ratio of citric acid to hydrogen peroxide at 20°C and 38°C is shown in Figure 7. The selectivity reaches a peak

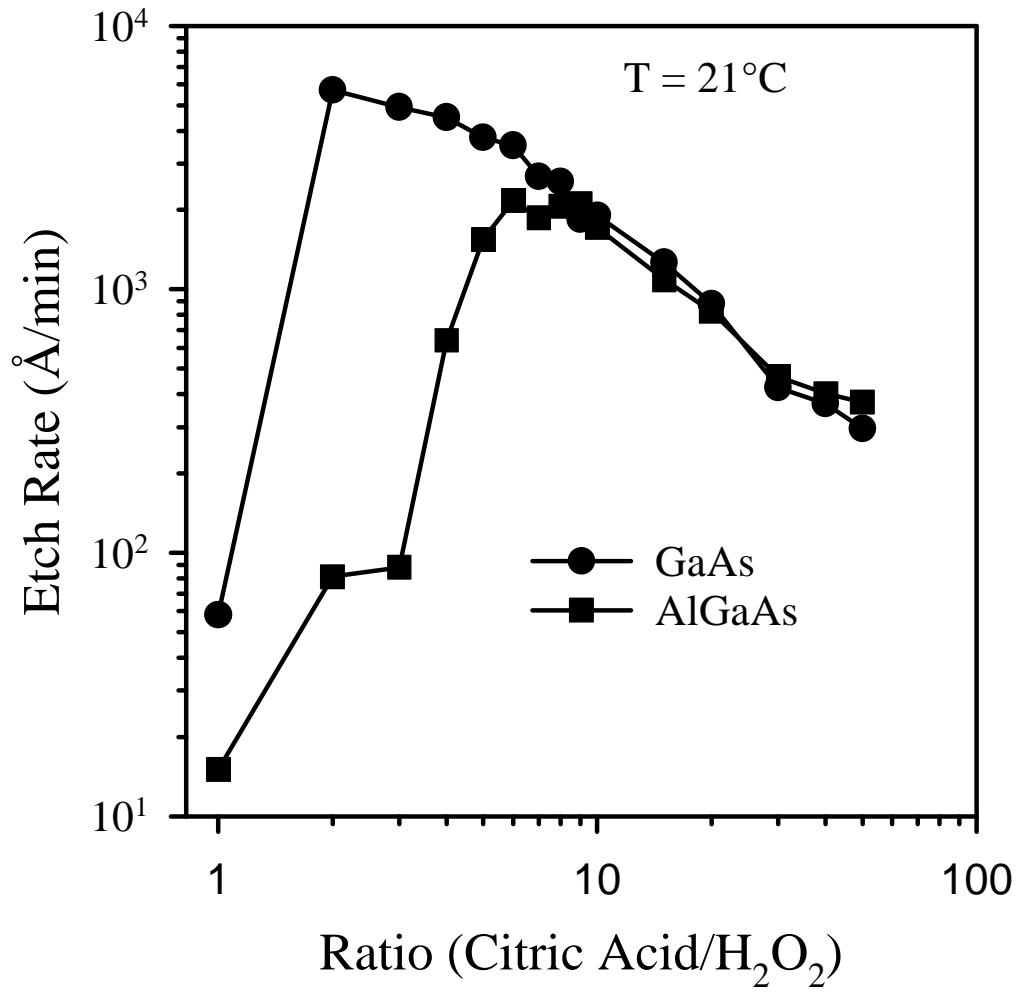


Figure 5. Etch rates of GaAs and AlGaAs at 21°C as a function of the ratio of citric acid to hydrogen peroxide

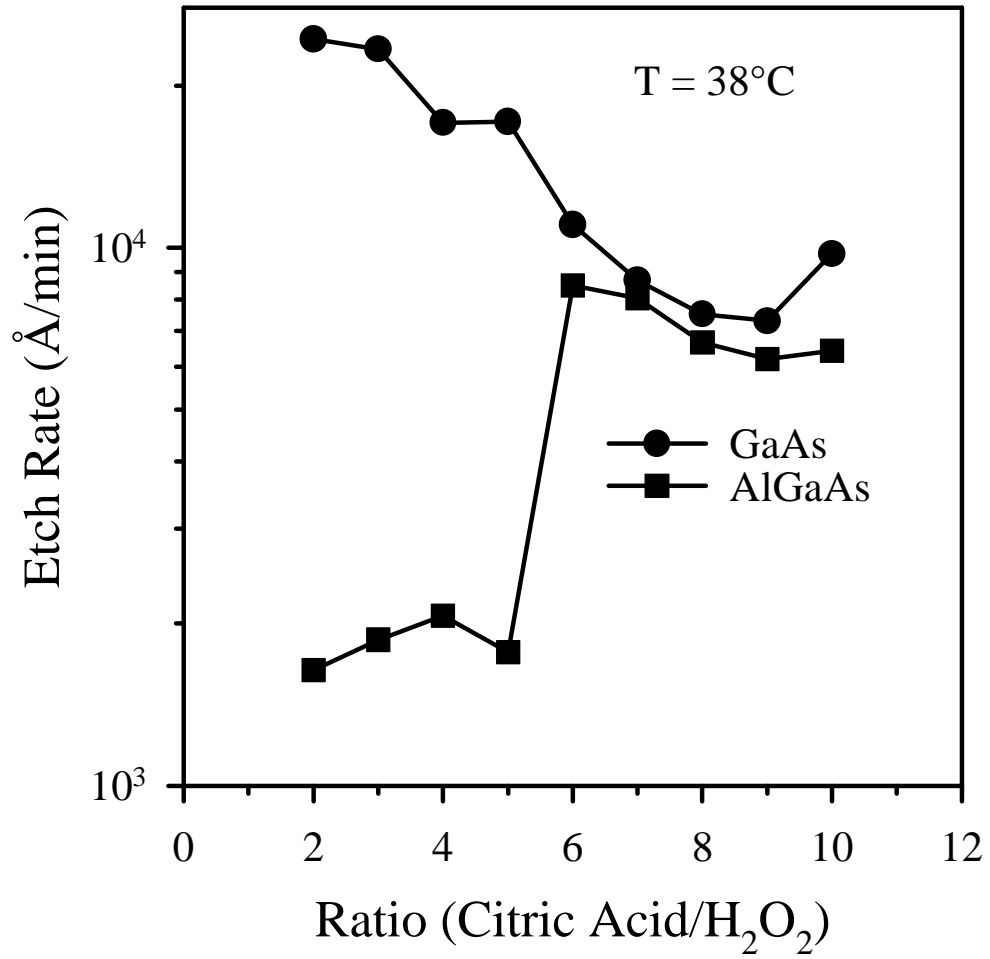


Figure 6. Etch rates of GaAs and AlGaAs at 38°C as a function of the ratio of citric acid to hydrogen peroxide

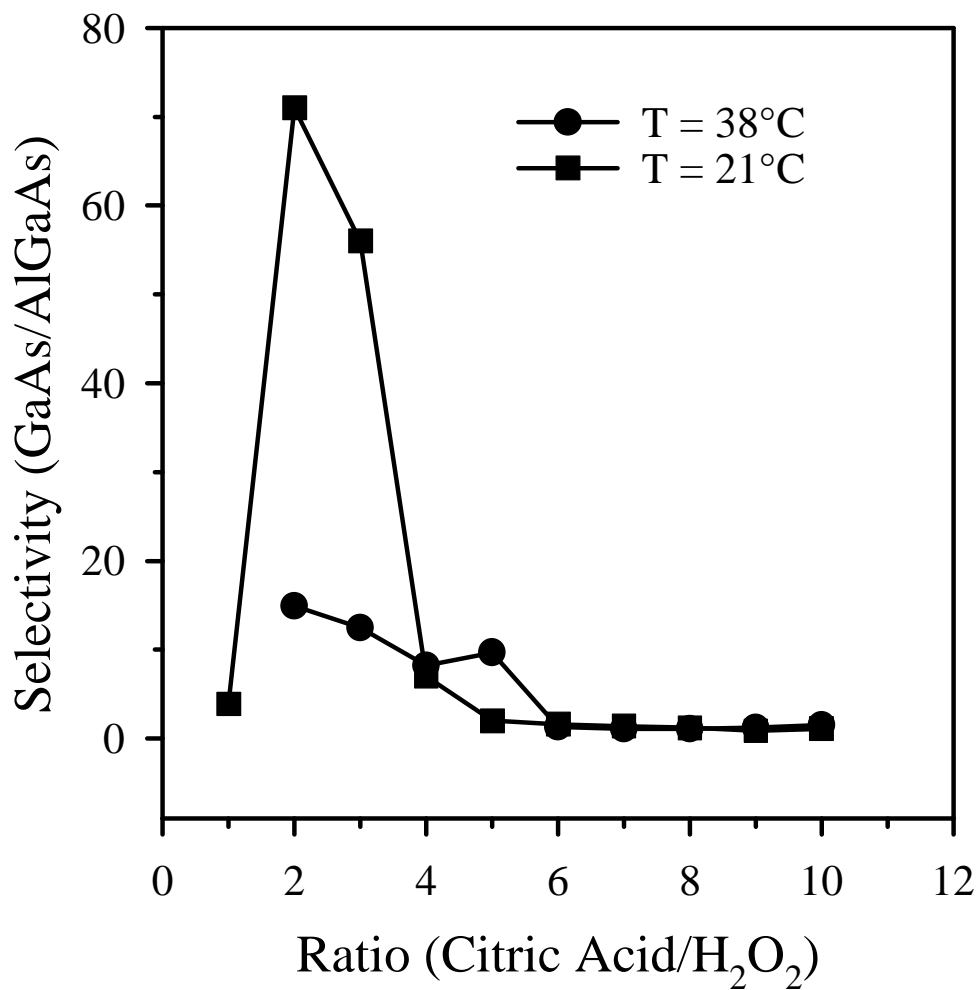


Figure 7. Selectivities of GaAs over AlGaAs at 21°C and 38°C as a function of the ratio of citric acid to hydrogen peroxide

value of 71 for a ratio of 2:1 at 21°C. Selectivity decreases sharply for higher concentrations of citric acid and is non-selective for ratios higher than 6:1. As shown in Figure 8, the AlGaAs is diffusion limited ( $E_a = 6.33$  kcal/mol) for low concentrations of citric acid while the GaAs is reaction rate limited ( $E_a = 13.7$  kcal/mol). The difference in the rate limiting steps for low concentrations of citric acid could be a major factor in achieving the very high selectivity for the ratio of 2:1. For high concentrations of citric acid, both GaAs ( $E_a = 11.3$  kcal/mol) and AlGaAs ( $E_a = 13.1$  kcal/mol) are reaction rate limited, as shown in Figure 9. The similar rate limiting steps could be a major factor in the decrease in selectivity for high ratios of citric acid to hydrogen peroxide.

The citric acid based etchants produced very smooth surfaces on GaAs (RMS roughness ~ 2-3nm) for all compositions, but caused an increase in roughness on AlGaAs for higher concentrations of citric acid, as shown in Figure 10. The surface morphologies are shown in Figure 11 for varying concentrations of citric acid. The RMS roughness for AlGaAs peaks at 24.5nm for a ratio of 6:1. The surface color of AlGaAs also changed from a shiny silver to a dull gray with higher ratios of citric acid. The change in color was determined by Auger electron spectroscopy (AES) to be high concentrations of carbon on the surface. Figure 12 shows AES results from an unetched sample of AlGaAs and displays a small peak for carbon. Figure 13 shows AES results from an AlGaAs sample etched in a 20citric acid:1H<sub>2</sub>O<sub>2</sub> solution, and displays a very large carbon peak. A depth profile is shown in Figure 14 and the carbon concentration persists to large depths ( a few hundred Angstroms) due to the rough surface, i.e. this depth is an artifact of the surface roughness

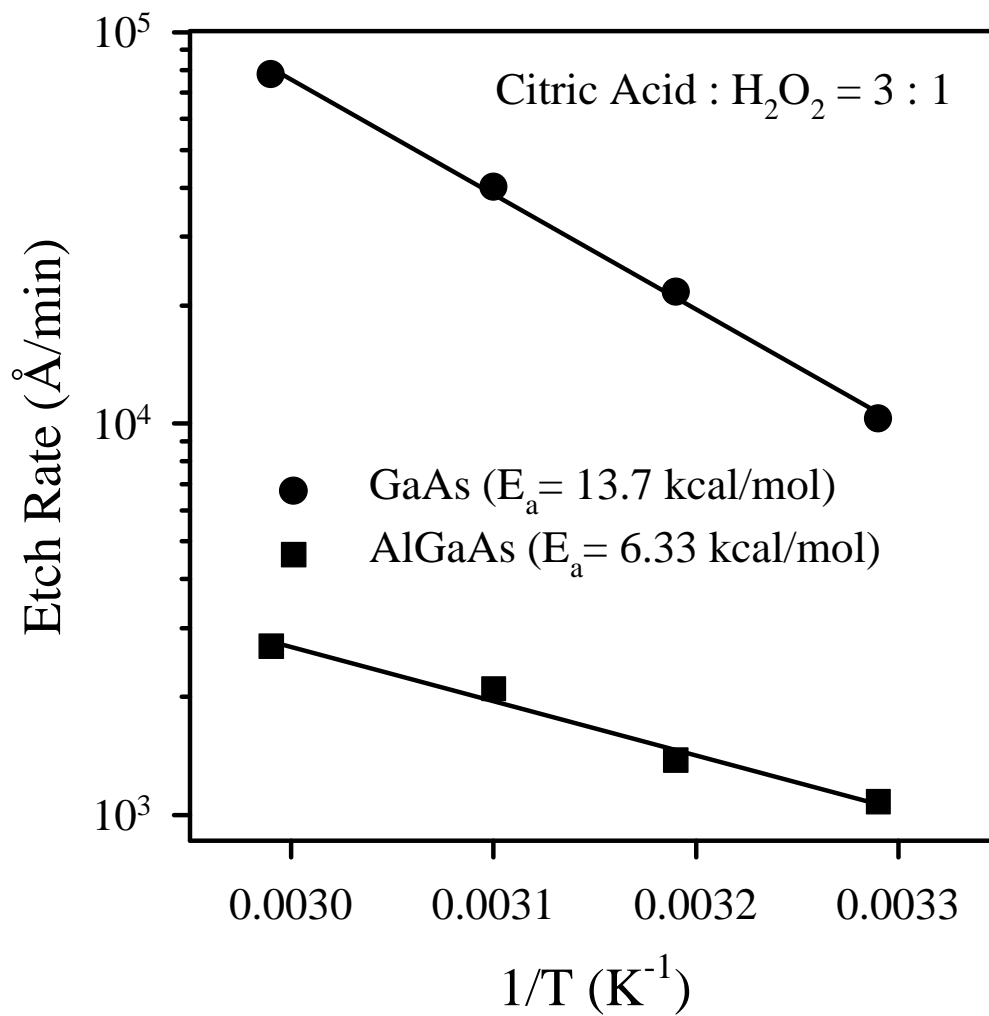


Figure 8. Etch rates of GaAs and AlGaAs in a 3citric acid:1H<sub>2</sub>O<sub>2</sub> solution as a function of temperature

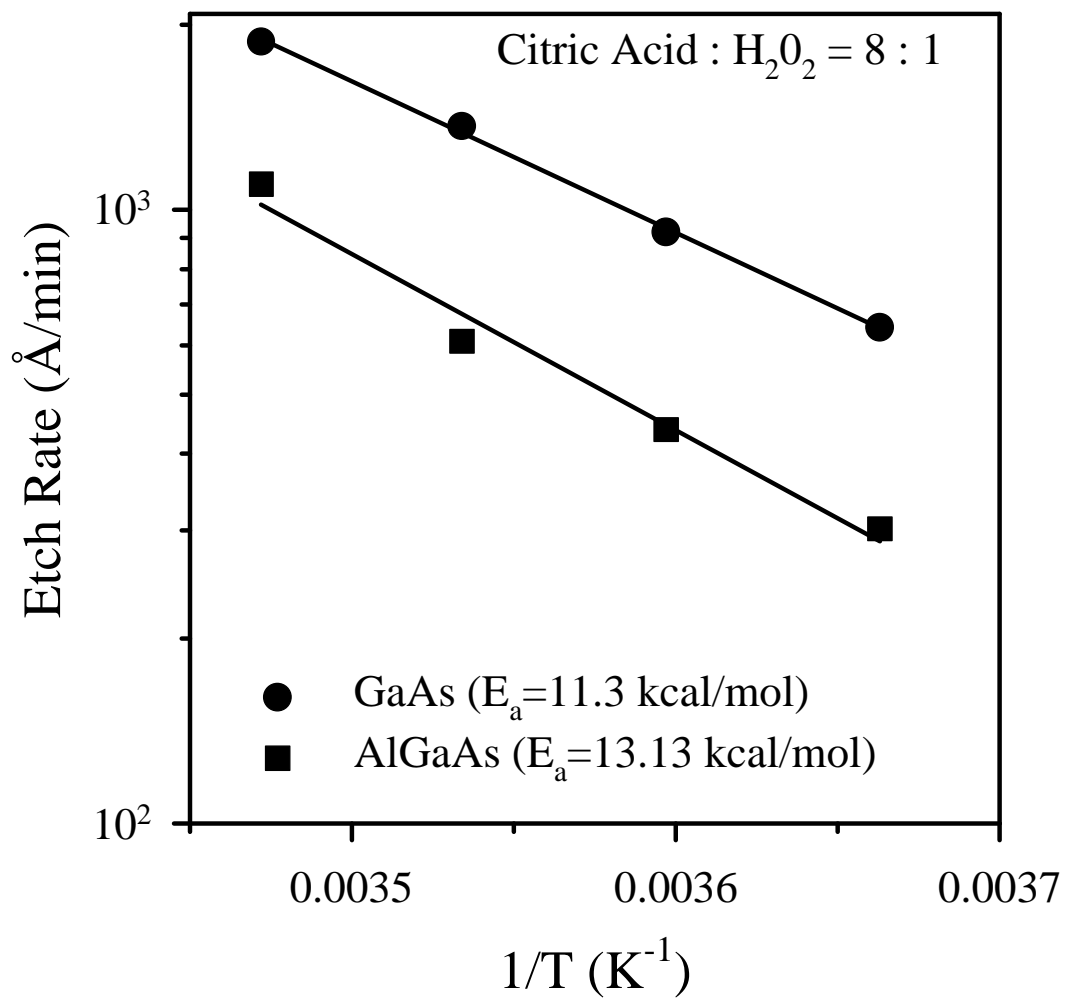


Figure 9. Etch rates of GaAs and AlGaAs in a Citric acid : H<sub>2</sub>O<sub>2</sub> solution as a function of temperature

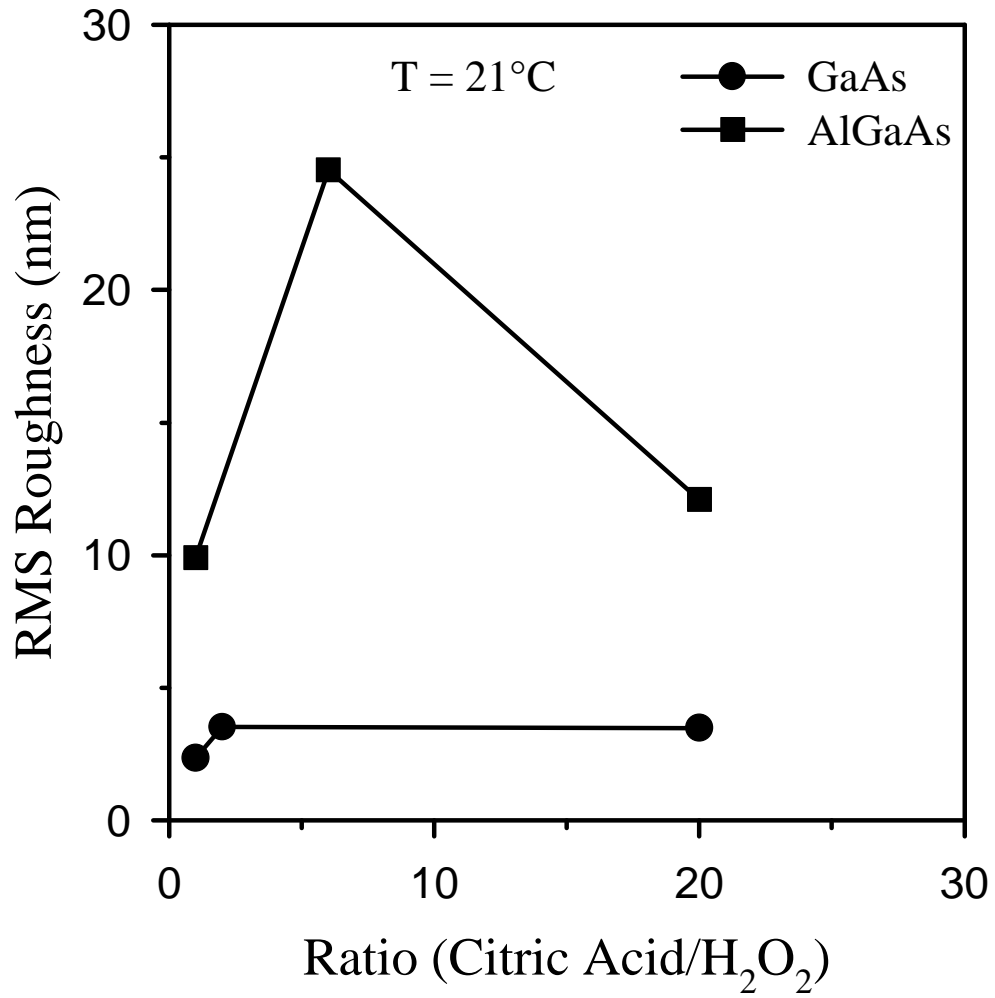
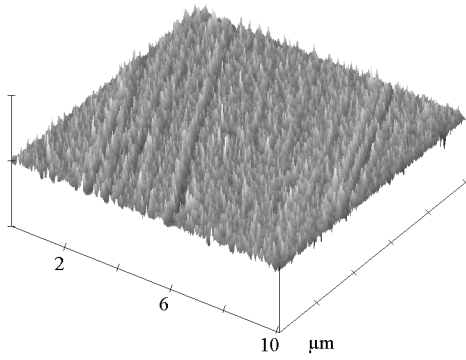
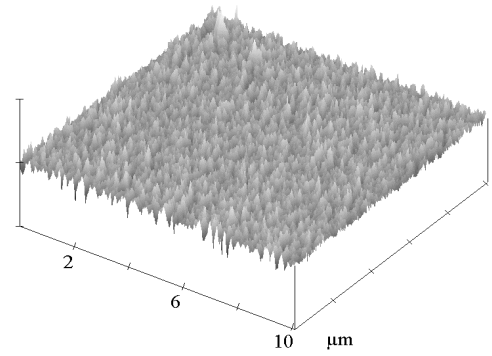


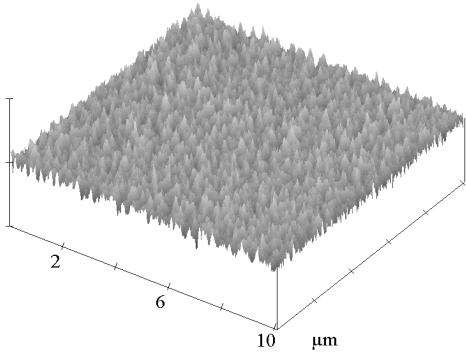
Figure 10. RMS surface roughness for GaAs and AlGaAs at 21°C as a function of the ratio of citric acid to hydrogen peroxide



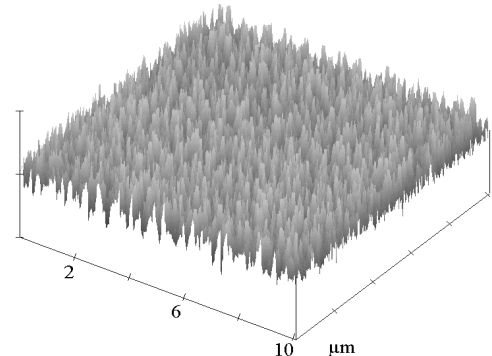
GaAs etched in 1citric acid:1H<sub>2</sub>O<sub>2</sub>  
Height scale is 50nm/div.



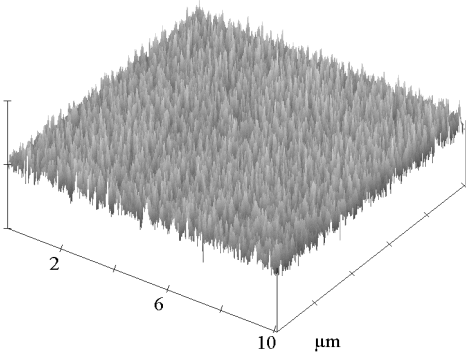
AlGaAs etched in 1citric acid:1H<sub>2</sub>O<sub>2</sub>  
Height scale is 180nm/div.



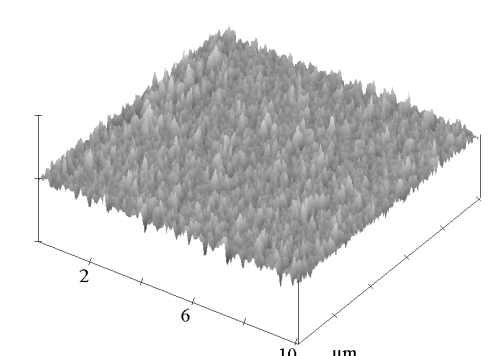
GaAs etched in 2citric acid:1H<sub>2</sub>O<sub>2</sub>  
Height scale is 50nm/div.



AlGaAs etched in 6citric acid:1H<sub>2</sub>O<sub>2</sub>  
Height scale is 180nm/div.



GaAs etched in 20citric acid:1H<sub>2</sub>O<sub>2</sub>  
Height scale is 50nm/div.



AlGaAs etched in 20citric acid:1H<sub>2</sub>O<sub>2</sub>  
Height scale is 180nm/div.

Figure 11. AFM scans of GaAs(left) and AlGaAs(right) etched in various concentrations of citric acid:H<sub>2</sub>O<sub>2</sub> solutions at 21°C.

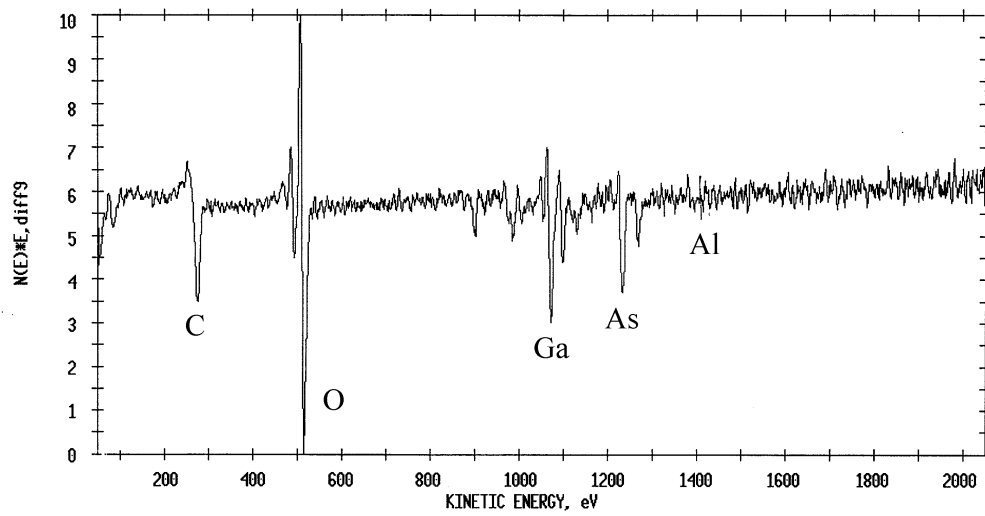


Figure 12. AES surface scan of unetched AlGaAs

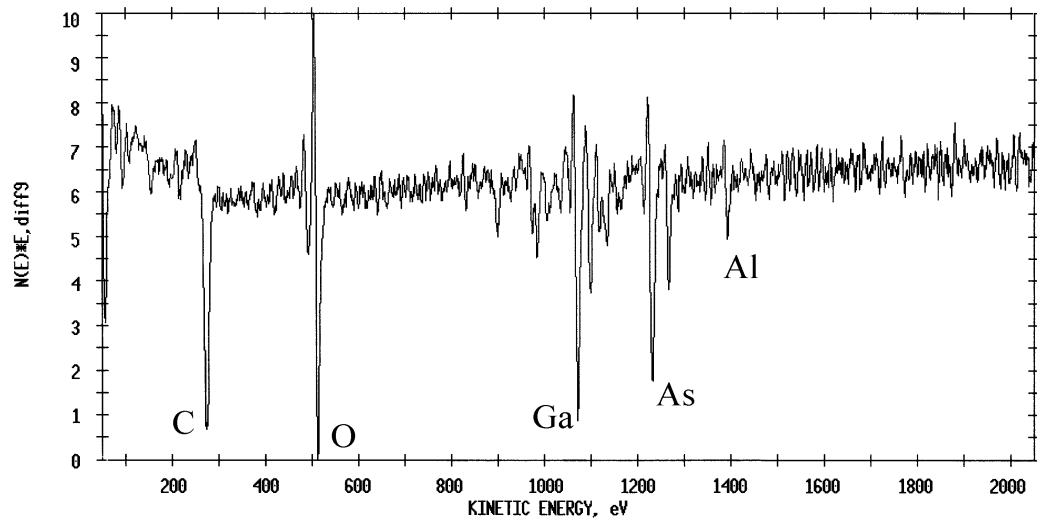


Figure 13. AES surface scan of AlGaAs etched in 20citric acid:1H<sub>2</sub>O<sub>2</sub>

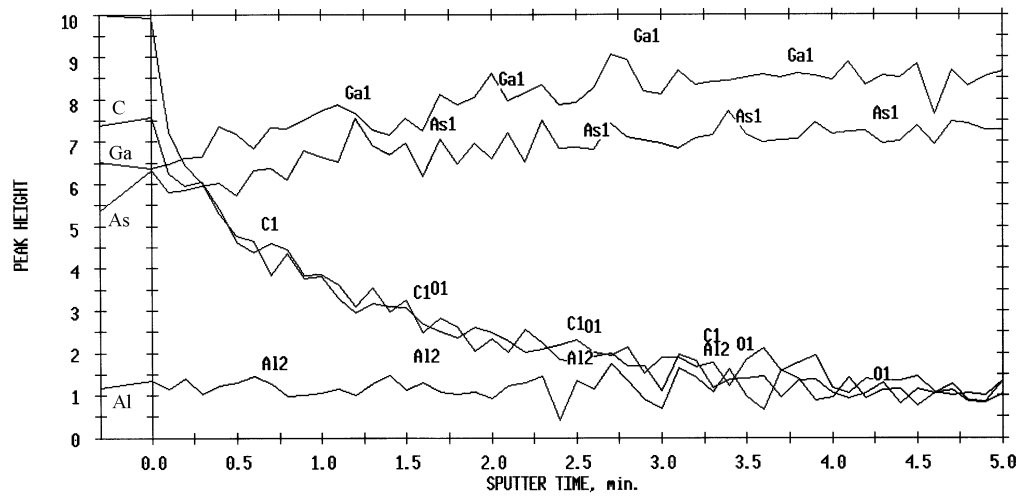


Figure 14. AES depth profile of AlGaAs etched in 20% citric acid:1H<sub>2</sub>O<sub>2</sub>

## CHAPTER 4 DRY ETCHING OF GaAs/AlGaAs/InGaP

### 4.1 Materials and Methods

Device quality epitaxial layers of  $\text{Al}_{0.22}\text{Ga}_{0.78}\text{As}$  and  $\text{In}_{0.5}\text{Ga}_{0.5}\text{P}$   $1\mu\text{m}$  thick were grown on undoped GaAs substrates by either Metal Organic Molecular Beam Epitaxy<sup>(63)</sup> or Metal Organic Chemical Vapor Deposition.<sup>(64)</sup> The AlGaAs and InGaP layers were nominally undoped ( $n\sim 10^{16}\text{ cm}^{-3}$ ). The GaAs was semi-insulating, (100) oriented substrates. The samples were masked with Apiezon wax for the etch rate experiments and etch depths were obtained by stylus profilometry.

The dry etching was performed as a function of ICP source power, percentage in input gas mixture, chamber pressure, and rf chuck power. The reactor used was a Plasma Therm 790 ICP system, in which a 2MHz, 3 turn coil generates the plasma, and the sample is mounted on a rf-powered(13.56MHz), He backside cooled chuck.

### 4.2 Results and Discussion

#### (a) $\text{BCl}_3/\text{SF}_6$

Under RIE conditions (where etch rates for GaAs were  $<2500\text{ \AA}/\text{min}$  and for AlGaAs and InGaP of  $\sim 30\text{ \AA}/\text{min}$ ), selectivities for GaAs over both AlGaAs and InGaP of  $>80$  were achieved for low dc chuck biases ( $< -80\text{V}$ ) for discharge compositions comprising  $\sim 20\%$   $\text{SF}_6$ . This is the composition where the  $\text{Cl}^0$  concentration and hence

GaAs etch rate is highest. With the addition of 200W ICP source power(Figure 15) the etch rates for all three materials increase by at least an order of magnitude for similar discharge composition. However, peak selectivities of ~45 for GaAs/AlGaAs and ~8 for GaAs/InGaP are obtained. Note the essentially non-selective etching for pure  $\text{BCl}_3$ , as expected.

To more fully investigate the role of ICP source power, Figure 16 shows etch rates and selectivities for a fixed discharge composition( $12\text{BCl}_3/3\text{SF}_6$ ). When source power is first added, the etch rates of all three materials decreases, probably due to a strong increase in atomic fluorine in the discharge which blocks the surface to chlorine neutral adsorption. As source power is increased above 100W the etch rates go through a maximum. This is commonly observed in ICP etching and is suggested to result from a competition between increased ion and radical flux, and reduced ion energy at high source power. Note that the etch selectivities rapidly decrease above 200-300W, since sputter-assisted desorption of the  $\text{AlF}_3$  and  $\text{InF}_3$  will be efficient at high ion fluxes.

Figure 17 shows the effect of process pressure under ICP conditions. The etch rates decrease for all three materials due to increased ion and radical recombination in the discharge, and there is a general trend for reduced selectivity. This is contrary to the situation under RIE conditions, shown in Figure 18. In this case the GaAs etch rate continues to increase due to the higher chlorine radical density, whereas there is little change in the AlGaAs or InGaP etch rate. This produces very high GaAs/AlGaAs and GaAs/InGaP selectivities as shown in the lower part of Figure 18. In the ICP case, the GaAs etch rate falls because of the additional fluorine surface coverage.

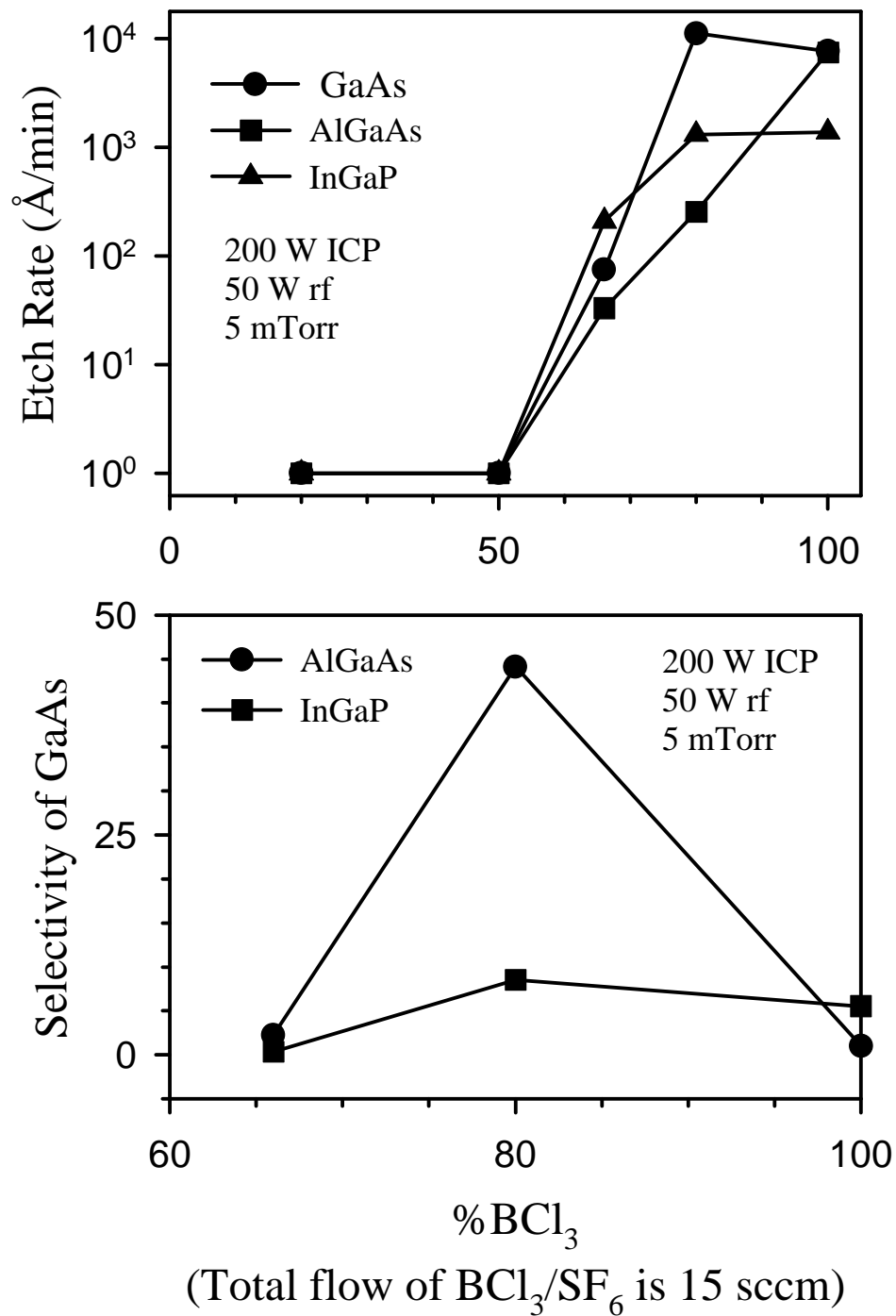


Figure 15. Etch rates of GaAs, AlGaAs, and InGaP(top) and resultant selectivities for GaAs over AlGaAs and InGaP(bottom) as a function of BCl<sub>3</sub> percentage in ICP BCl<sub>3</sub>/SF<sub>6</sub> discharges (200W source power, 50W rf chuck power, 5mTorr)

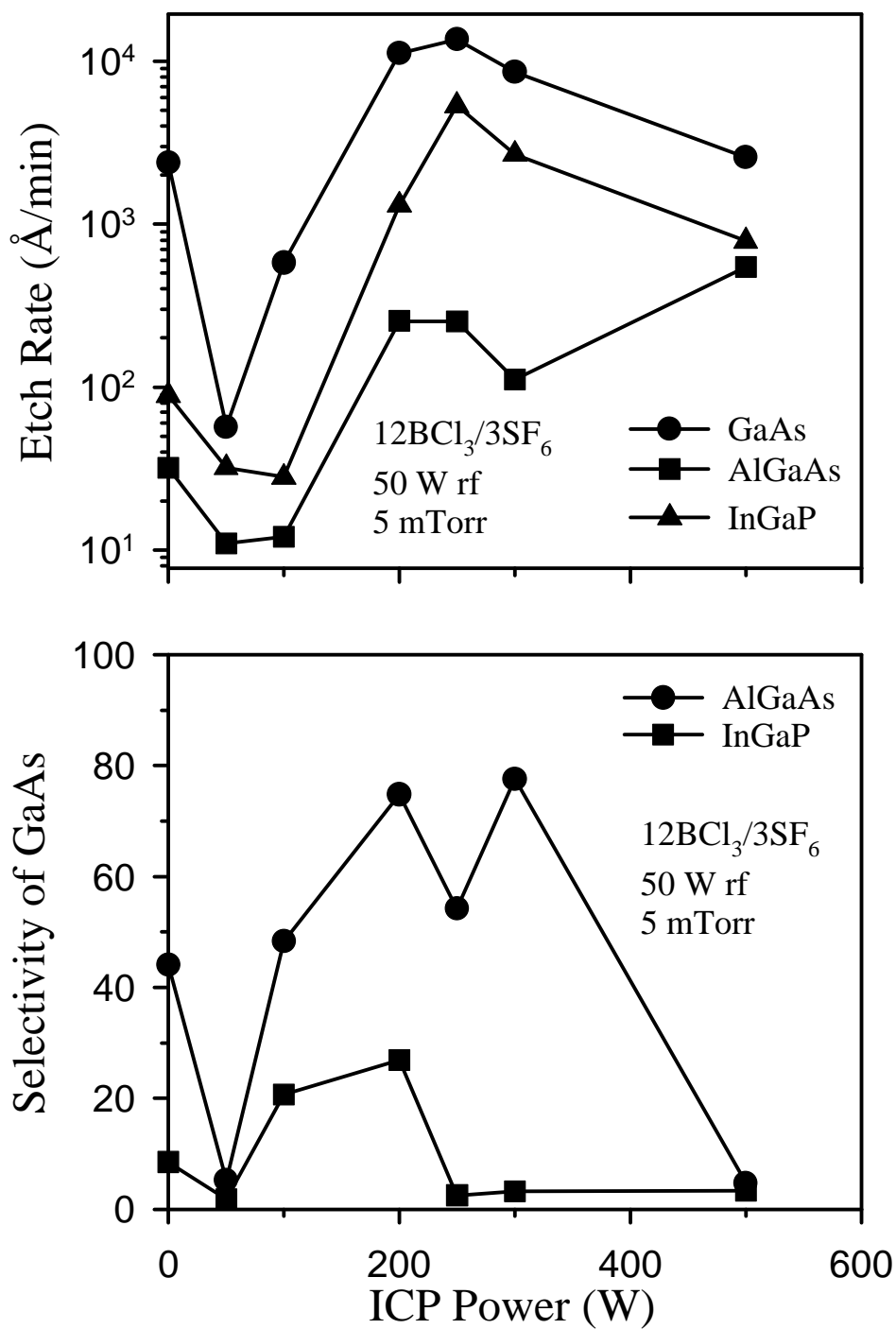


Figure 16. Etch rates of GaAs, AlGaAs, and InGaP(top) and resultant selectivities for GaAs over AlGaAs and InGaP(bottom) as a function of source power in ICP 12BCl<sub>3</sub>/3SF<sub>6</sub> discharges (50W rf chuck power, 5mTorr)

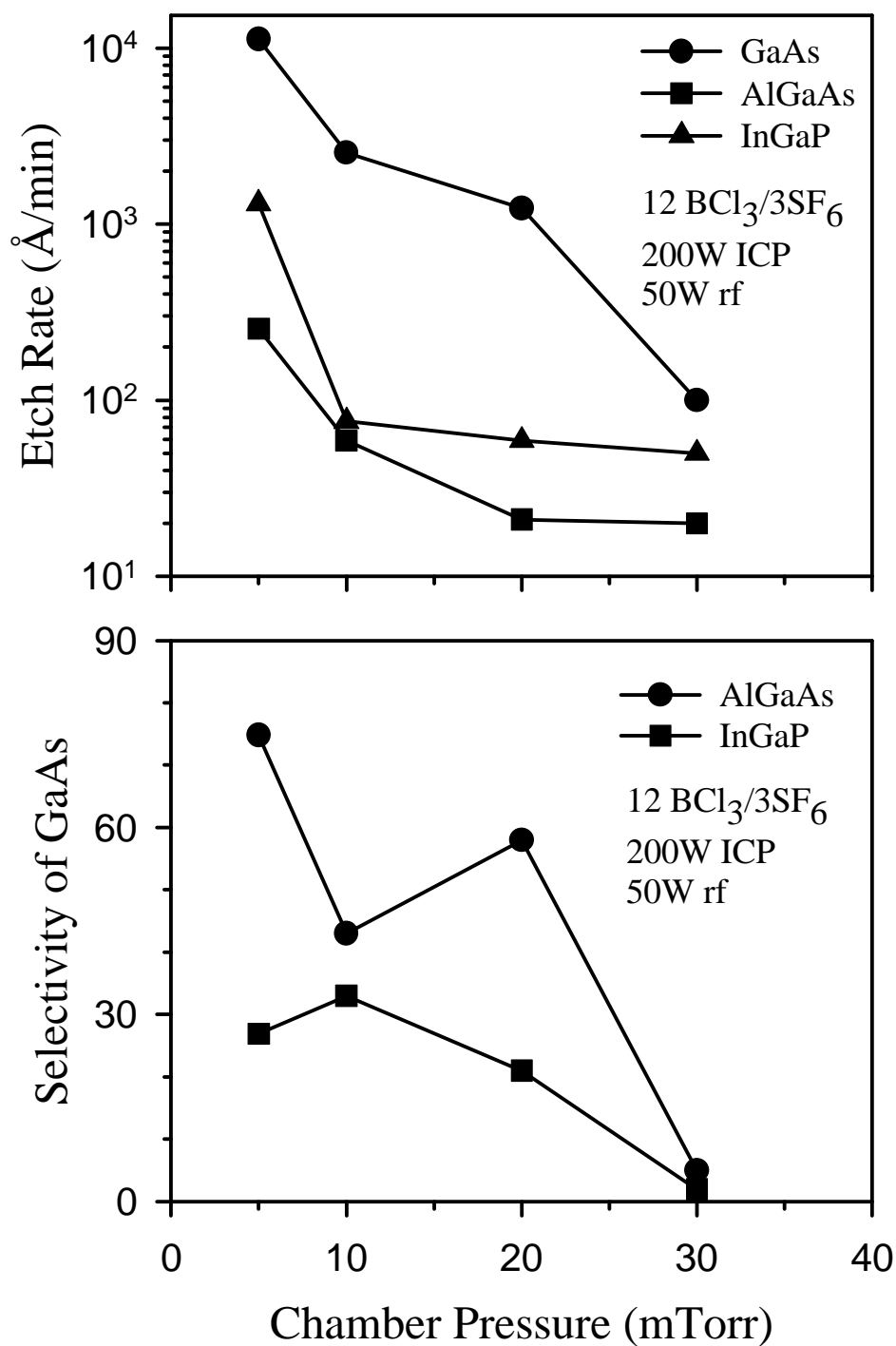


Figure 17. Etch rates of GaAs, AlGaAs, and InGaP(top) and resultant selectivities for GaAs over AlGaAs and InGaP(bottom) as a function of pressure in ICP 12BCl<sub>3</sub>/3SF<sub>6</sub> discharges (200W source power, 50W rf chuck power)

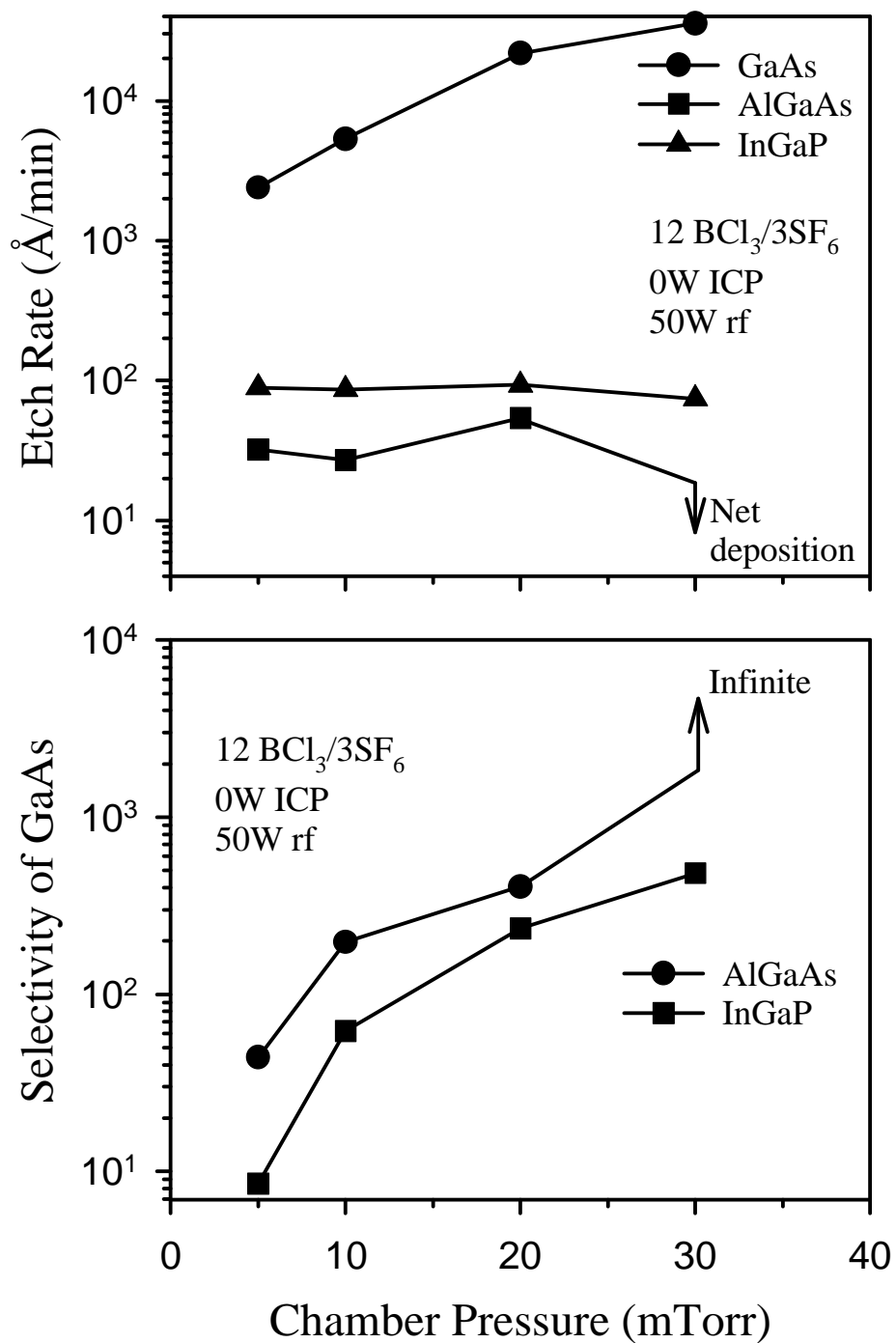


Figure 18. Etch rates of GaAs, AlGaAs, and InGaP(top) and resultant selectivities for GaAs over AlGaAs and InGaP(bottom) as a function of pressure in RIE 12BCl<sub>3</sub>/3SF<sub>6</sub> discharges (50W rf chuck power)

The effect of rf chuck power, which controls incident ion energy, is shown in Figure 19. The etch rates tend to saturate above ~50W for the chosen parameter space, since the etching probably becomes reactant-limited, i.e. the adsorbed chlorine coverage is less than necessary to achieve the highest rate of etch product formation and ion-assisted desorption. The selectivities are maximized at low rf powers and decrease at higher values due to ion-assisted desorption of the aluminum and indium fluoride and the indium chloride. Thus, both ion energy and ion flux must be controlled to achieve good etch selectivities in both heterostructure systems.

(b)  $\text{BCl}_3/\text{NF}_3$

$\text{NF}_3$  is a less desirable choice than  $\text{SF}_6$  from the point of view of cost and corrosion issues, but it is less strongly bonded and might be expected to produce more atomic fluorine at low ICP source powers. We performed the same runs with  $\text{BCl}_3/\text{NF}_3$  in order to compare with the more common  $\text{BCl}_3/\text{SF}_6$  chemistry.

Figure 20 shows the influence of discharge composition for low ICP source power (200W) conditions. The resultant etch selectivities for GaAs/AlGaAs and GaAs/InGaP are significantly lower than achieved with  $\text{BCl}_3/\text{SF}_6$  under the same conditions. This was true even for RIE conditions, where maximum selectivities of typically <10 were obtained.

Figure 21 shows the effect of source power on etch rates and selectivity for a fixed plasma composition of 12 $\text{BCl}_3$ /3 $\text{NF}_3$ . The maximum selectivities are ~50 for GaAs/AlGaAs and ~25 for GaAs/InGaP, which again are lower than achieved with  $\text{BCl}_3/\text{SF}_6$ .

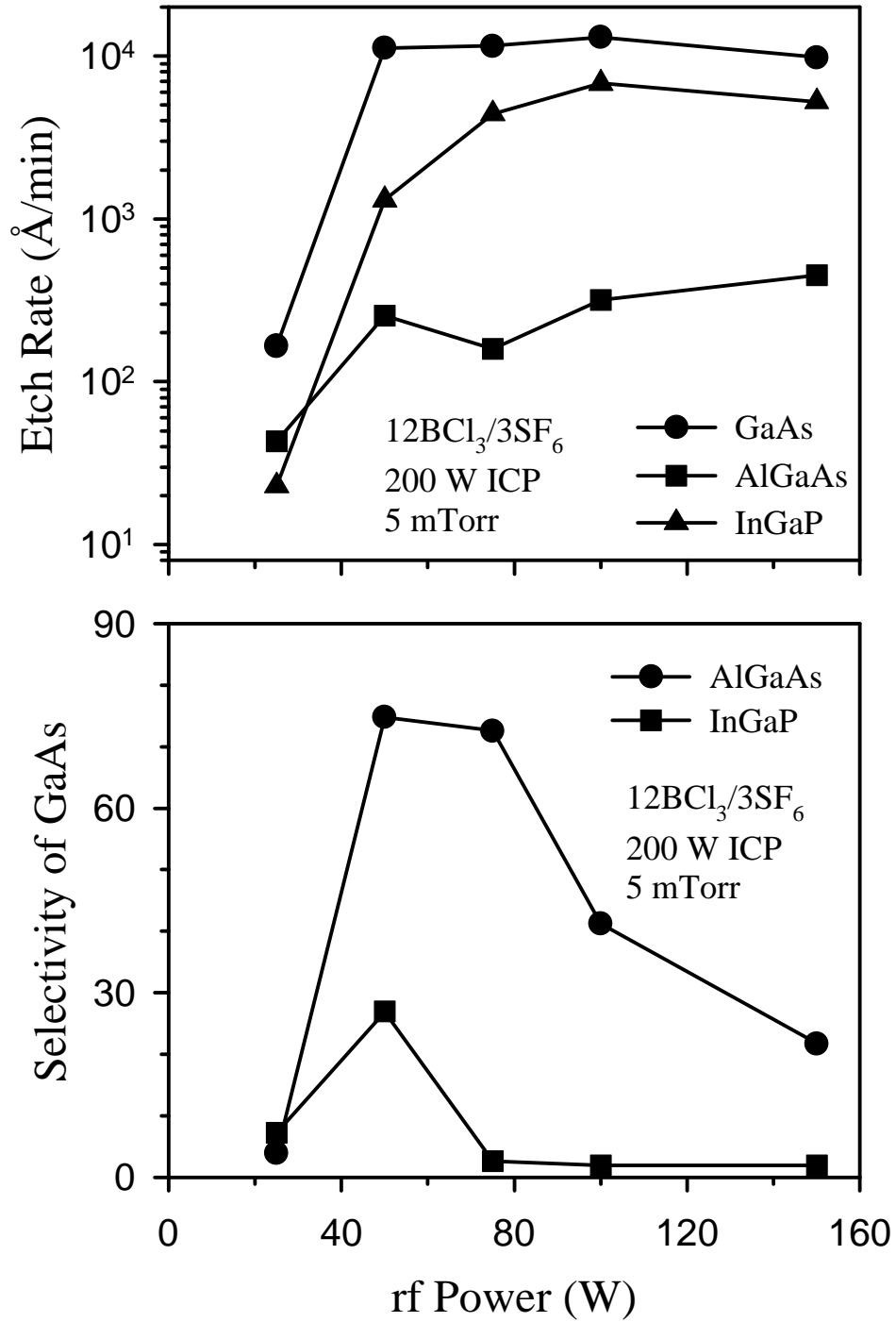


Figure 19. Etch rates of GaAs, AlGaAs, and InGaP(top) and resultant selectivities for GaAs over AlGaAs and InGaP(bottom) as a function of rf chuck power in ICP  $12\text{BCl}_3/3\text{SF}_6$  discharges (200W source power, 5mTorr)

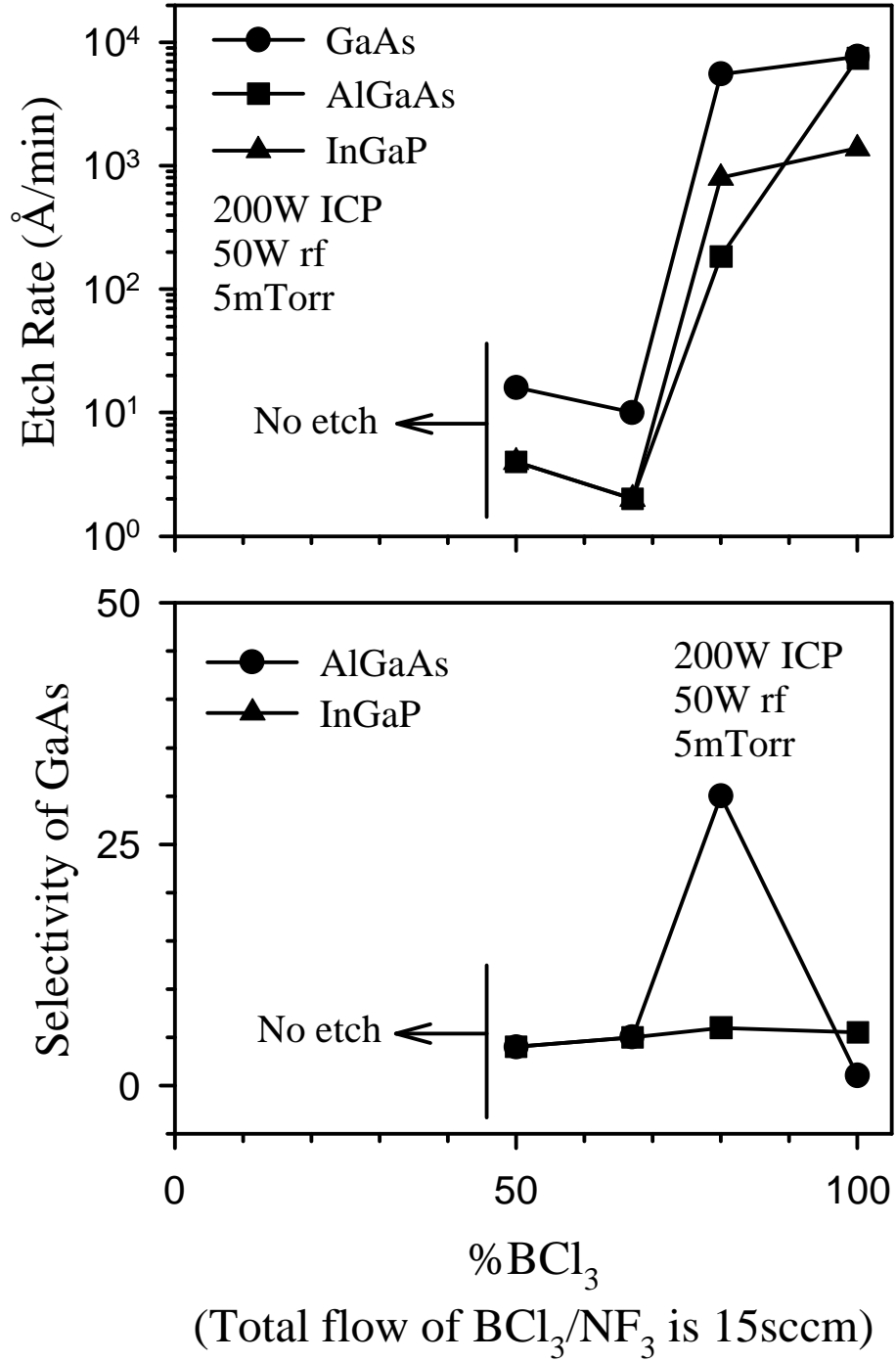


Figure 20. Etch rates of GaAs, AlGaAs, and InGaP(top) and resultant selectivities for GaAs over AlGaAs and InGaP(bottom) as a function of  $\text{BCl}_3$  percentage in ICP  $\text{BCl}_3/\text{NF}_3$  discharges (200W source power, 50W rf chuck power, 5mTorr)

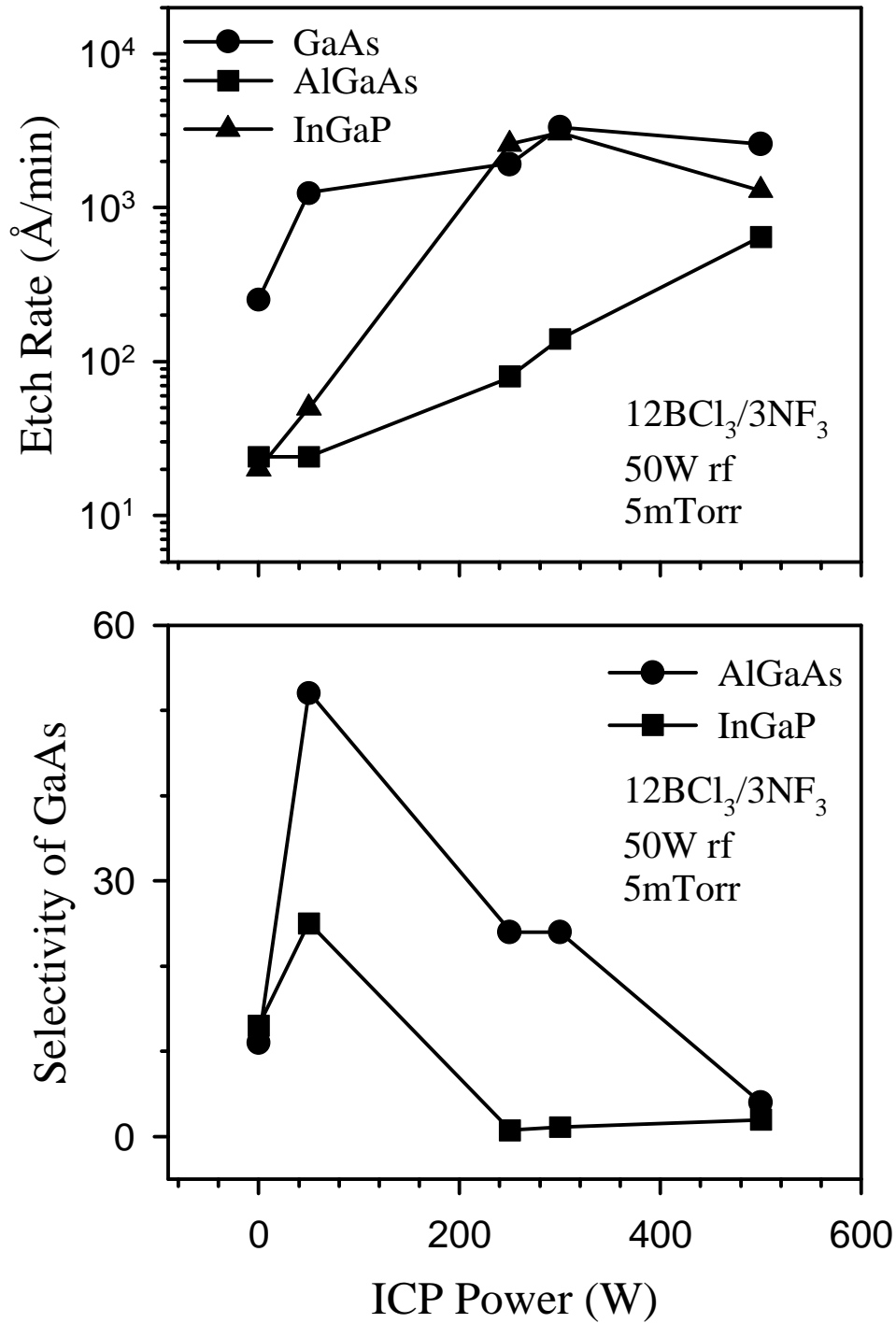


Figure 21. Etch rates of GaAs, AlGaAs, and InGaP(top) and resultant selectivities for GaAs over AlGaAs and InGaP(bottom) as a function of source power in ICP 12BCl<sub>3</sub>/3NF<sub>3</sub> discharges (50W rf chuck power, 5mTorr)

The etch rates of all three materials decreased rapidly with pressure (Figure 22). The same trend was observed under RIE conditions, with the rates being roughly a factor of 30 lower than for ICP etching. Selectivities were at least as good under ICP conditions reaching ~30 for GaAs/AlGaAs and ~8 for GaAs/InGaP compared to 11-13 for both systems under RIE conditions. The selectivities decreased again for higher rf chuck powers, as shown in Figure 23 and were lower than those obtained with  $\text{BCl}_3/\text{SF}_6$ .

Etched surface morphology was examined using AFM for GaAs, AlGaAs, and InGaP samples etched at 200 W ICP power, 150 W rf chuck power, 5 mTorr in both  $\text{BCl}_3/\text{SF}_6$ , and  $\text{BCl}_3/\text{NF}_3$ . From the data it is seen that  $\text{BCl}_3/\text{NF}_3$  produces rougher surfaces on InGaP (Figure 24) than  $\text{BCl}_3/\text{SF}_6$ , and the opposite is found for GaAs as shown in Figure 25. ( $\text{BCl}_3/\text{SF}_6$  produces rougher surfaces). The AlGaAs surface morphology, presented in Figure 26, shows that the RMS roughness remains nearly constant and similar to the control sample.

In addition to the surface smoothness, equi-rate removal of group III and V components or their corresponding etch products are very important to guarantee the stoichiometry of the etched surface. Figure 27 shows the AES surface scan of GaAs etched in  $\text{BCl}_3/\text{SF}_6$  (top) and  $\text{BCl}_3/\text{NF}_3$  (bottom) plasmas at 0 W ICP power, 50 W rf chuck power and 10 mTorr. There is oxygen present that grows on the samples in the course of transfer from the ICP chamber to the AES system, and also carbon contamination due to the exposure to surrounding air. The sample etched in  $\text{BCl}_3/\text{SF}_6$  shows sulfur contamination, indicating the need for an additional in-situ or ex-situ cleaning step.

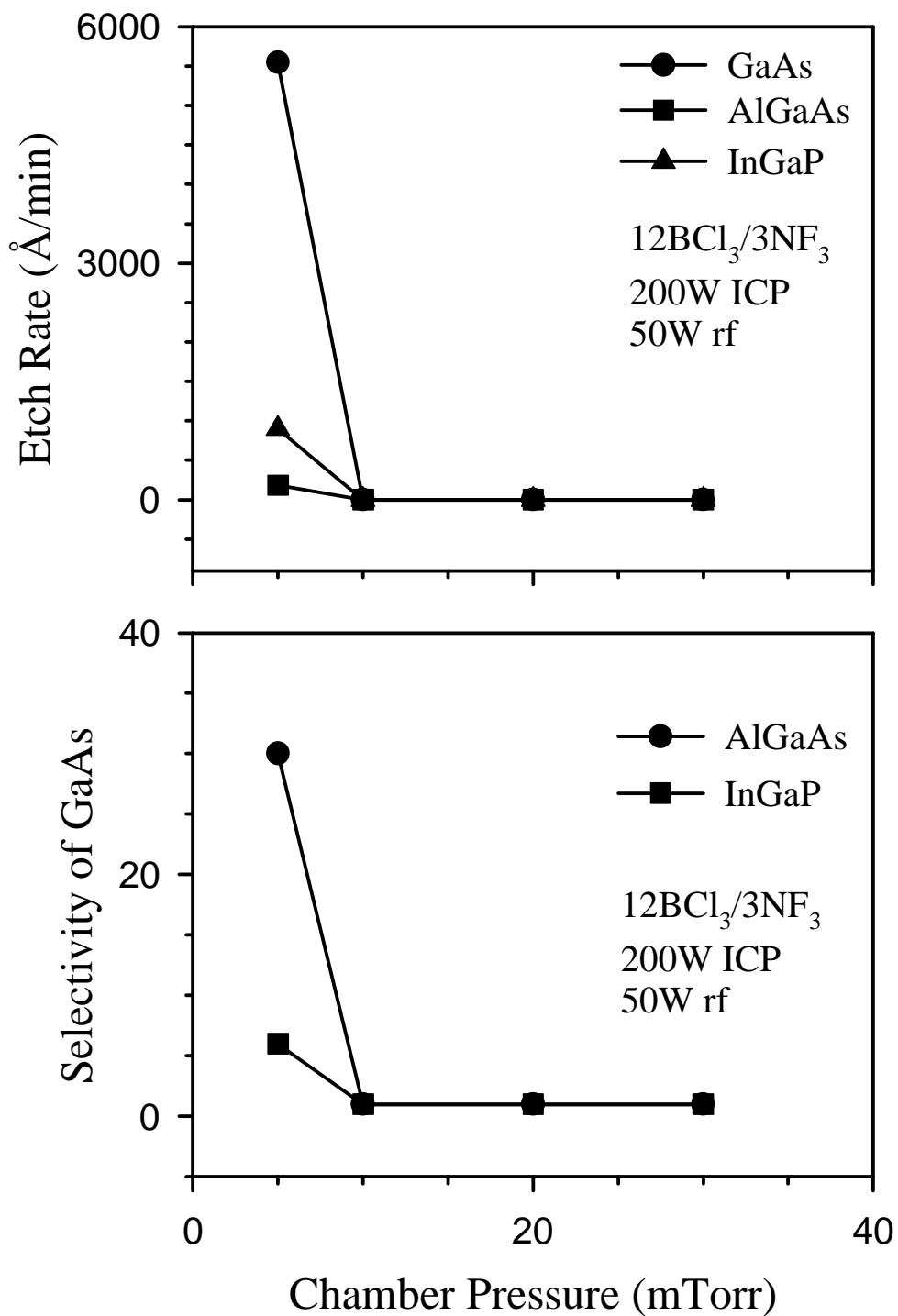


Figure 22. Etch rates of GaAs, AlGaAs, and InGaP(top) and resultant selectivities for GaAs over AlGaAs and InGaP(bottom) as a function of pressure in ICP 12BCl<sub>3</sub>/3NF<sub>3</sub> discharges (200W source power, 50W rf chuck power)

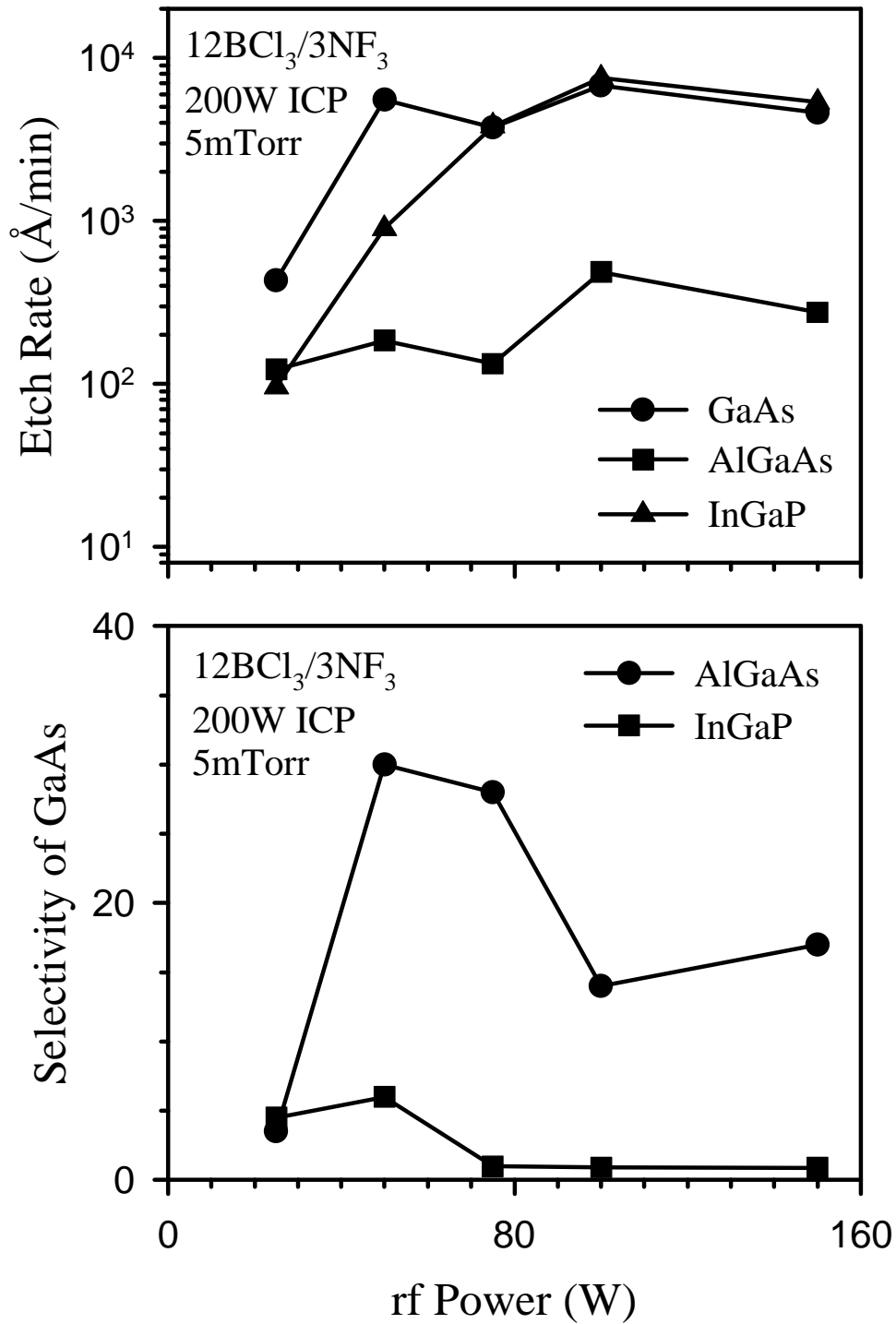
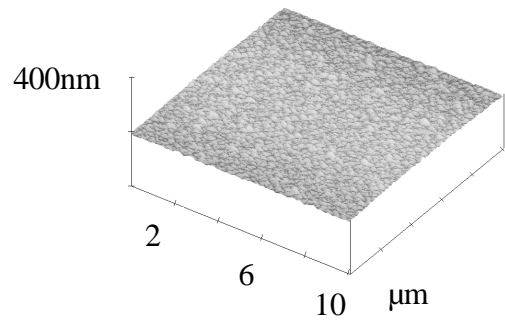
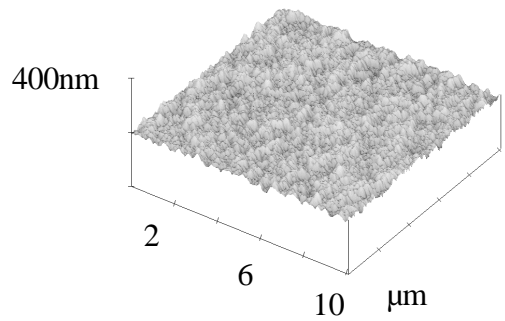


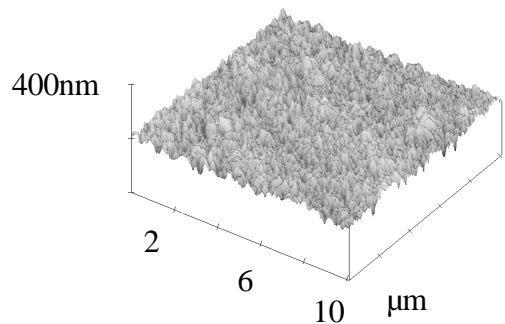
Figure 23. Etch rates of GaAs, AlGaAs, and InGaP(top) and resultant selectivities for GaAs over AlGaAs and InGaP(bottom) as a function of rf chuck power in ICP 12BCl<sub>3</sub>/3NF<sub>3</sub> discharges (200W source power, 5mTorr)



InGaP Control  
RMS Roughness = 4.1nm

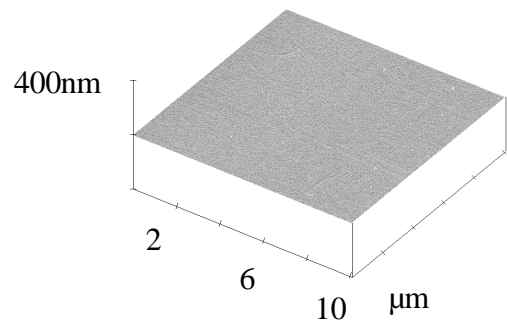


$12\text{BCl}_3/3\text{SF}_6$ , 200W ICP, 150W rf, 5mTorr  
RMS Roughness = 16.6nm

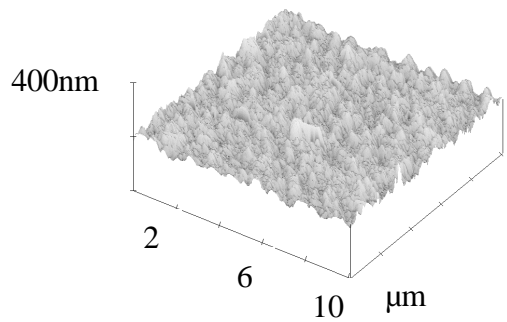


$12\text{BCl}_3/3\text{NF}_3$ , 200W ICP, 150W rf, 5mTorr  
RMS Roughness = 24.9nm

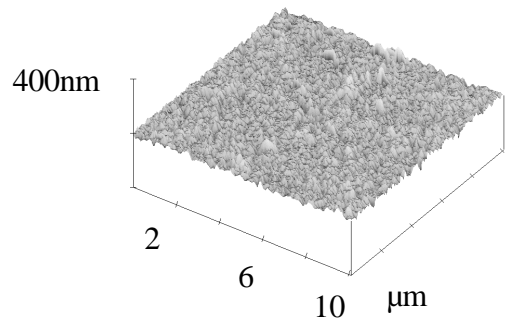
Figure 24. AFM scans of InGaP control sample (top), and samples etched in  $12\text{BCl}_3/3\text{SF}_6$  (middle), and  $12\text{BCl}_3/3\text{NF}_3$  (bottom) (200W source power, 150W rf chuck power, 5mTorr)



GaAs Control  
RMS Roughness = 0.4nm

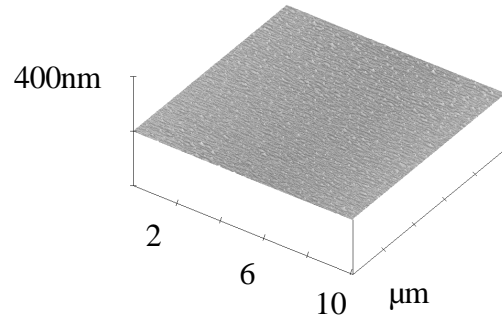


$12\text{BCl}_3/3\text{SF}_6$ , 200W ICP, 150W rf, 5mTorr  
RMS Roughness = 26.5nm

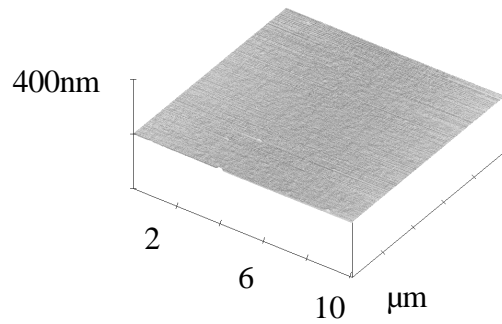


$12\text{BCl}_3/3\text{NF}_3$ , 200W ICP, 150W rf, 5mTorr  
RMS Roughness = 15.1nm

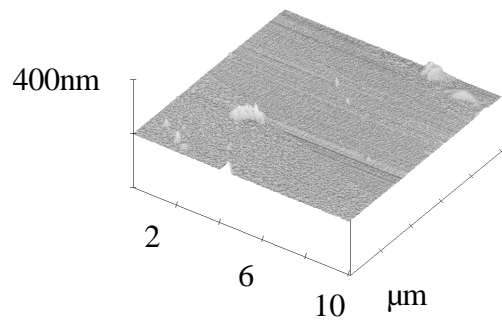
Figure 25. AFM scans of GaAs control sample (top), and samples etched in  $12\text{BCl}_3/3\text{SF}_6$  (middle), and  $12\text{BCl}_3/3\text{NF}_3$  (bottom) (200W source power, 150W rf chuck power, 5mTorr)



AlGaAs Control  
RMS Roughness = 1.3nm



12BCl<sub>3</sub>/3SF<sub>6</sub>, 200W ICP, 150W rf, 5mTorr  
RMS Roughness = 1.2nm



12BCl<sub>3</sub>/3NF<sub>3</sub>, 200W ICP, 150W rf, 5mTorr  
RMS Roughness = 4.7nm

Figure 26. AFM scans of AlGaAs control sample (top), and samples etched in 12BCl<sub>3</sub>/3SF<sub>6</sub> (middle), and 12BCl<sub>3</sub>/3NF<sub>3</sub> (bottom) (200W source power, 150W rf chuck power, 5mTorr)

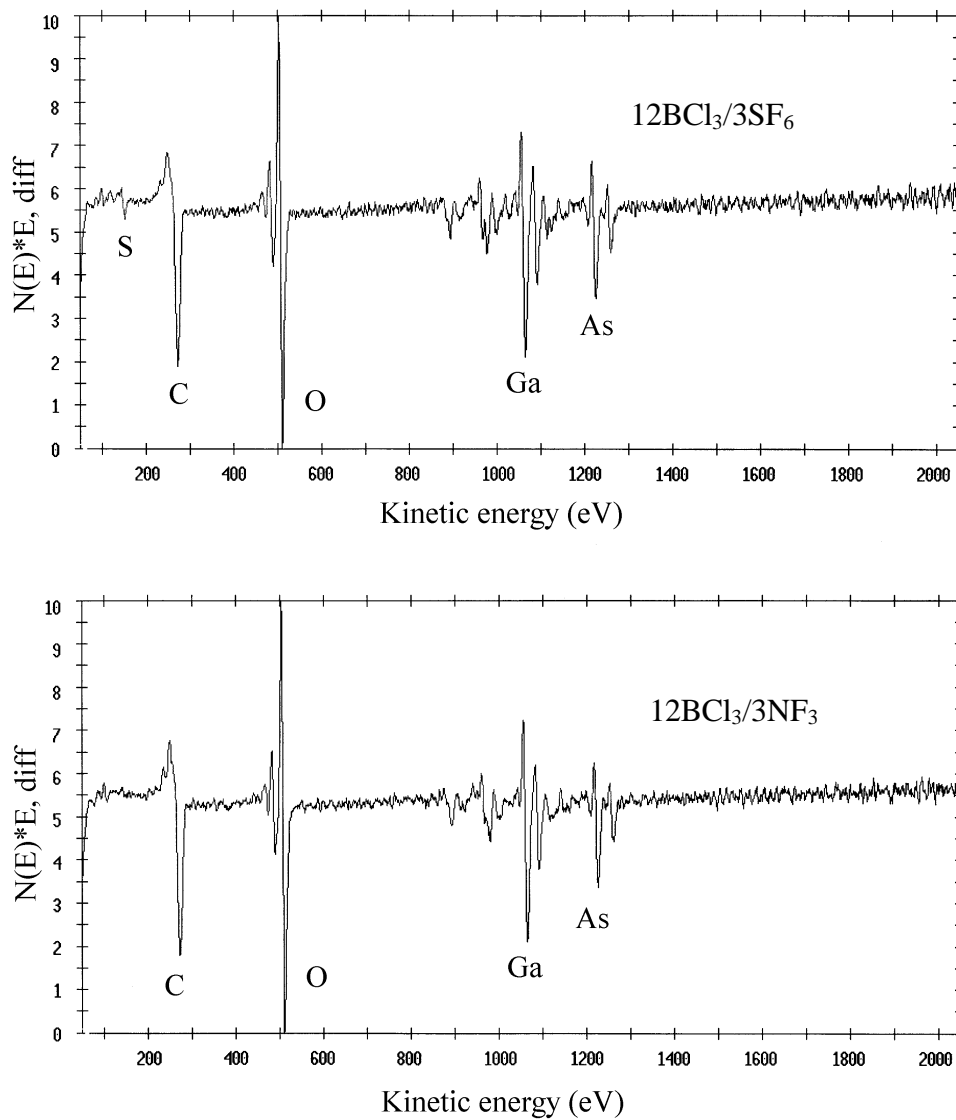


Figure 27. AES surface scans of GaAs etched in  $12\text{BCl}_3/3\text{SF}_6$  (top), and  $12\text{BCl}_3/3\text{NF}_3$  (bottom) (0W source power, 50W rf chuck power, 10mTorr)

(c) IBr and ICl

The interhalogen compounds are alternative etch chemistries for high density reactors because of their weak bonding and absence of polymer formation. Moreover,  $\text{InI}_3$  is much more volatile than  $\text{InCl}_3$ , leading to the possibility of selective etching of InGaP over GaAs.

Figure 28 shows the effects of ICl percentage on etch rates and selectivity under high source and chuck power conditions. The etch rates for AlGaAs are low over the whole range of ICl percentages investigated, producing selectivities up to  $\sim 30$  for GaAs over AlGaAs. This chemistry produces non-selective etching of the GaAs/InGaP heterostructure under these conditions, suggesting that at these biases and fluxes  $\text{InCl}_x$  desorption is not the limiting step. Lower biases and fluxes might produce better selectivity. The corresponding data for IBr/Ar discharges is shown in Figure 29. The same basic trends were obtained for this chemistry.

We also explored the effect of increasing source power at fixed plasma composition (i.e. 2ICl/13Ar ; 2IBr/13Ar), and found maximum selectivities  $< 10$  for GaAs/AlGaAs and typically 0.7-2 for GaAs/InGaP. The etched surface morphology was very good for these chemistries for a broad range of conditions (Figure 30), with root-mean-square (RMS) roughness in the range of 0.9-1.6 nm (i.e. similar to unetched controls), and excellent maintenance of stoichiometry as measured by Auger Electron Spectroscopy as shown in Figure 31 for ICl/Ar and Figure 32 for IBr/Ar. The latter measurements showed near-surface stoichiometries similar to the control samples.<sup>(25)</sup>

Typical data showing the influence of rf chuck power on etch rates and selectivities with these two chemistries are shown in Figures 33 and 34. The rates are a

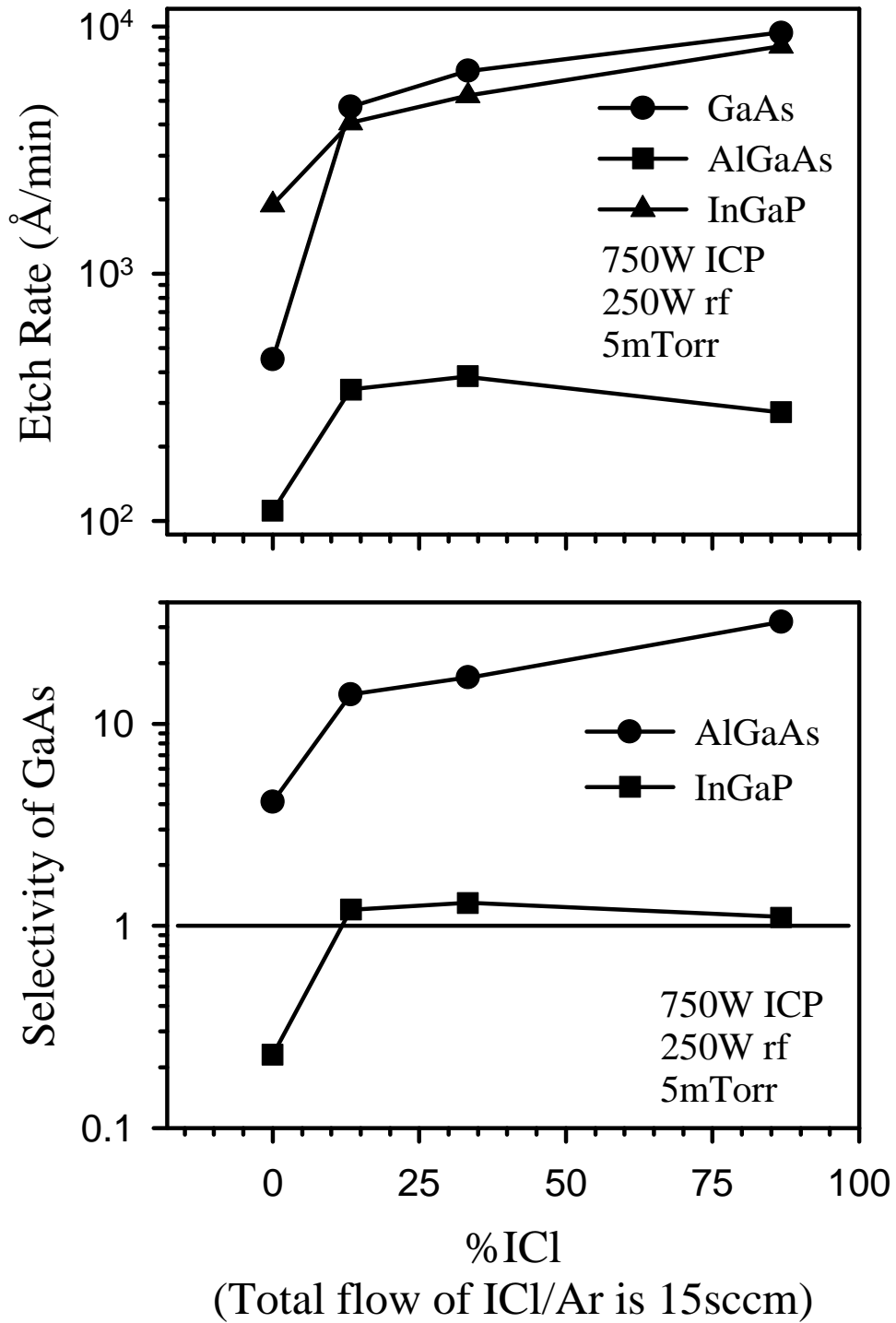


Figure 28. Etch rates of GaAs, AlGaAs, and InGaP(top) and resultant selectivities for GaAs over AlGaAs and InGaP(bottom) as a function of ICl percentage in ICP ICl/Ar discharges (750W source power, 250W rf chuck power, 5mTorr)

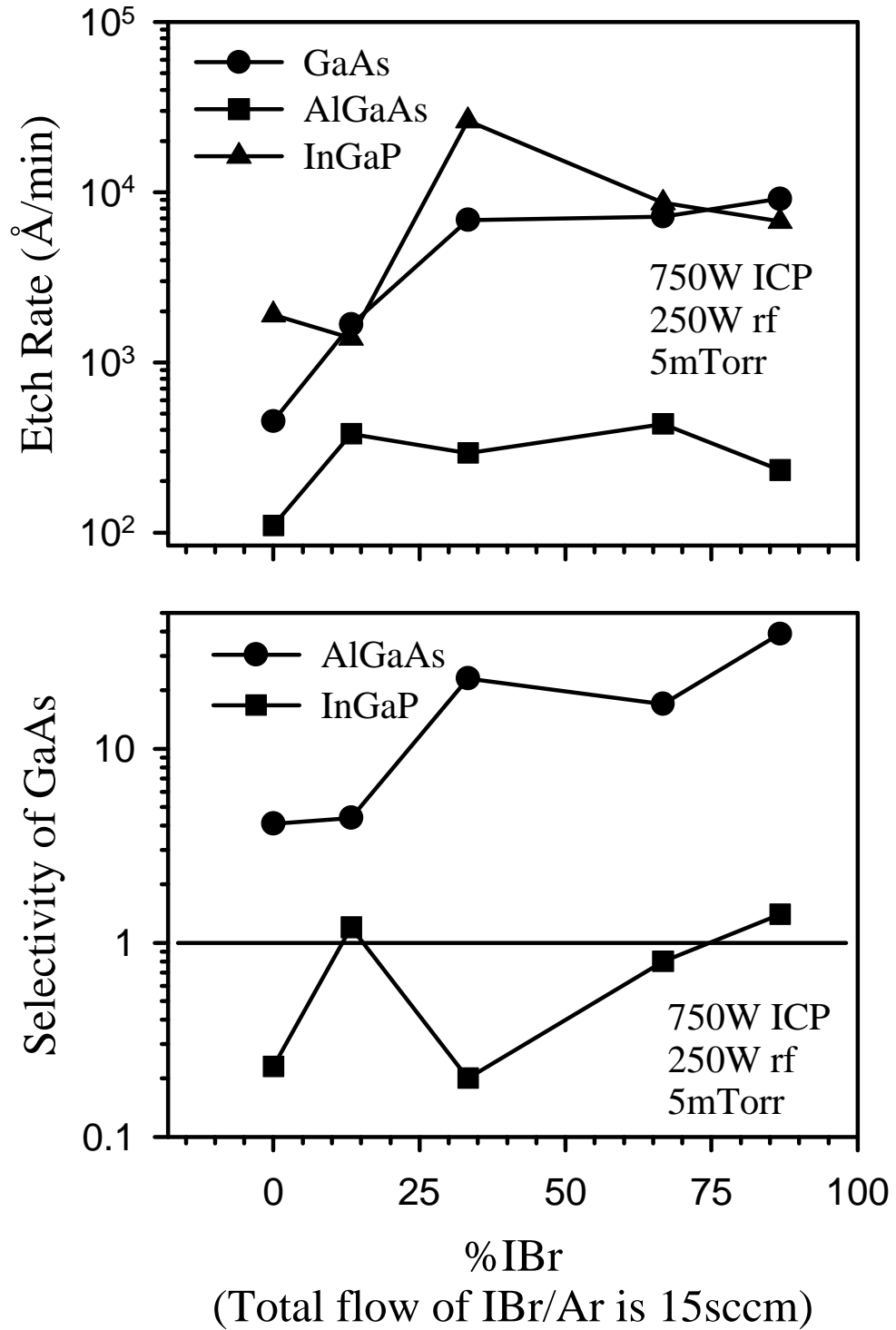
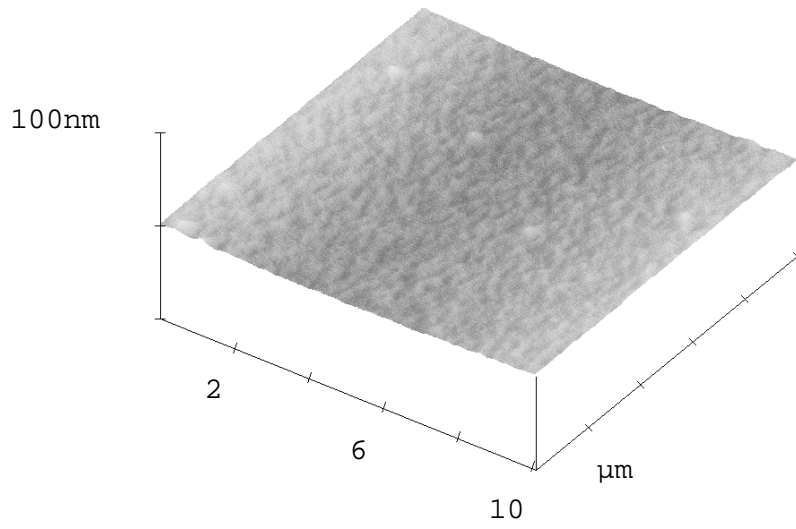
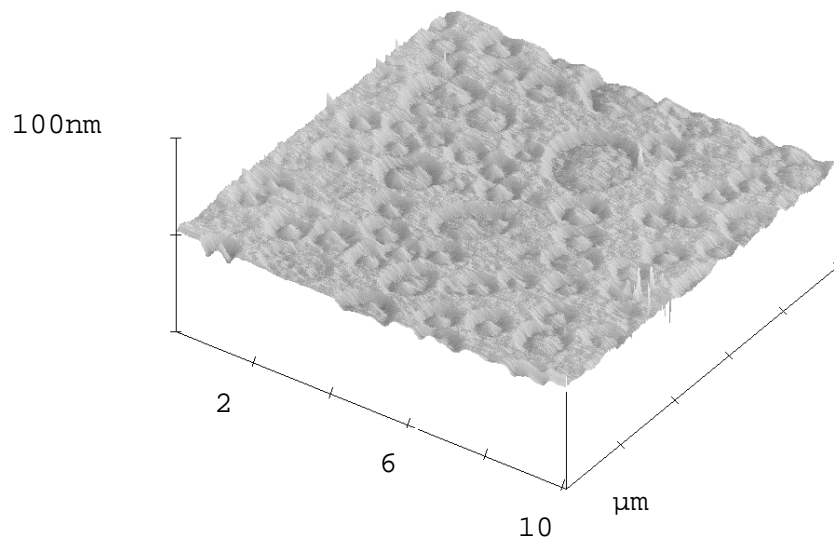


Figure 29. Etch rates of GaAs, AlGaAs, and InGaP(top) and resultant selectivities for GaAs over AlGaAs and InGaP(bottom) as a function of IBr percentage in ICP IBr/Ar discharges (750W source power, 250Wrf chuck power, 5mTorr)



ICl/Ar (RMS Roughness = 0.9nm)



IBr/Ar (RMS Roughness = 1.6 nm)

Figure 30. AFM scans of GaAs etched in 2ICl/13Ar (top) and 2IBr/13Ar (bottom) (750W source power, 250W rf chuck power, 5mTorr)

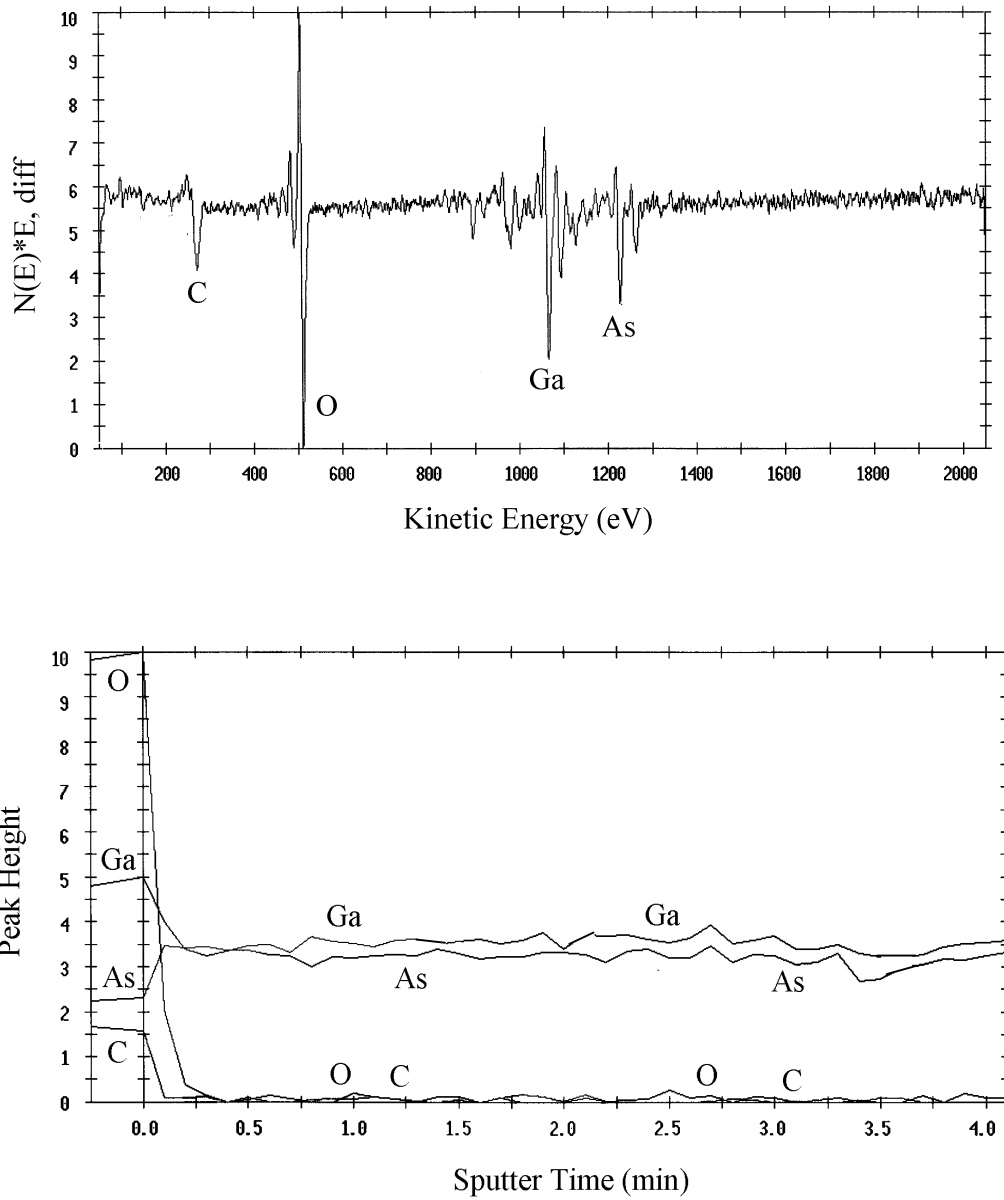


Figure 31. AES surface scan (top) and depth profile (bottom) of GaAs etched in  $2\text{ICl}/13\text{Ar}$  plasma at 750W source power, 250W rf chuck power and 5mTorr

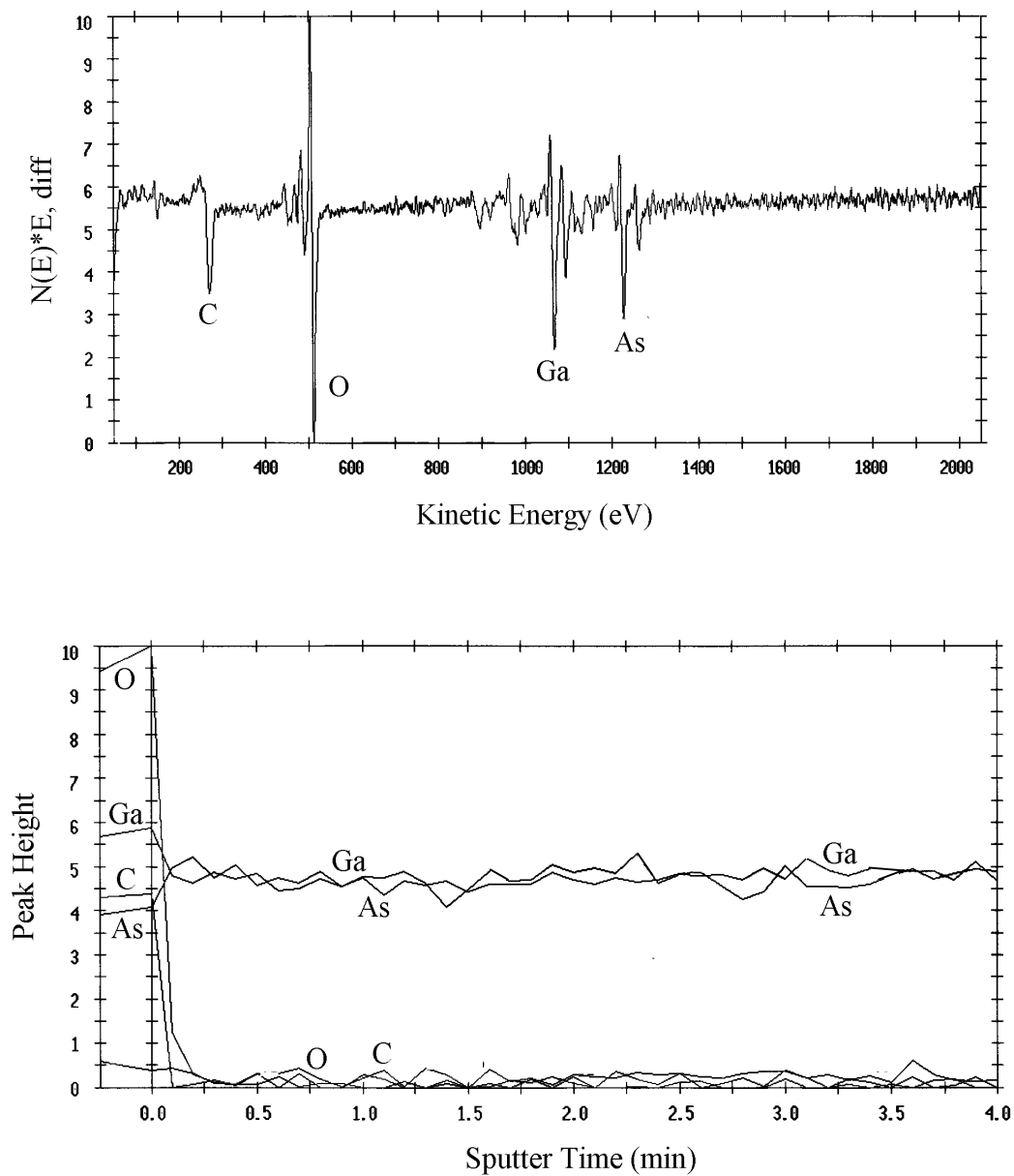


Figure 32. AES surface scan (top) and depth profile (bottom) of GaAs etched in 2IBr/13Ar plasma at 750W source power, 250W rf chuck power and 5mTorr

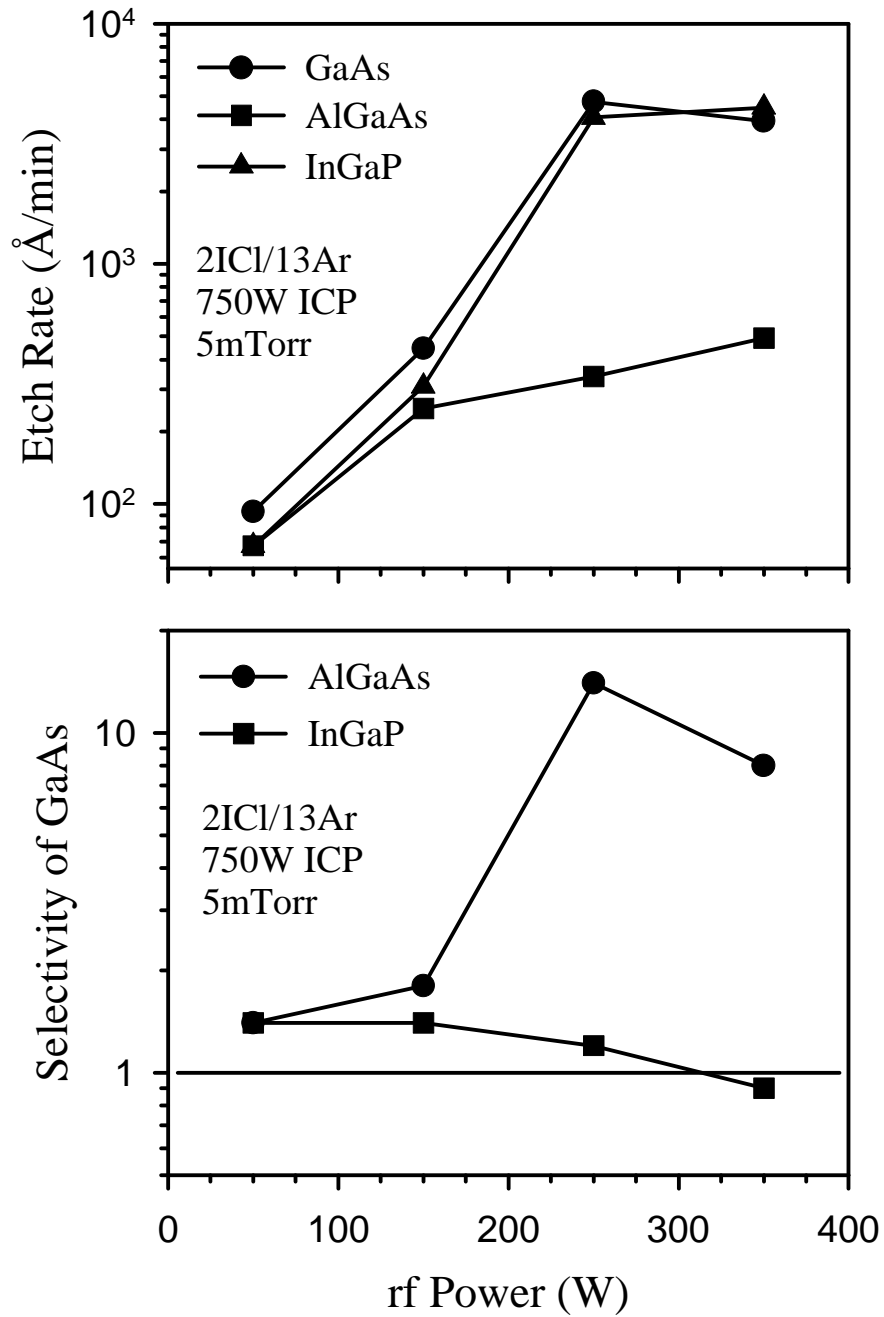


Figure 33. Etch rates of GaAs, AlGaAs, and InGaP(top) and resultant selectivities for GaAs over AlGaAs and InGaP(bottom) as a function of rf chuck power in ICP 2ICl/13Ar discharges (750W source power, 5mTorr)

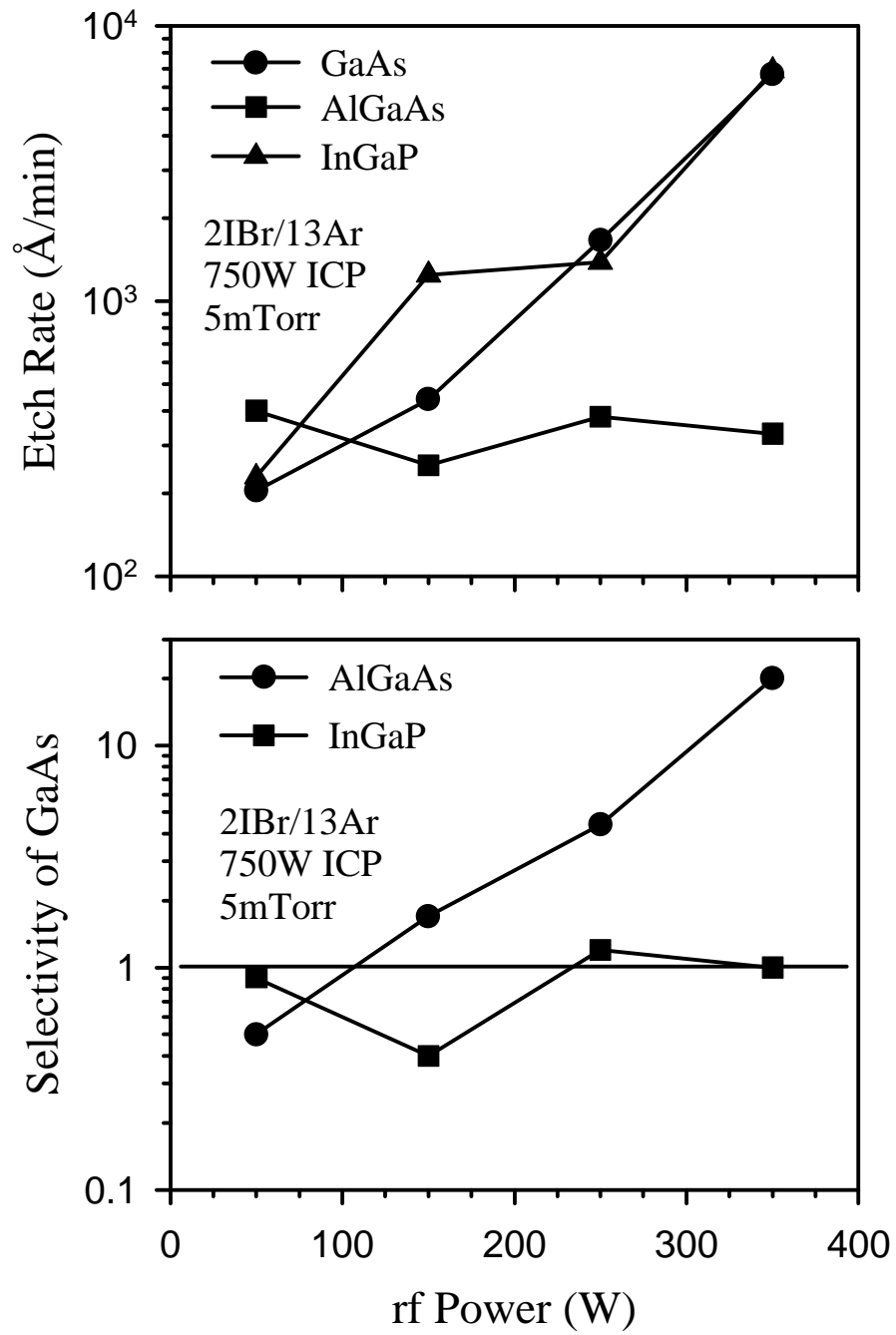


Figure 34. Etch rates of GaAs, AlGaAs, and InGaP(top) and resultant selectivities for GaAs over AlGaAs and InGaP(bottom) as a function of rf chuck power in ICP 2IBr/13Ar discharges (750W source power, 5mTorr)

strong function of ion energy, but the etching for both GaAs/AlGaAs and GaAs/InGaP is basically non-selective at low chuck powers. These do not appear to be attractive candidates for selective ICP etching.

(d)  $\text{BI}_3$  and  $\text{BBr}_3$

These compounds are the iodine and bromine analogs of  $\text{BCl}_3$ , and have only recently begun to be explored as etching chemistries for III-V semiconductors. Figure 35 shows the effect of  $\text{BI}_3$  percentage(top), source power(center), and chuck power(bottom) on GaAs and InGaP etch rates and the resultant selectivity for InGaP over GaAs. Note that values  $\sim 60$  can be achieved. This is an important result, since previously only  $\text{CH}_4/\text{H}_2$  has been found to produce selectivity for InGaP over GaAs. However, the use of  $\text{CH}_4/\text{H}_2$  has many attendant problems, including hydrogen passivation of near-surface dopants and polymer deposition on the mask material and within the chamber. The GaAs etch rate at low  $\text{BI}_3$  content, flux and ion energy is a sensitive function of ion/neutral ratio, and this is reflected in the variations in etch rate in Figure 35.

The corresponding data for  $\text{BBr}_3$  discharges is shown in Figure 36. We had to employ much higher rf chuck power with this chemistry to achieve measurable etch rates. The data show that  $\text{BBr}_3$  is essentially non-selective for GaAs/InGaP.

We summarize the selectivities for GaAs/AlGaAs and GaAs/InGaP achieved with the different chemistries under both RIE and ICP conditions in Table 2.

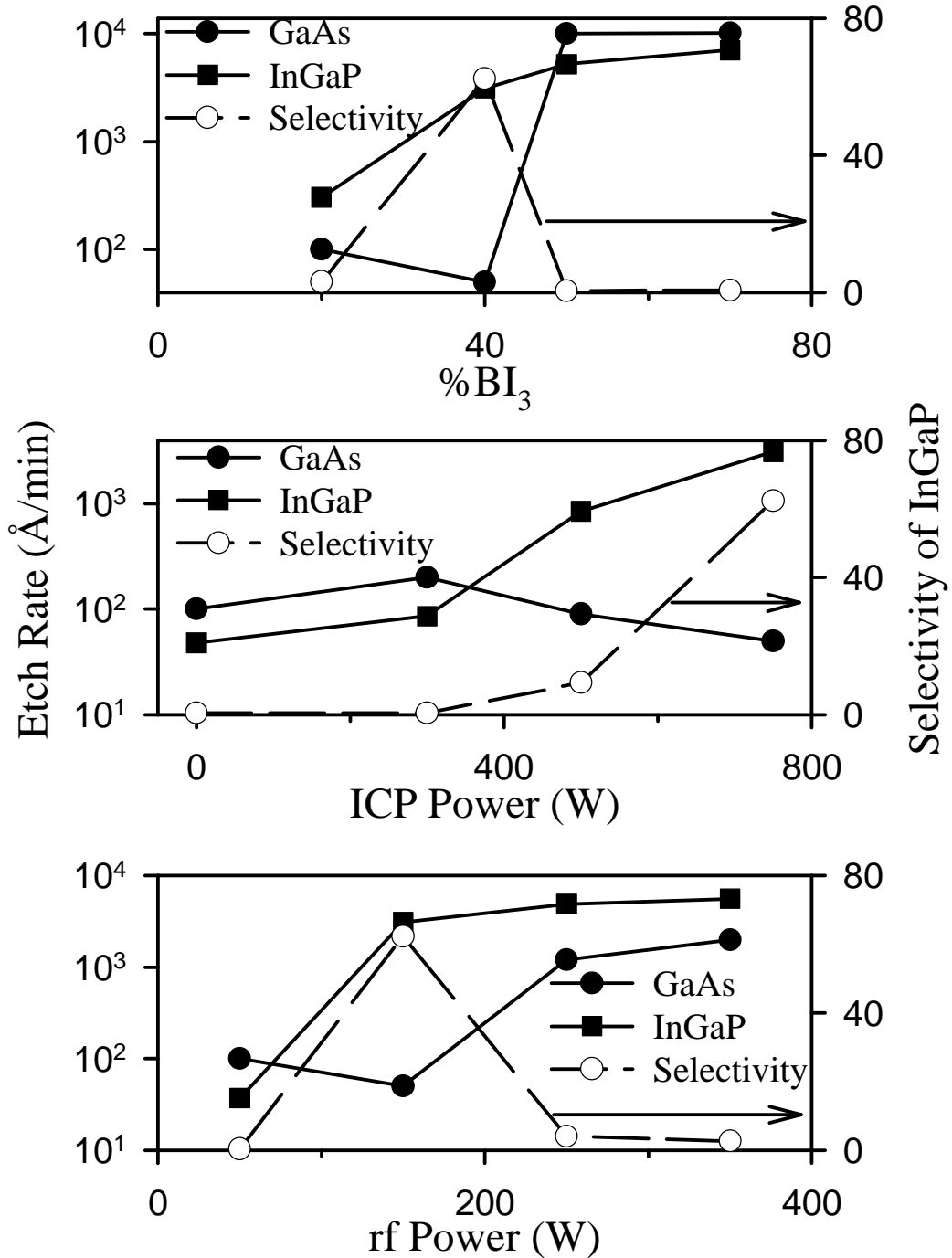


Figure 35. Etch rates of GaAs and InGaP and resultant selectivity for InGaP over GaAs as a function of BI<sub>3</sub> percentage at 750W source power, 150W rf chuck power(top), source power at fixed rf power of 150W(center) and rf power at fixed ICP power of 750W(bottom) in ICP BI<sub>3</sub>/Ar discharges (5mTorr)

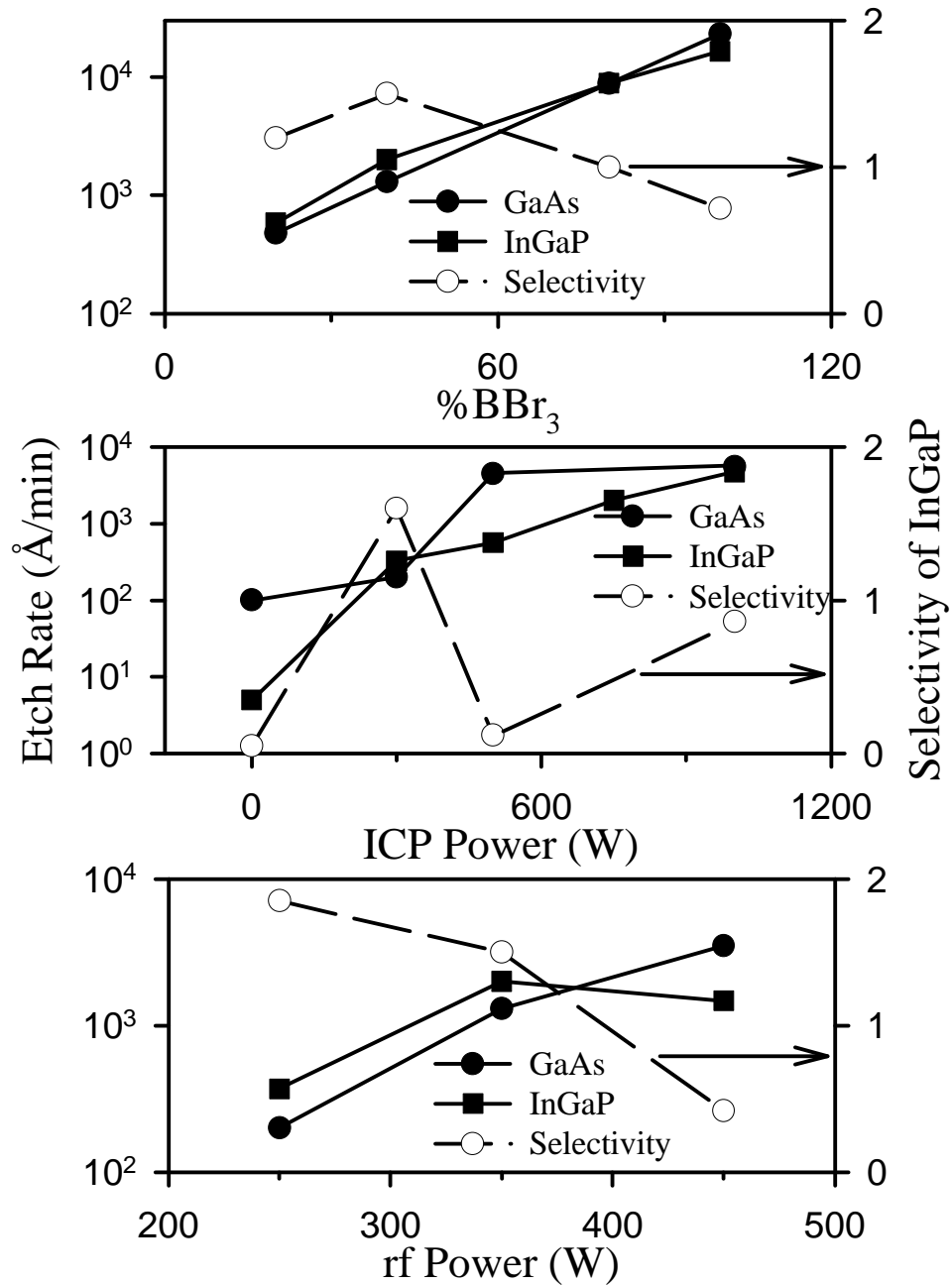


Figure 36. Etch rates of GaAs and InGaP and resultant selectivity for InGaP over GaAs as a function of BBr<sub>3</sub> percentage at 750W source power 250W rf chuck power(top), source power at fixed rf chuck power of 250W(center) and rf power at fixed ICP power of 750W(bottom) in ICP BBr<sub>3</sub>/Ar discharges (5mtorr)

Table 2. Dry etch selectivities for GaAs/AlGaAs and GaAs/InGaP under conventional RIE conditions and under high density plasma conditions in different plasma chemistries

Chemistry	GaAs/AlGaAs		GaAs/InGaP	
	<u>RIE</u>	<u>ICP</u>	<u>RIE</u>	<u>ICP</u>
BBr <sub>3</sub> /Ar	-	-	-	0.5-1
BI <sub>3</sub> /Ar	-	-	-	0.02-2
ICl/Ar	2	4-30	2	0.2-1
IBr/Ar	1	1-40	0.5	0.2-1
BCl <sub>3</sub> /SF <sub>6</sub>	Infinite	2-75	400	50-80
BCl <sub>3</sub> /NF <sub>3</sub>	1-50	1-30	1-75	1-25

## CHAPTER 5 DRY ETCHING OF InN/GaN/AlN

### 5.1 Materials and Methods

GaN, AlN and InN layers c-plane Al<sub>2</sub>O<sub>3</sub> substrates by Metal Organic Chemical Vapor Deposition (GaN)<sup>(65)</sup> or Metal Organic Molecular Beam Epitaxy (MOMBE).<sup>(63)</sup> In etch rate experiments they were masked with Apiezon wax, which was removed in acetone and the step height measured by stylus profilometry.

The vapor from ICl and IBr, contained in heated stainless-steel vessels, was introduced into the reactor through electronic mass flow controllers at a total gas load up to 15 standard cubic centimeters per minute(sccm). The Plasma Therm 790 ICP reactor was described in the previous chapter.

### 5.2 Results and Discussion

#### (a) ICl/Ar

Etch rates for the binary nitrides and resultant selectivities for InN over GaN and AlN are shown in Figure 37 as a function of discharge composition at fixed source power(750W) and rf chuck power(250W). The etch rates for AlN and GaN increase with ICl percentage, indicating some degree of chemical enhancement. The etch rate for InN is basically dominated singly by sputtering and is independent of discharge composition.

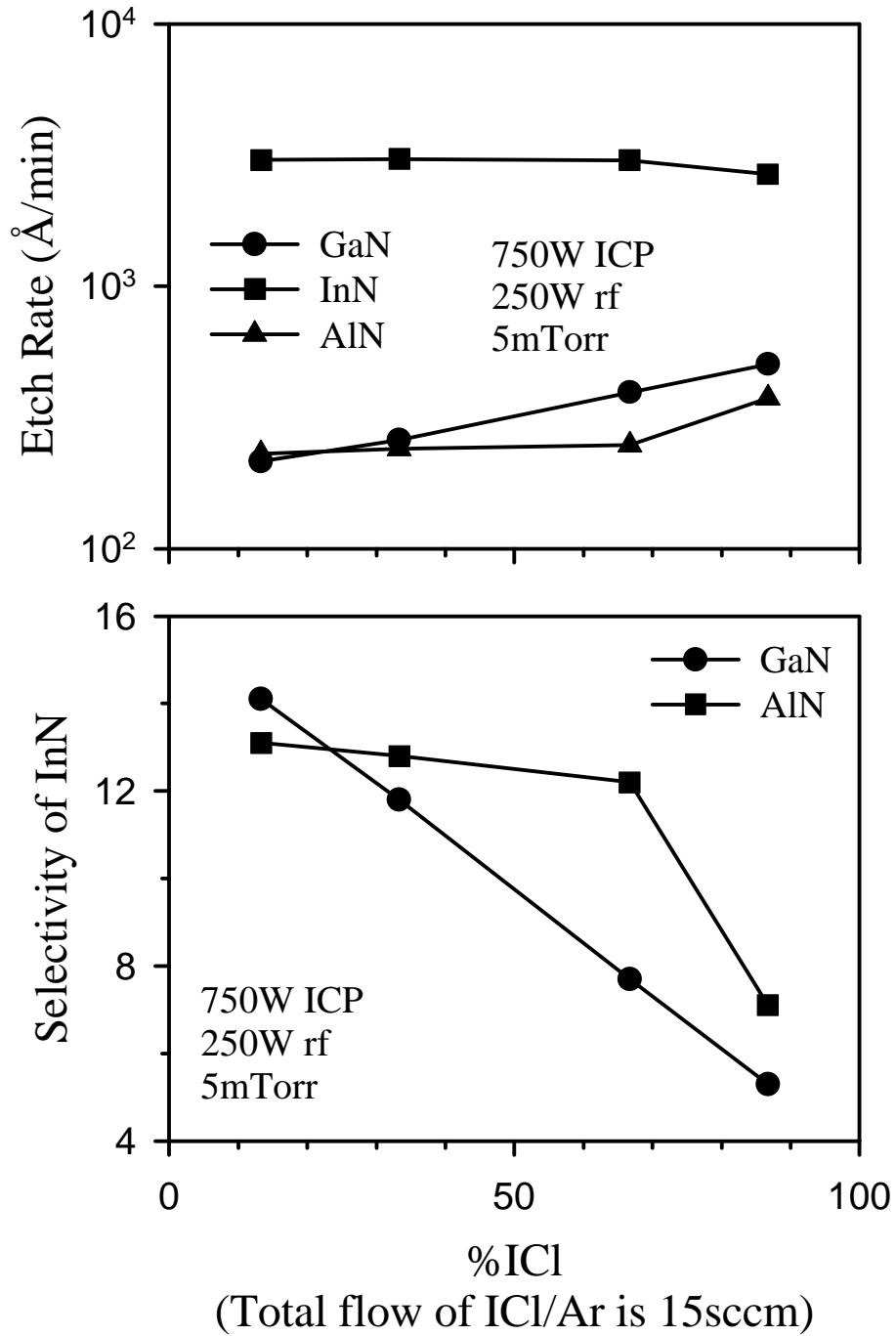


Figure 37. Etch rates of binary nitrides(top) and selectivity for InN over the other two materials(bottom) as a function of ICl percentage in ICP discharges (750W source power, 250W rf chuck power, 5mTorr)

Selectivities of 13 and 14, respectively, for InN/AlN and InN/GaN are achieved at low ICI percentages.

Results are shown in Figure 38 as a function of source power at the optimum discharge composition. The etch rates saturate beyond ~300W source power, producing similar behavior in the selectivity. In device fabrication a selectivity of >10 is desirable for process repeatability, and this is achieved for both InN/GaN and InN/AlN. These results also show the value of using high density plasma conditions for etching of the nitrides, since the rates are 1-2 orders of magnitude higher than for RIE conditions (i.e. 0W source power).<sup>(66)</sup>

The results as a function of process pressure are shown in Figure 39. The effects of increasing pressure include an increase in reactive neutral density, but a reduction in effective ion energy. These competing trends produce either maxima or minima in the etch rates. Since the InN etch mechanism is strongly ion-assisted, the rate falls off at high process pressure and reduces the selectivity with respect to both GaN and AlN. An excellent maximum selectivity of ~55 for InN/GaN was achieved at 10mTorr.

The relatively high bond strength for the nitrides (7.72eV/atom for InN, 8.92eV/atom for GaN, and 11.52eV/atom for AlN)<sup>(67)</sup> means that bond-breaking prior to formation of the etch products is often the rate-limiting step. The incident ion energy is basically controlled by the rf chuck power. Figure 40 shows the effect of this parameter on nitride etch rates and selectivities. The rates saturate above ~150W (corresponding to dc self-bias of ~ -125V), where the etching becomes reactant-limited. The selectivity for InN over both materials is quite good over a broad range of rf chuck power.

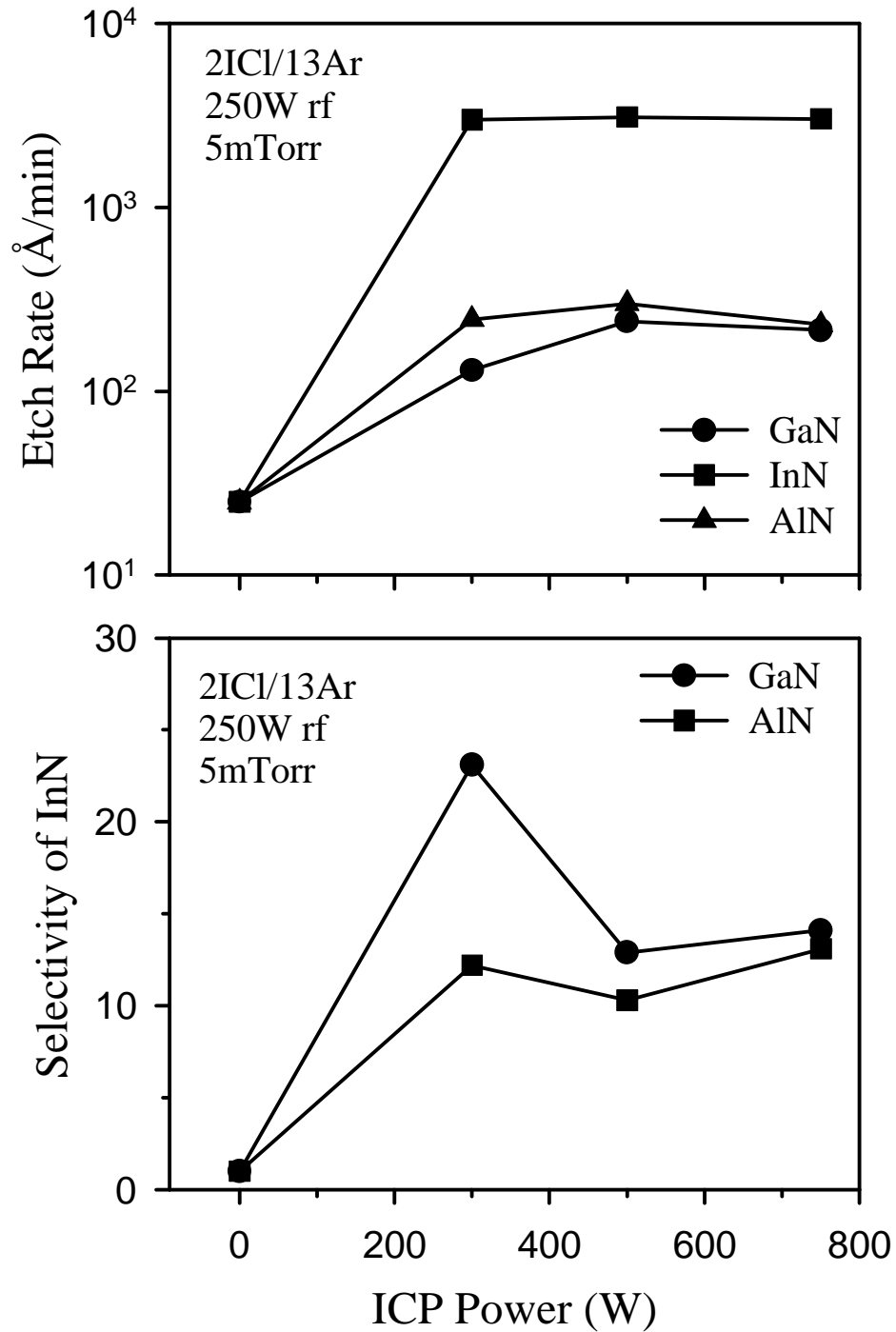


Figure 38. Etch rates of binary nitrides(top) and selectivity for InN over the other two materials(bottom) as a function of source power in ICP discharges (250W rf chuck power, 5mTorr) of 2ICl/13Ar

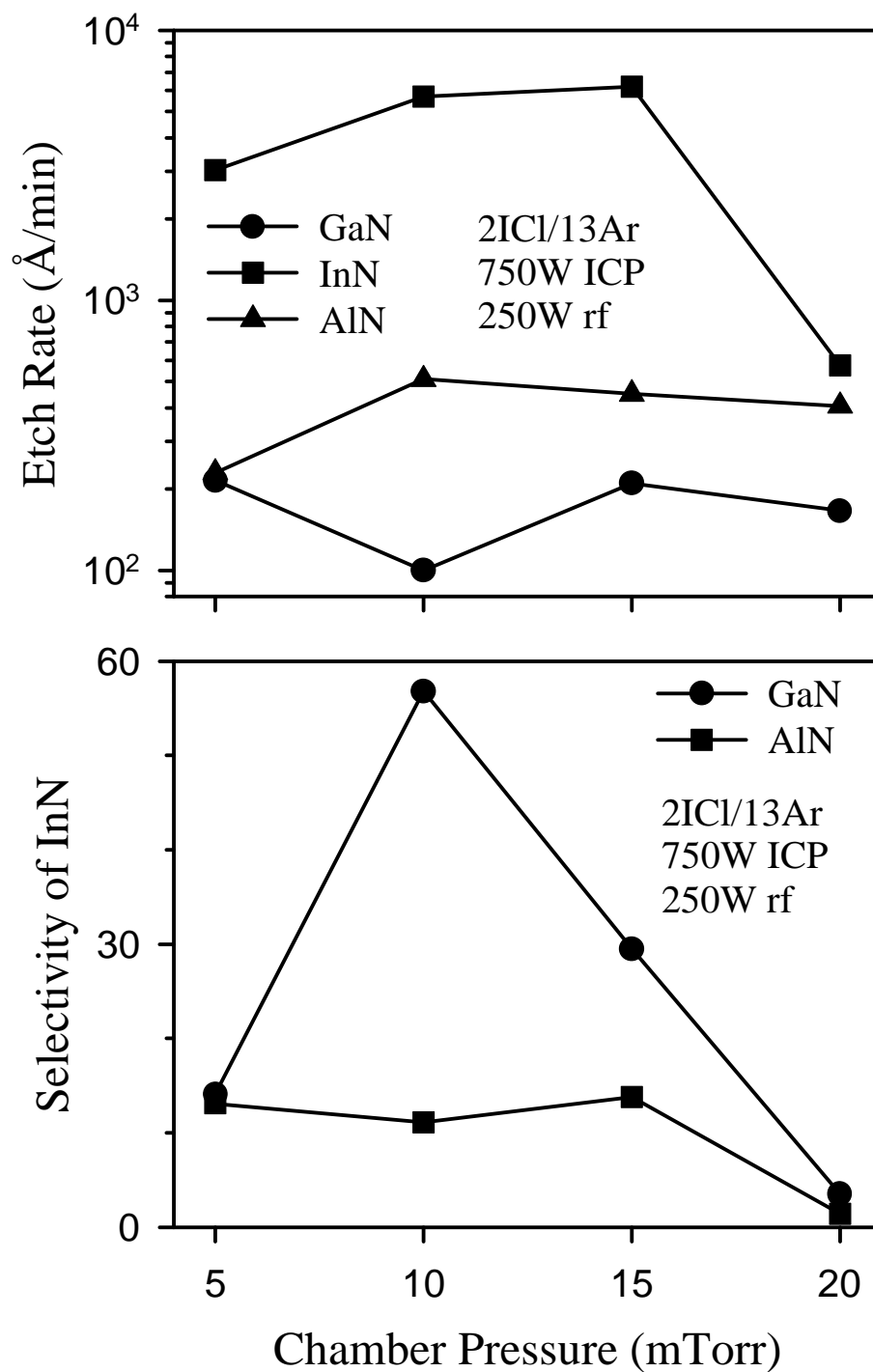


Figure 39. Etch rates of binary nitrides(top) and selectivity for InN over the other two materials(bottom) as a function of pressure in ICP discharges (750W source power, 250W rf chuck power) of 2ICl/13Ar

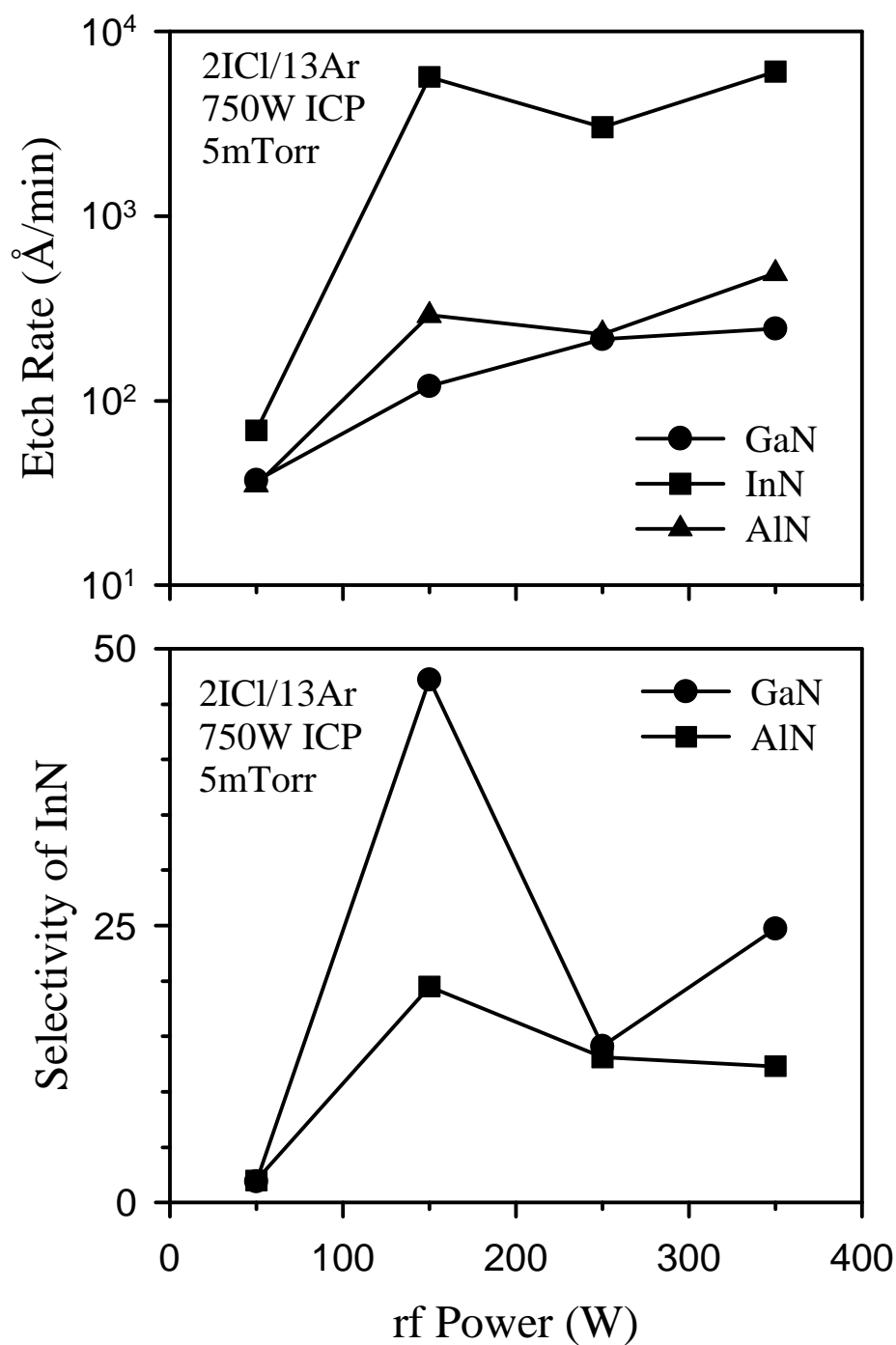


Figure 40. Etch rates of binary nitrides(top) and selectivity for InN over the other two materials(bottom) as a function of rf chuck power in ICP discharges (750W source power, 5mTorr) of 2ICl/13Ar

(b) IBr/Ar

The same experiments were performed for the IBr chemistry. Figure 41 shows the effect of plasma composition on the material etch rates and selectivity. The results are fairly similar to those obtained with the ICl mixtures (Figure 37) and maximum selectivities  $>10$  were achieved for both InN/GaN and InN/AlN.

The effect of ICP source power on the etching with IBr/Ar is shown in Figure 42. The overall trends are again similar to those obtained with ICl/Ar, with the only significant difference being that the GaN etch rate has not yet saturated at 750W source power. Maximum selectivities are again  $>10$ , and the rates under ICP conditions are much higher than the 0W RIE condition.

The IBr/Ar mixtures were ineffective for etching at pressures above 10mTorr, as shown in Figure 43. The ion-to-neutral ratio most likely falls below the threshold for etching to occur, and the surface becomes blocked to etch product desorption. This is another reason why high density tools are attractive for etching of III-nitrides, since they operate at low pressures (typically 1-5mTorr) relative to RIE systems (50-200mTorr).

Figure 44 shows the effect of rf chuck power on etch rates and selectivity. The overall behavior is again very similar to that found with ICl/Ar, with the etch rates saturating at higher chuck powers. The selectivities are slightly lower than obtained with the ICl/Ar chemistry.

Etch morphology was examined using AFM for GaN samples etched at 750 W ICP power, 250 W rf chuck power and 5 mTorr in 2ICl/13Ar and 2IBr/13Ar discharges, respectively and the results are shown in Figure 45. It is seen that the IBr/Ar chemistry (bottom) shows somewhat better morphology than ICl/Ar, resulting in overall mirror-like

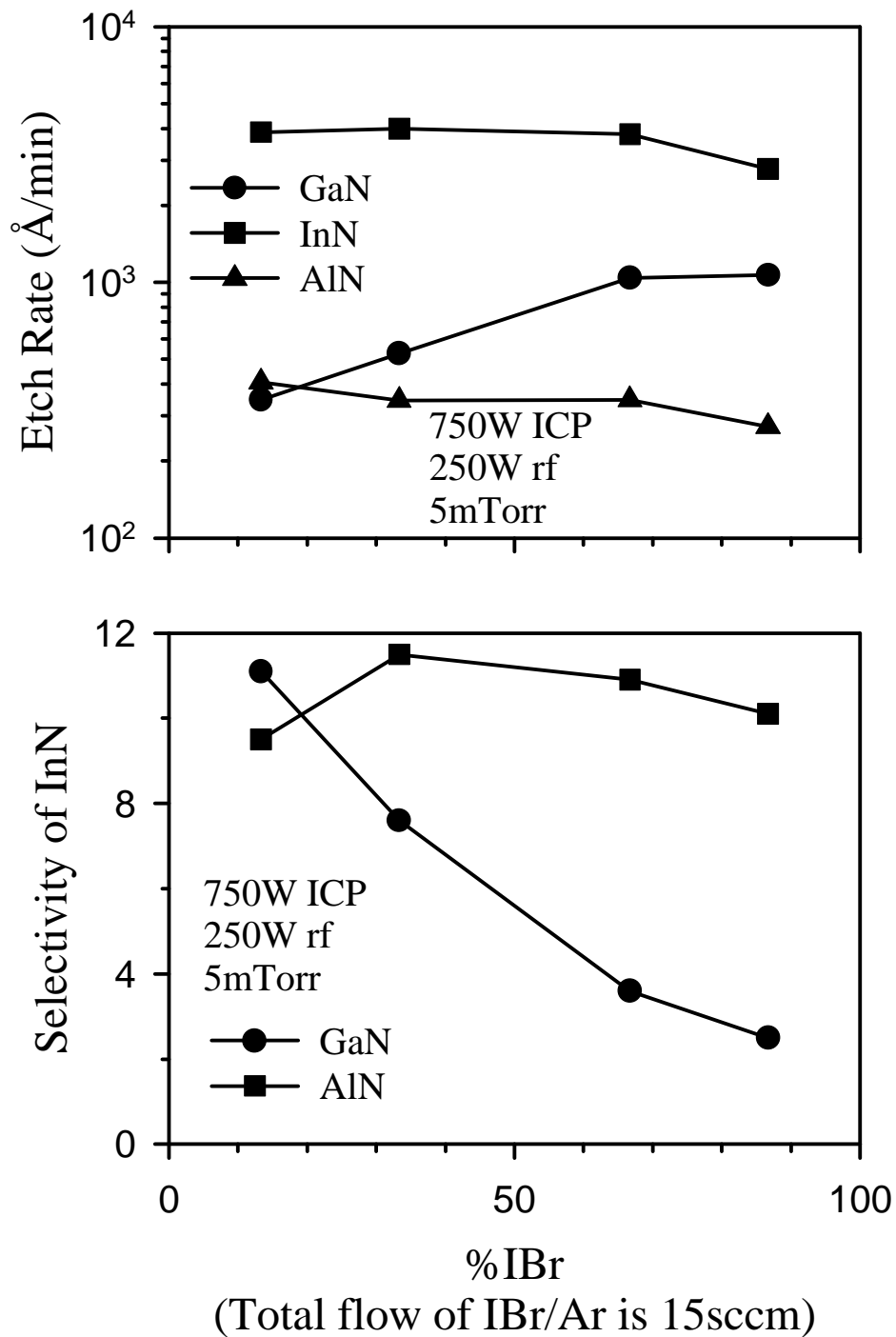


Figure 41. Etch rates of binary nitrides(top) and selectivity for InN over the other two materials(bottom) as a function of IBr percentage in ICP discharges (750W source power, 250W rf chuck power, 5mTorr)

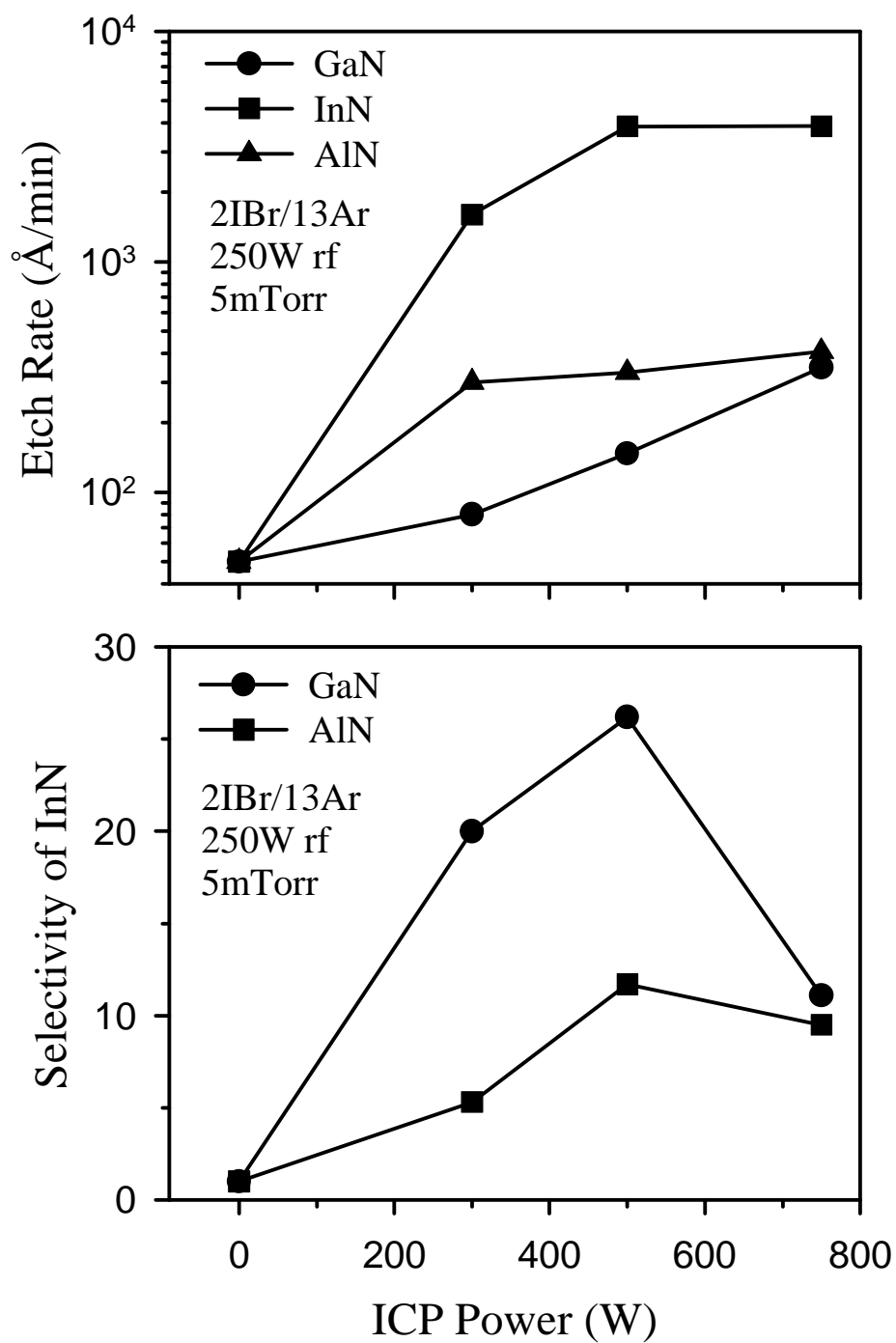


Figure 42. Etch rates of binary nitrides(top) and selectivity for InN over the other two materials(bottom) as a function of source power in ICP discharges (250W rf chuck power, 5mTorr) of 2IBr/13Ar

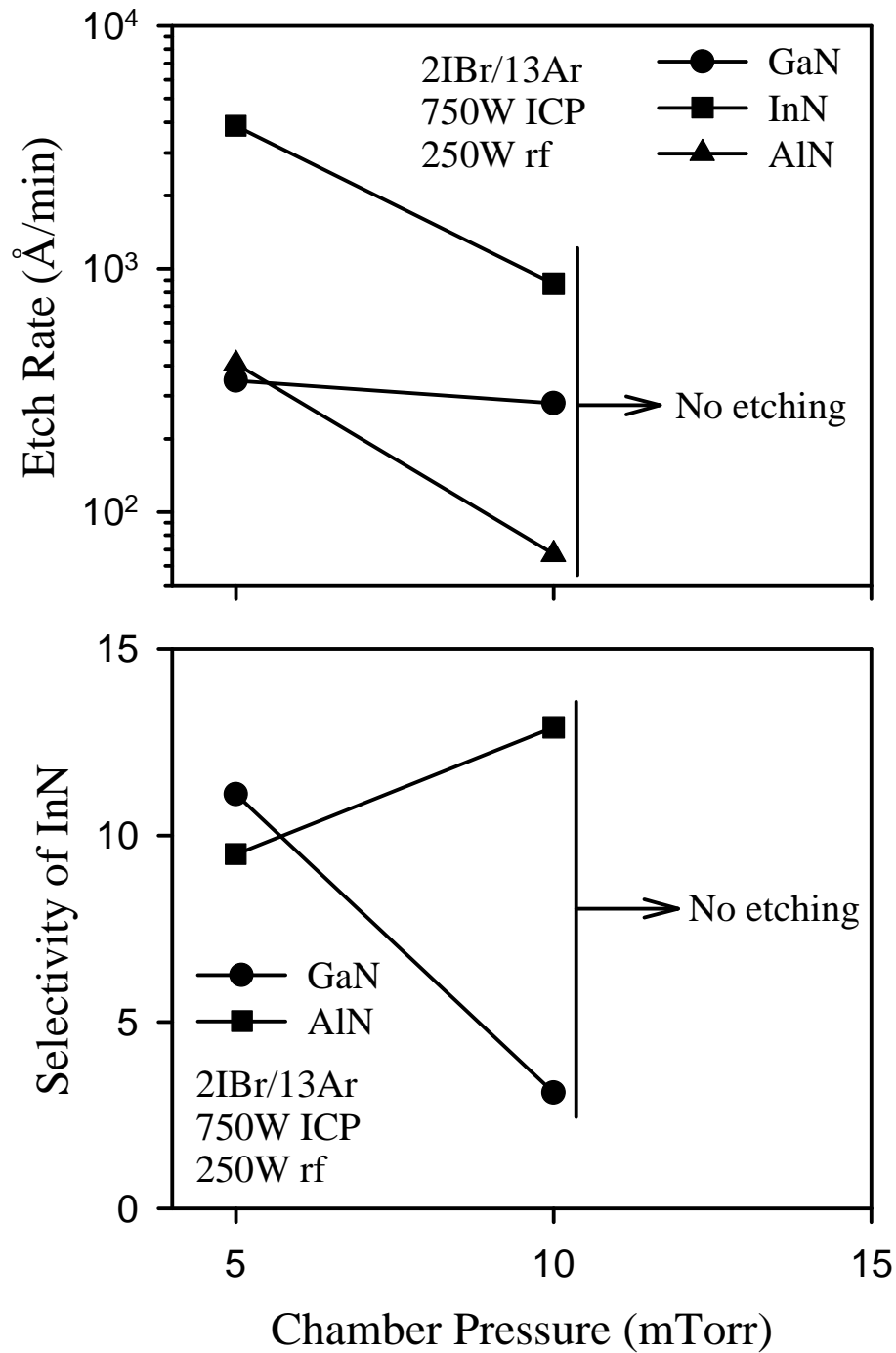


Figure 43. Etch rates of binary nitrides(top) and selectivity for InN over the other two materials(bottom) as a function of pressure in ICP discharges (750W source power, 250W rf chuck power) of 2IBr/13Ar

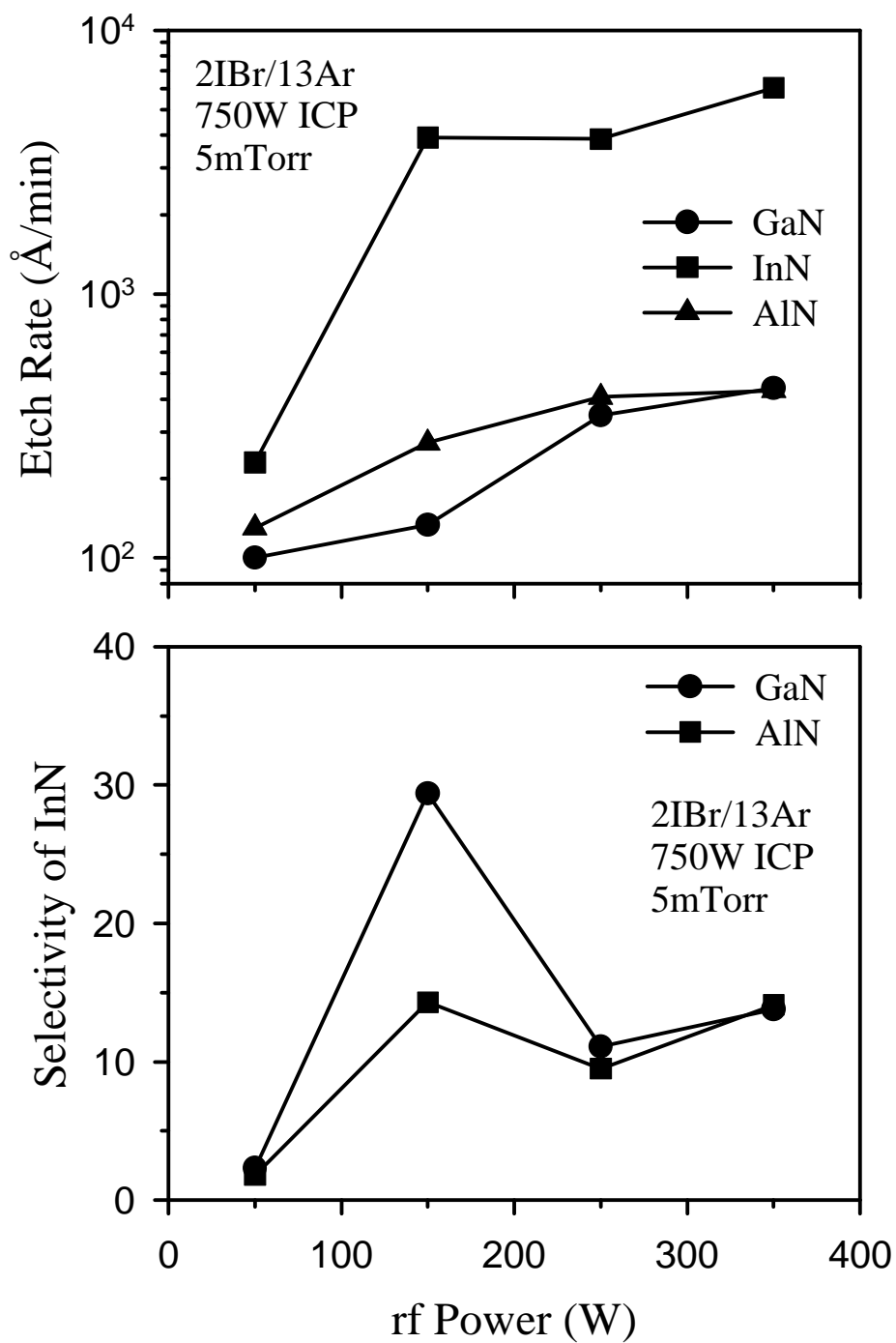


Figure 44. Etch rates of binary nitrides(top) and selectivity for InN over the other two materials(bottom) as a function of rf chuck power in ICP discharges (750W source power, 5mTorr) of 2IBr/13Ar

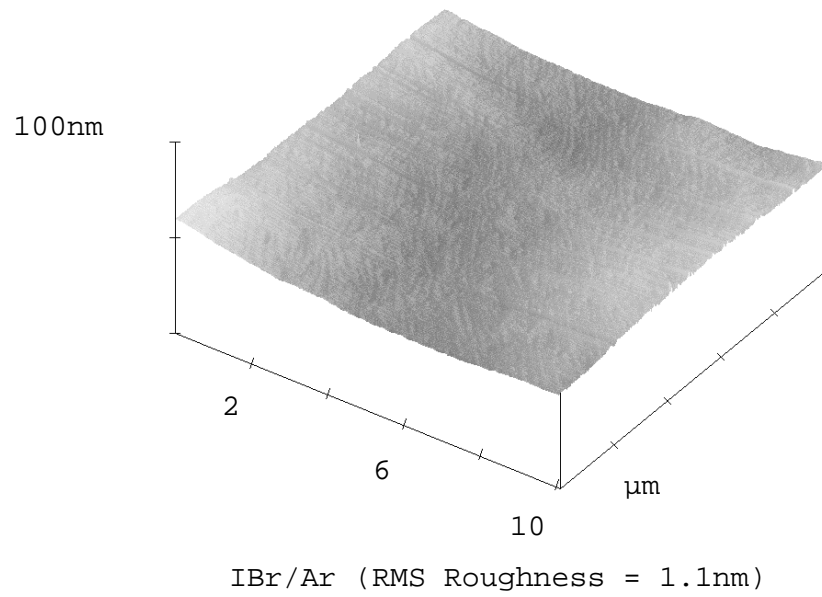
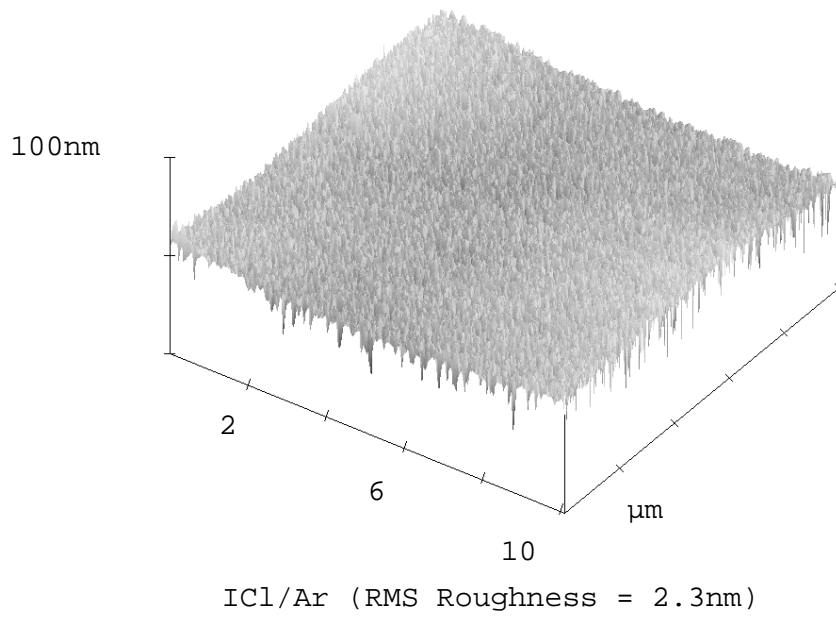


Figure 45. AFM scans for GaN etched in 2ICl/13Ar (top) and 2IBr/13Ar (bottom) (750 W source power, 250W rf chuck power, 5mTorr)

smoothness in both chemistries. The near surface composition was also examined using Auger Electron Spectroscopy (AES) and showed an excellent maintenance of stoichiometry as compared to control samples. Figure 46 shows an AES surface scan and depth profile in  $2\text{ICl}/13\text{Ar}$  and shows no chlorine contamination on the surface. Similar results were obtained for  $\text{IBr}/\text{Ar}$  chemistries showing no Bromine contamination.

(c)  $\text{Cl}_2/\text{He}$ ,  $\text{Cl}_2/\text{Ar}$ , and  $\text{Cl}_2/\text{Xe}$

Figures 47 and 48 show the effect of  $\text{Cl}_2$  concentration on etch rates of InN, AlN and GaN in  $\text{Cl}_2/\text{He}$ ,  $\text{Cl}_2/\text{Ar}$  and  $\text{Cl}_2/\text{Xe}$  discharges at 5 mTorr, 750 W source power and 250 W rf chuck power. It is seen that the effects of noble gas additives are strongly dependent on the particular III-nitride material: the highest etch rates for InN were obtained with  $\text{Cl}_2/\text{Xe}$  (Figure 47, top) and for AlN (bottom) and GaN (Figure 48, top) with  $\text{Cl}_2/\text{He}$ . It is also seen that etch rates of AlN and GaN were much lower in chlorine-based plasmas compared to InN. The high rates for the latter are similar to the previously reported results observed for InP where efficient ion-assisted desorption of the  $\text{InCl}_x$  occurs under ICP conditions.<sup>(68)</sup> These results indicate that the etch mechanism is dependent on material bond strengths and on the particular plasma chemistry employed, and optimization of the ICP etching process is crucial for obtaining the best results.

The highest etch rates for AlN and GaN at these low bias conditions were obtained with  $\text{Cl}_2/\text{He}$  discharges:  $\sim 300 \text{ \AA}/\text{min}$  for AlN and  $\sim 500 \text{ \AA}/\text{min}$  for GaN at 66.7 %  $\text{Cl}_2$ . According to a self-consistent model developed for the ICP system having a cylindrical geometry,<sup>(69)</sup> ion fluxes and Bohm velocities at the sheath edge at 66.7 %  $\text{Cl}_2$  are, respectively,  $1.59 \times 10^{16} \text{ cm}^{-2}\text{s}^{-1}$  ( $\text{Cl}_2/\text{Ar}$ ),  $1.84 \times 10^{16} \text{ cm}^{-2}\text{s}^{-1}$  ( $\text{Cl}_2/\text{He}$ ) and  $1.92 \times 10^{16}$

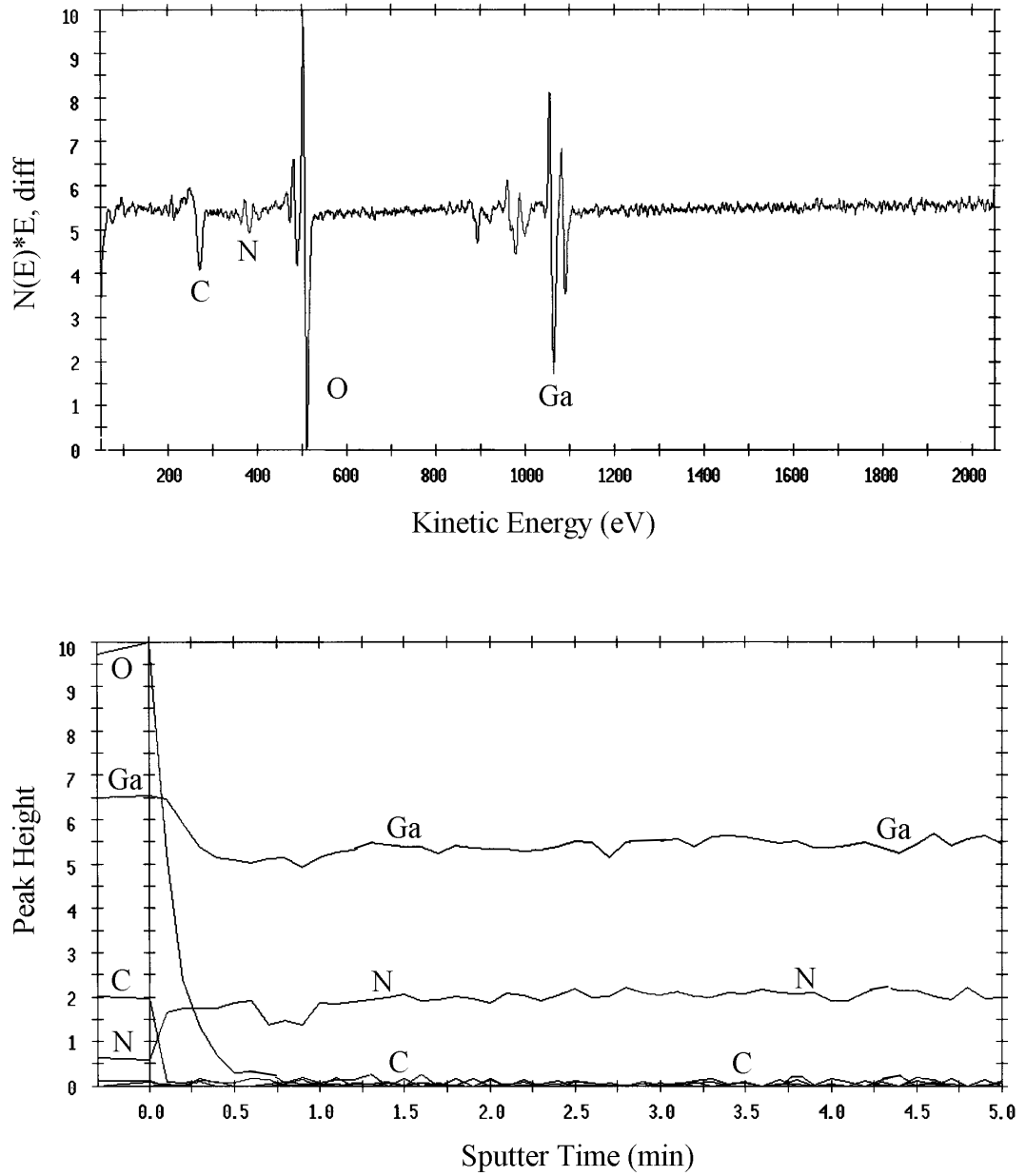


Figure 46. AES surface scan (top) and depth profile (bottom) of GaN  
(2ICl/13Ar, 750W source power, 250W rf chuck power,

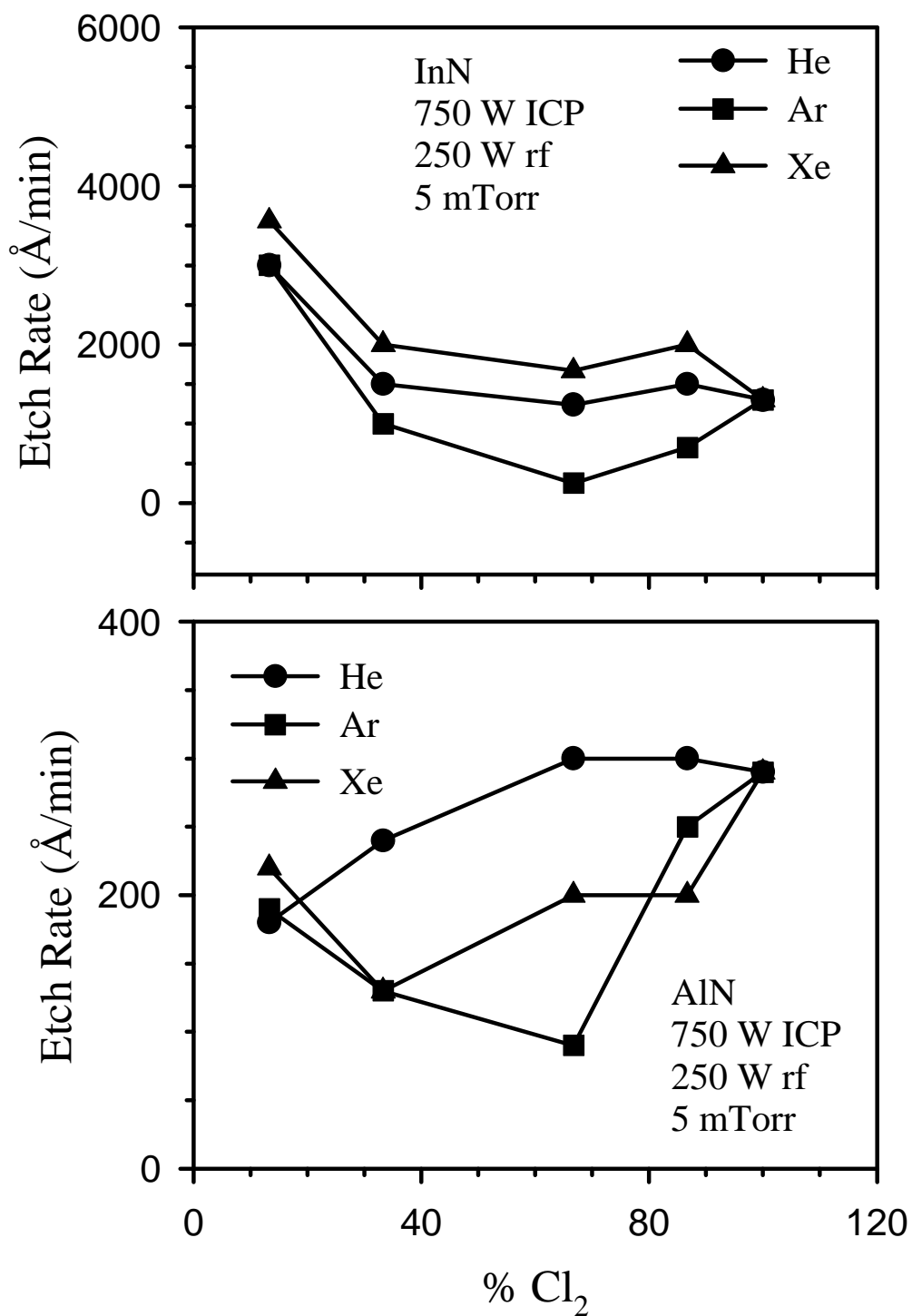


Figure 47. Effect of chlorine concentration on etch rates of InN (top) and AlN (b) with Cl<sub>2</sub>/He, Cl<sub>2</sub>/Ar and Cl<sub>2</sub>/Xe plasma chemistries (750 W source power, 250 W rf chuck power, 5 mTorr)

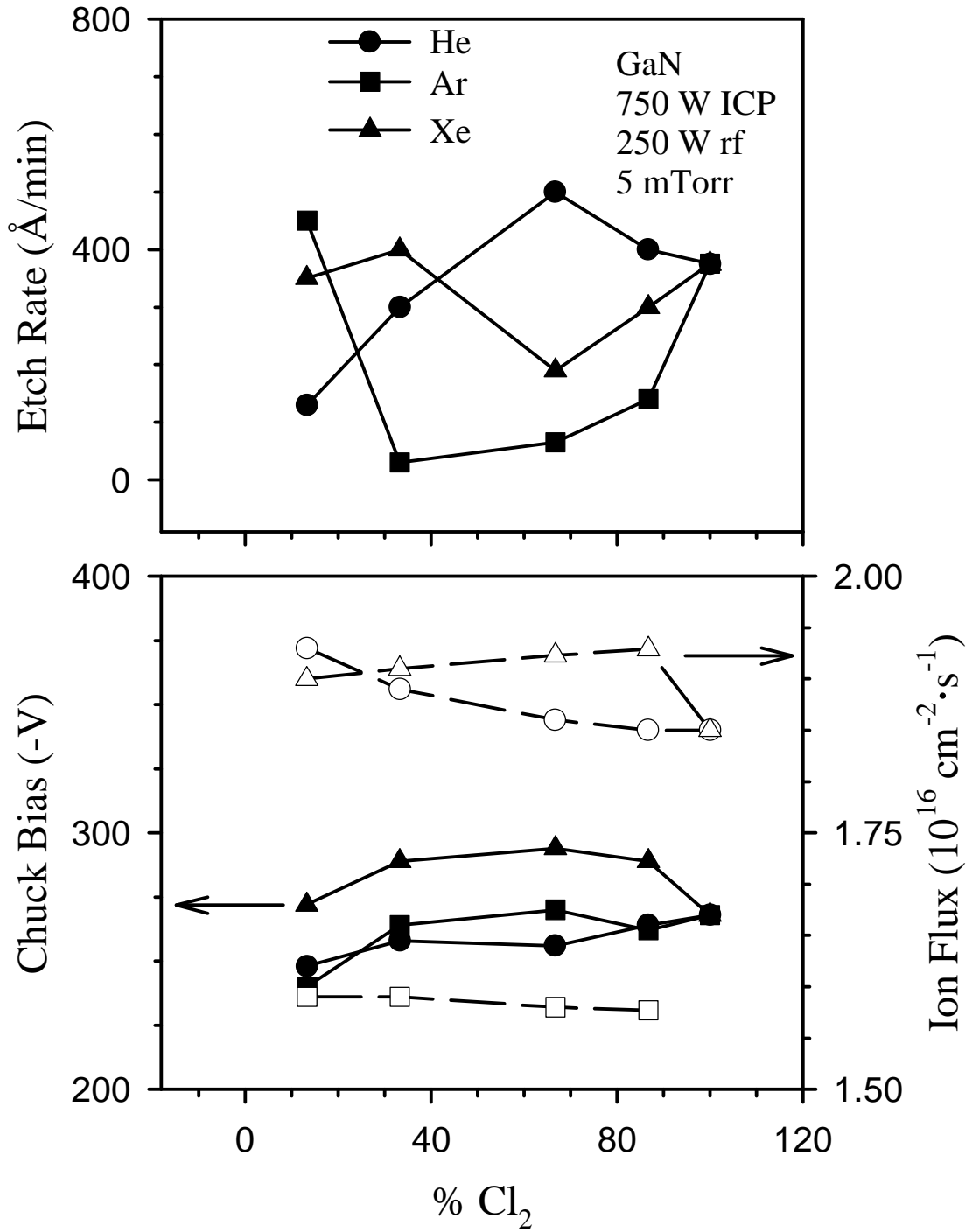


Figure 48. Effect of chlorine concentration on etch rates of GaN (top) and on dc bias and ion flux at the sheath edge (bottom) with  $\text{Cl}_2/\text{He}$ ,  $\text{Cl}_2/\text{Ar}$  and  $\text{Cl}_2/\text{Xe}$  plasma chemistries (750 W source power, 250 W rf chuck power, 5 mTorr)

$\text{cm}^{-2}\text{s}^{-1}$  ( $\text{Cl}_2/\text{Xe}$ ), and 1,740 m/s ( $\text{Cl}_2/\text{Xe}$ ), 2,350 m/s ( $\text{Cl}_2/\text{Ar}$ ) and 2,660 m/s ( $\text{Cl}_2/\text{He}$ ). That is, the  $\text{Cl}_2/\text{Xe}$  discharges showed the highest ion flux at the sheath edge, while the ions created by  $\text{Cl}_2/\text{He}$  discharge have the greatest Bohm velocity. It is interesting to see that the ion fluxes and sheath edge velocities are in the same order as we expected based on ionization energy [ $\text{Ar}$  (15.76 eV) >  $\text{He}$  (13.6 eV) >  $\text{Xe}$  (12.13 eV)]<sup>(57)</sup> and atomic mass. The predicted ion fluxes and Bohm velocities explain why the etch rates with  $\text{Cl}_2/\text{Ar}$  are the lowest, while the highest are obtained with  $\text{Cl}_2/\text{He}$ . Ions created in the  $\text{Cl}_2/\text{He}$  discharge, having the fastest velocity, arrive at the surface with higher velocities, helping activate the nitride surface for the coincident reactive chlorine neutral flux. They also provide the impetus for directional etching. In the ICP system, the sheath layer near the sample position is determined mainly by the capacitively coupled power because the sheath thickness due to the inductively coupled power is much smaller. The values of sheath thickness predicted at 66.7%  $\text{Cl}_2$ , 750 W ICP and 250 W rf powers are 0.62 cm in  $\text{Cl}_2/\text{He}$ , and 0.44 cm in  $\text{Cl}_2/\text{Xe}$  discharges. Although the heavier Xe ions are accelerated within the sheath region, the sheath thickness is not long enough for them to reach the energy carried by the fast-moving ions created by the  $\text{Cl}_2/\text{He}$  discharge. This partially explains the difference in etch rates between the different chemistries.

The effect of rf chuck power on the etch rates, dc bias, and ion flux at the sheath edge are shown in Figures 49 and 50. The etch rates of InN with  $\text{Cl}_2/\text{Xe}$  and  $\text{Cl}_2/\text{He}$  discharges increased up to 250 W and decreased at higher power (Figure 49, top), but increased monotonically with  $\text{Cl}_2/\text{Ar}$  as the rf power increased. The increase in etch rate can be attributed to enhanced sputter desorption of etch products as well as dominant physical sputtering of the InN surface. The decrease in InN etch rate with  $\text{Cl}_2/\text{He}$  and

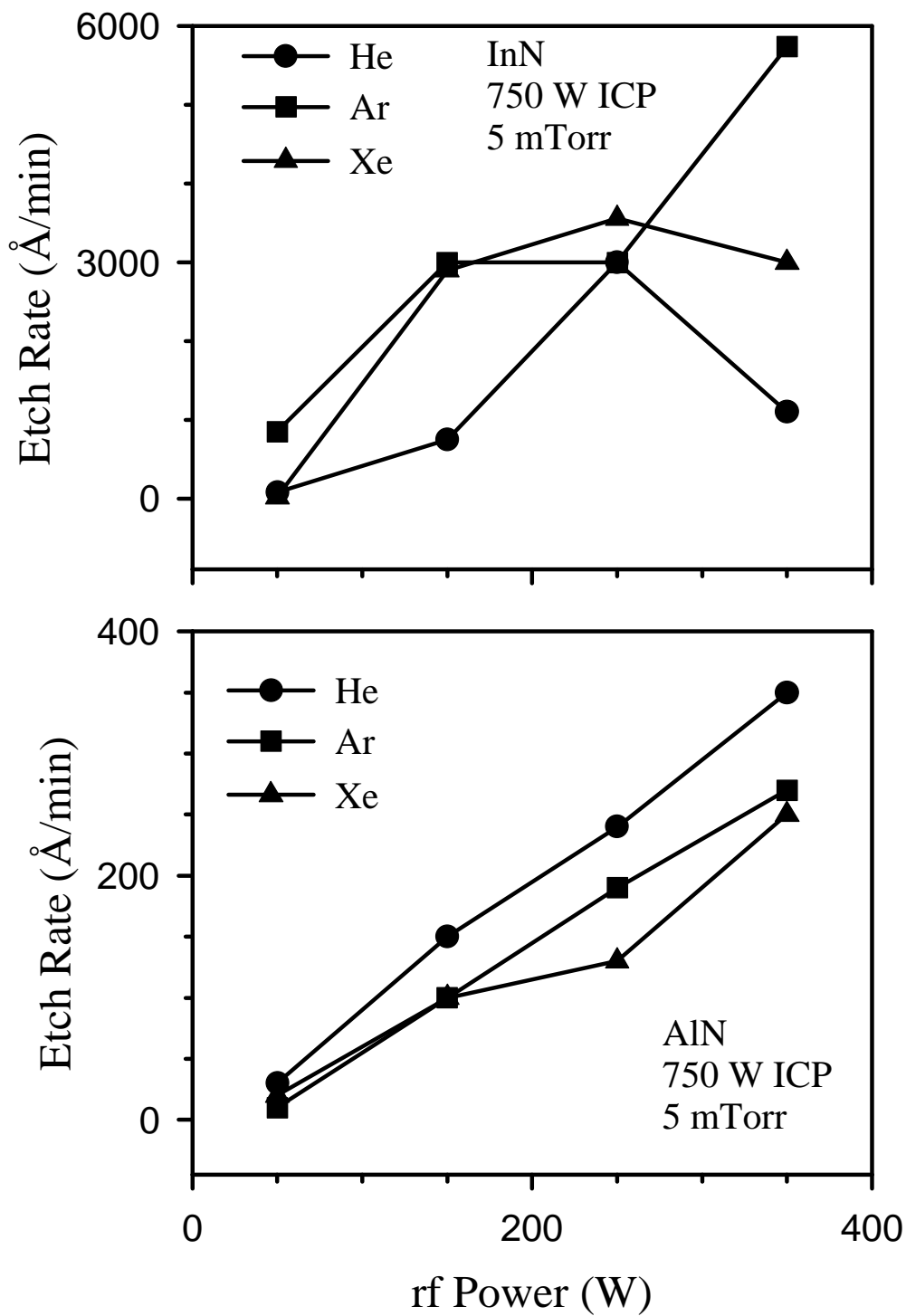


Figure 49. Effect of rf chuck power on etch rates of InN (top) and AlN (bottom) with  $2\text{Cl}_2/13\text{He}$ ,  $2\text{Cl}_2/13\text{Ar}$  and  $2\text{Cl}_2/13\text{Xe}$  plasma chemistries (750 W source power, 5 mTorr)

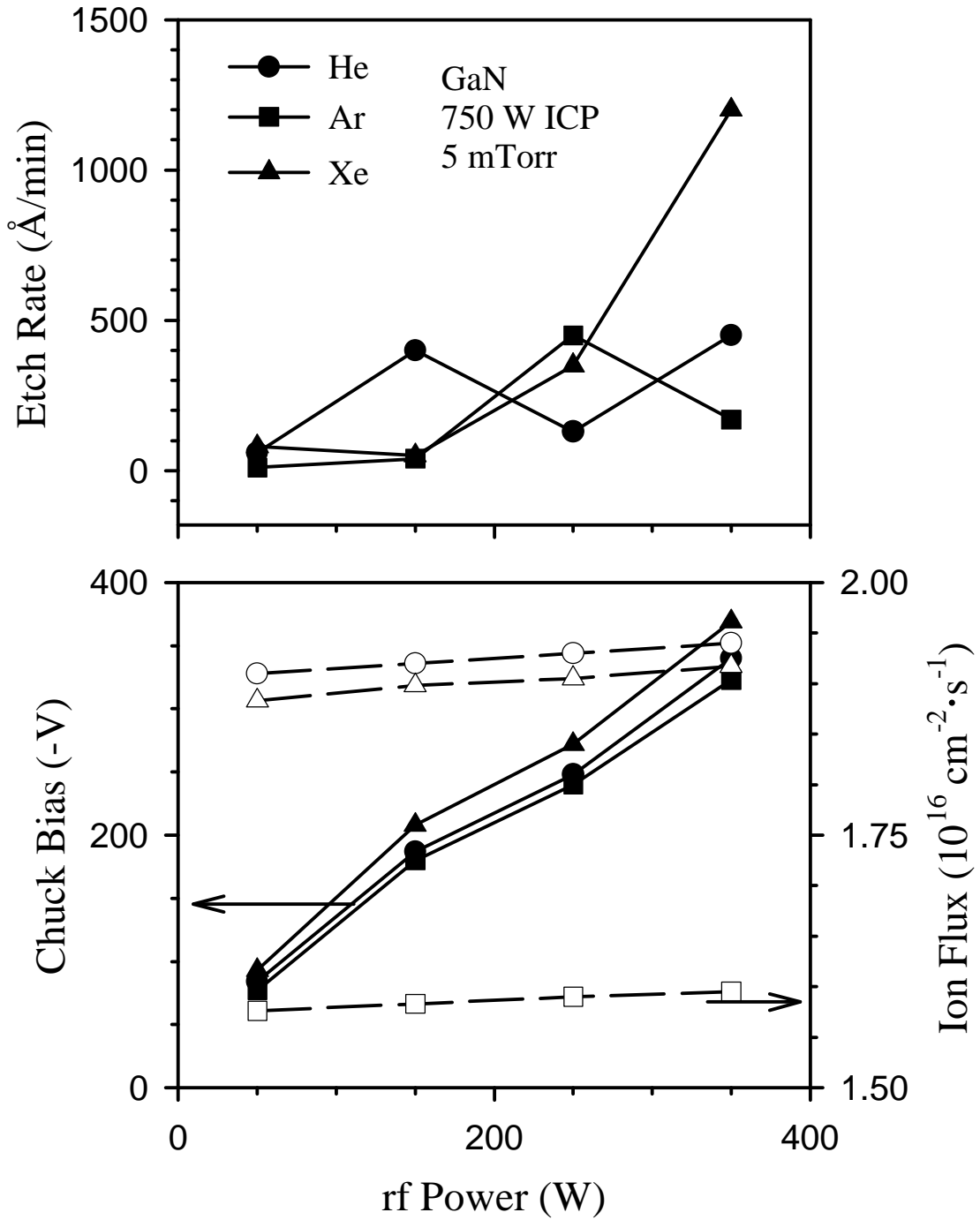


Figure 50. Effect of rf chuck power on etch rates of GaN (top) and on dc bias and ion flux at the sheath edge (bottom) with  $2\text{Cl}_2/13\text{He}$ ,  $2\text{Cl}_2/13\text{Ar}$  and  $2\text{Cl}_2/13\text{Xe}$  plasma chemistries (750 W source power, 5 mTorr)

$\text{Cl}_2/\text{Xe}$  at higher rf chuck power ( $> 300$  W) is believed to be due to the desorption of adspecies of reactive chlorine atoms from the substrate surface, caused by increased ion energy. It is also worthwhile to note that  $\text{Cl}_2/\text{He}$  and  $\text{Cl}_2/\text{Xe}$  plasmas have almost the same ion fluxes at the sheath edge, but are greater than the ion flux in  $\text{Cl}_2/\text{Ar}$  plasma. The etch rates of AlN increased monotonically as the rf power increased with all  $\text{Cl}_2$ -based discharges (Figure 49, bottom). However, GaN etching in  $\text{Cl}_2/\text{He}$  and  $\text{Cl}_2/\text{Ar}$  showed relatively constant etch rates with some fluctuations, and increased rapidly in the  $\text{Cl}_2/\text{Xe}$  chemistry as the rf power increased (Figure 50, top). Again, He and Xe additives resulted in overall better etch rates than Ar.

The monotonic increase in AlN etch is mainly due to the higher bond strength of AlN (11.52 eV) compared to InN and GaN, indicating that AlN etch rate is limited by breaking the Al-N bond. In order to initiate etching, breaking the group III-nitrogen bond is crucial, since this must precede the formation of etch products. Bond energies are in the order of InN (7.72 eV)  $<$  GaN (8.92 eV)  $<$  AlN (11.52 eV).<sup>(57)</sup> The etch rate is also related to the volatilities of the etch products. In chlorine-based plasmas, the boiling points are  $\text{AlCl}_3$  (183 °C)  $<$   $\text{GaCl}_3$  (201 °C)  $<$   $\text{InCl}_3$  (600 °C).<sup>(57)</sup> In addition to the experimental results, from the view points of bond strength and boiling point, two conclusions may be drawn: 1) the etch rates of InN are dominated by physical sputtering, due to the relatively low bond strength, but possibly limited by desorption of etch products due to the lowest volatility of  $\text{InCl}_3$  and 2) lower etch rates of GaN and AlN are limited by initial breaking of the III-nitrogen bond.

The dc bias increased monotonically with increasing rf chuck power from 50 to 350 W, but the ion flux at the sheath edge increased slightly (Figure 50, bottom). It is also

seen that the ion fluxes in  $\text{Cl}_2/\text{He}$  and  $\text{Cl}_2/\text{Xe}$  discharges are much greater than that in  $\text{Cl}_2/\text{Ar}$ , and  $\text{Cl}_2/\text{He}$  plasma shows somewhat greater ion flux than  $\text{Cl}_2/\text{Xe}$  discharge.

The effect of the rf power on ion fluxes at the sheath edge, respectively, generated by capacitive and inductive coupled discharges with chlorine-based chemistries was predicted using the self-consistent model and the results are shown in Figure 51. It is seen that the ion flux generated by the capacitive discharge increases substantially with increasing rf power, while that in the counterpart by the inductively coupled discharge maintains an essentially constant value. Hence the model predictions lead to a conclusion that the rf power increases not only the number of ion density but also the ion bombarding energy, resulting in an increase in etch rate with increasing the chuck power. However, the predicted ion flux (or bulk ion density) showed that the contribution of the capacitive discharge to total ion flux in the ICP etching process is less than 2 %, indicating that the main role of the chuck power is to increase the ion bombarding energy.

The effect of ICP source power on etch rate, dc bias, and ion flux at the sheath edge are shown in Figures 52 and 53. The influence of additive noble gases was dependent on III-nitride materials: the best etch rate for InN was obtained with  $\text{Cl}_2/\text{Xe}$  (Figure 52, top), while the overall highest rates for the other materials were achieved with  $\text{Cl}_2/\text{He}$ . InN showed higher etch rates again than AlN and GaN. The etch rates of InN with  $\text{Cl}_2/\text{He}$  and  $\text{Cl}_2/\text{Xe}$  discharges increased up to 750 W ICP power, and decreased at > 750 W (Figure 52, bottom). However, the  $\text{Cl}_2/\text{Ar}$  discharge showed the highest etch rate of InN at 1000 W. AlN etch rate increased slightly with the source power, but resulted in no good etch rates (Figure 52, bottom). GaN etch rates with  $\text{Cl}_2/\text{He}$  and  $\text{Cl}_2/\text{Ar}$  chemistries showed maxima as the source power increased, but relatively constant etch

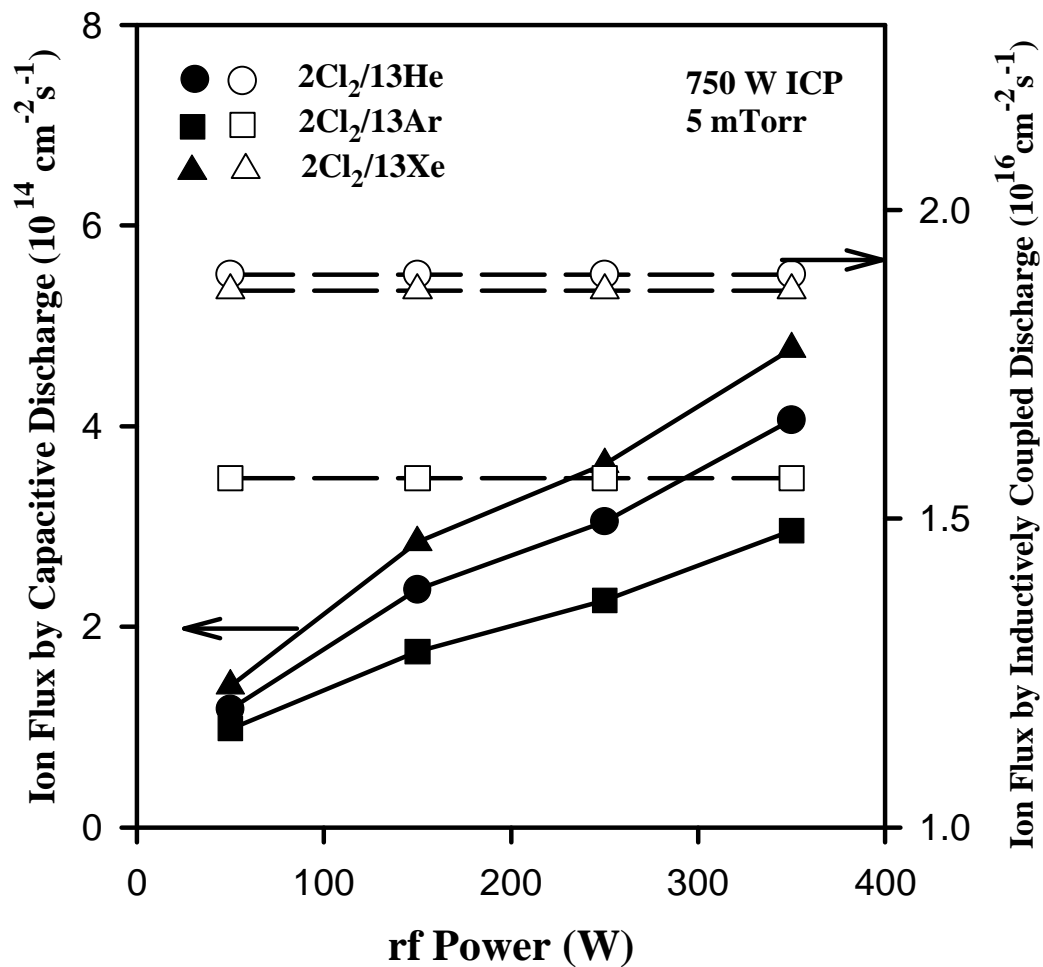


Figure 51. Effect of rf chuck power on the ion fluxes generated by capacitive discharge and inductively coupled discharge with 2Cl<sub>2</sub>/13He, 2Cl<sub>2</sub>/13Ar and 2Cl<sub>2</sub>/13 Xe plasma chemistries (750 W source power, 5 mTorr)

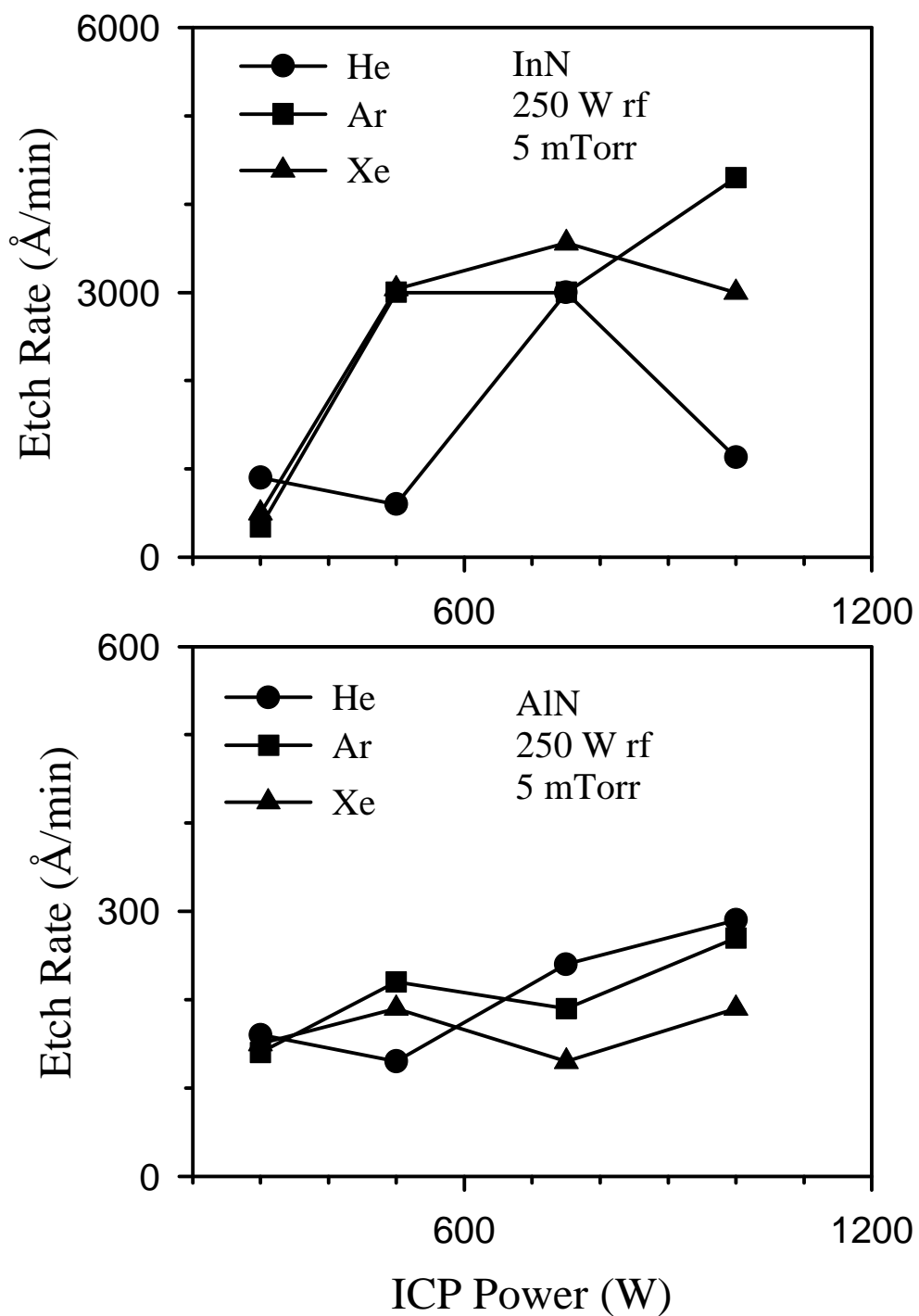


Figure 52. Effect of ICP source power on etch rates of InN (top) and AlN (bottom) with  $2\text{Cl}_2/13\text{He}$ ,  $2\text{Cl}_2/13\text{Ar}$  and  $2\text{Cl}_2/13\text{Xe}$  plasma chemistries (250 W rf chuck power, 5 mTorr)

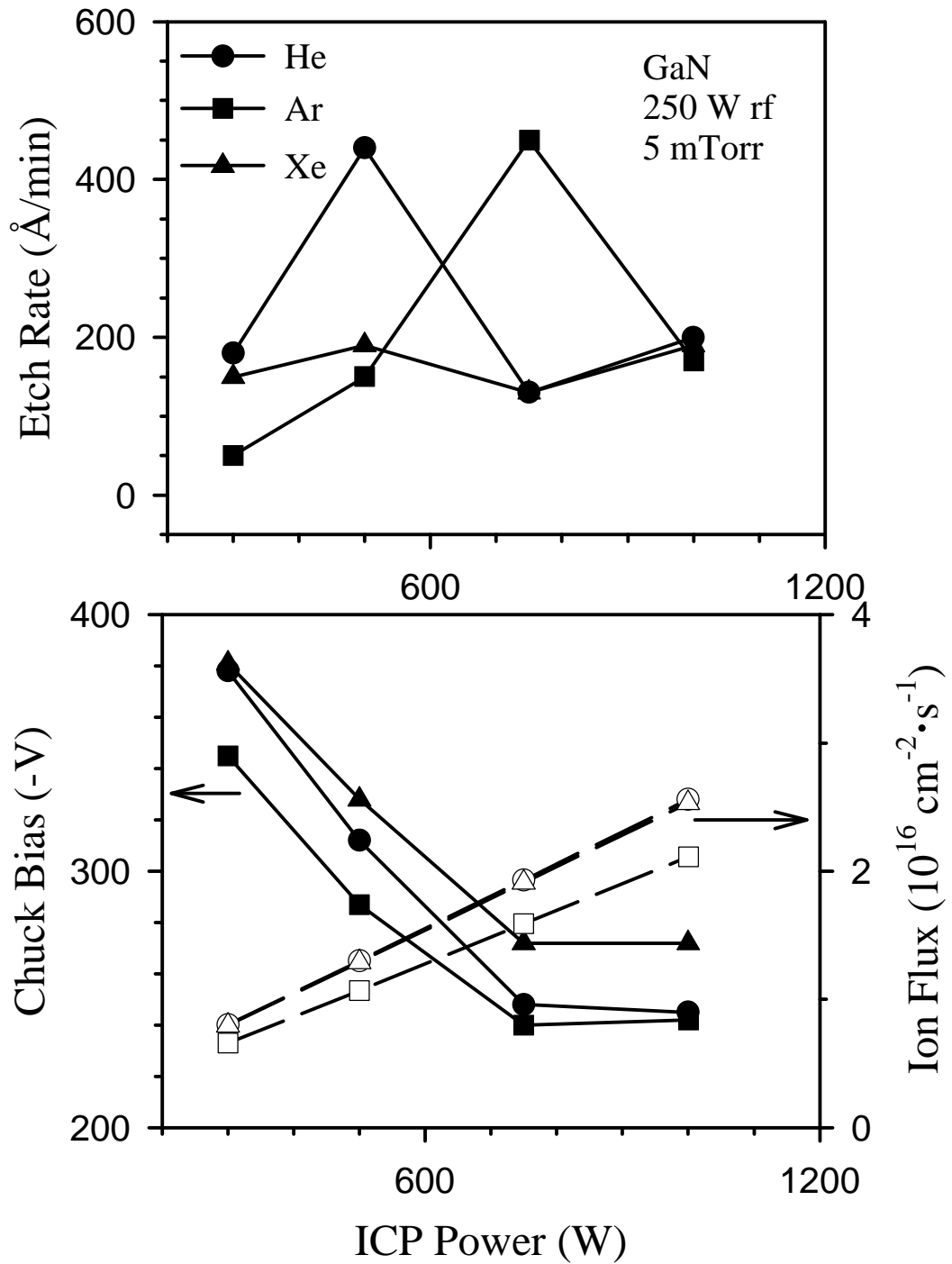


Figure 53. Effect of ICP source power on etch rates of GaN (top) and on dc bias and ion flux at the sheath edge (bottom) with  $2\text{Cl}_2/13\text{He}$ ,  $2\text{Cl}_2/13\text{Ar}$  and  $2\text{Cl}_2/13\text{Xe}$  plasma chemistries (250 W rf chuck power, 5 mTorr)

rates with  $\text{Cl}_2/\text{Xe}$  (Figure 53, top). The increase in etch rate with increasing source power is due to the higher concentration of reactive species in the plasma, suggesting a reactant-limited regime, and to higher ion flux to the substrate surface. Increased numbers of ions also make the surface more active with respect to the reactive neutrals. The decrease in etch rate with further increase of the ICP power is attributed either to lower ion energies or ion-assisted desorption of the reactive species at the substrate surface prior to etch reactions. The dc bias of the sample chuck was decreased as the ICP power increased mainly due to the increased ion density (Figure 53, bottom).

In order to reduce the currently high contact resistance in GaN-based heterostructure field transistors,<sup>(70)</sup> and eventually heterojunction bipolar transistors, it is expected that InN-based contact layers will be necessary,<sup>(71-73)</sup> in analogy to InGaAs on GaAs. In such a case, the ability to selectively etch InN relative to the other nitrides will be crucial. Figures 54 to 56 show some selectivity data as functions of chlorine concentration, rf power, and ICP power in chlorine-noble discharges, respectively. The effect of  $\text{Cl}_2$  concentration showed an overall trend of decrease in selectivities for InN over GaN and over AlN as chlorine percentage increases (Figure 54). It is also interesting to see that the  $\text{Cl}_2/\text{Xe}$  discharge gives the highest selectivity, and  $\text{Cl}_2/\text{He}$  and  $\text{Cl}_2/\text{Ar}$  plasmas show similar ones. As the rf power increased, the  $\text{Cl}_2/\text{Ar}$  discharge showed overall the best selectivity of InN over GaN (Figure 55, top), but the  $\text{Cl}_2/\text{He}$  chemistry yielded the lowest selectivities for InN over AlN as well as over GaN. It is clearly seen that the selectivities of InN over AlN in  $\text{Cl}_2/\text{He}$ ,  $\text{Cl}_2/\text{Ar}$  and  $\text{Cl}_2/\text{Xe}$  discharges increased as the source power increased up to 750 W, and decreased at

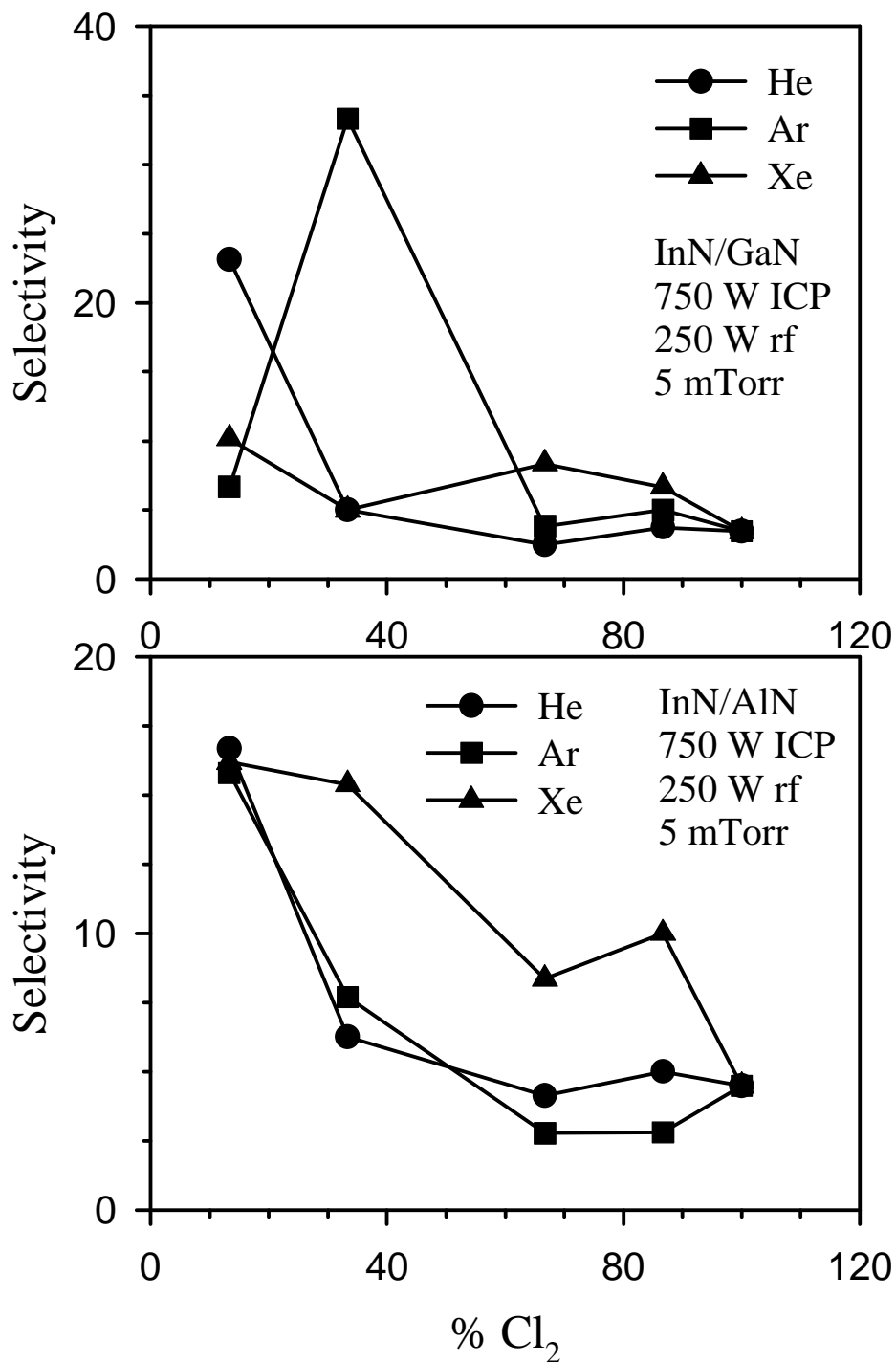


Figure 54. Effect of chlorine concentration on the selectivity for InN over GaN (top) and AlN (bottom) (750 W source power, 250 W rf chuck power, 5 mTorr)

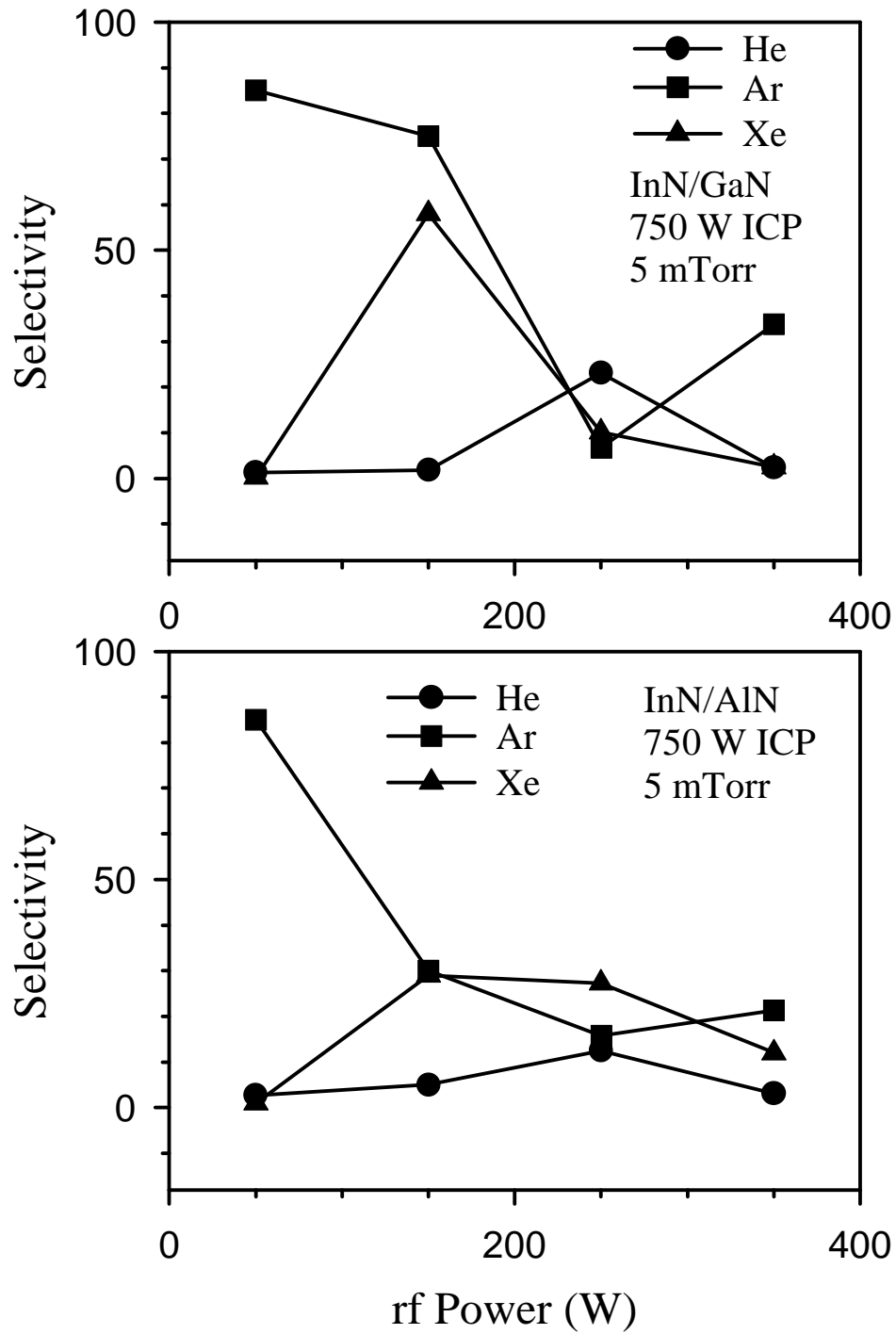


Figure 55. Effect of rf chuck power on the selectivity for InN over GaN (top) and AlN (bottom) (750 W source power, 5 mTorr, 2Cl<sub>2</sub>/13noble gas)

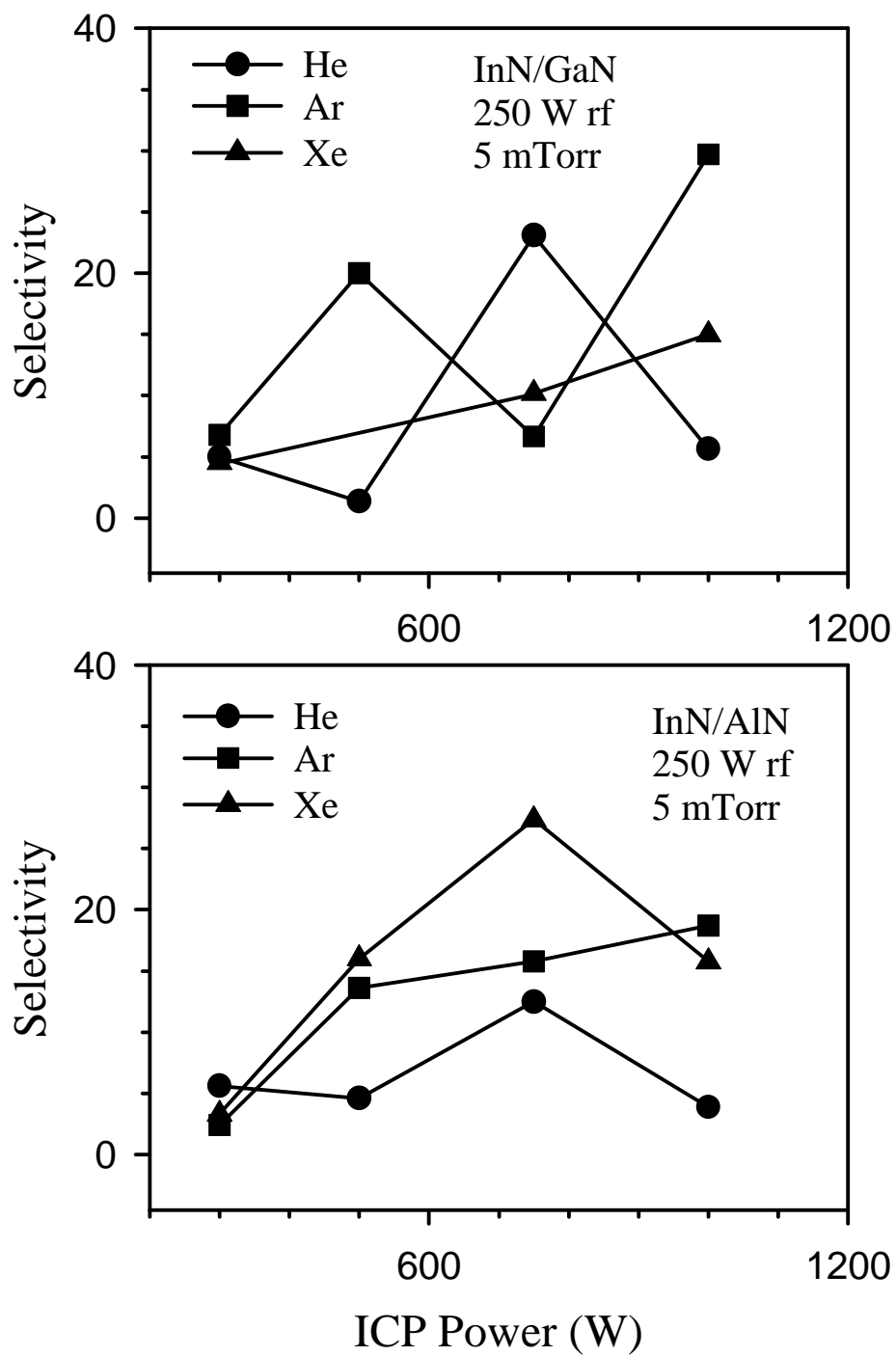


Figure 56. Effect of ICP source power on the selectivity for InN over GaN (top) and AlN (bottom) (250 W rf chuck power, 5 mTorr, 2Cl<sub>2</sub>/13noble gas)

> 750 W (Figure 56, bottom). The selectivity data obtained in this work showed overall higher selectivity characteristics for InN over GaN and AlN in Cl<sub>2</sub>/He, Cl<sub>2</sub>/Ar and Cl<sub>2</sub>/Xe than that previously reported.<sup>(74,75)</sup>

Figure 57 shows AFM scan results of the GaN surfaces etched with Cl<sub>2</sub>/He (top), Cl<sub>2</sub>/Ar (middle), and Cl<sub>2</sub>/Xe (bottom) chemistries at 750 W ICP power, 250 W rf chuck power and 5 mTorr. It is seen that the Cl<sub>2</sub>/Xe discharge shows the worst morphology, but all additives resulted in quite smooth surfaces that are fairly similar to unetched controls (rms roughness 0.8 - 1nm).

Figure 58 show the AES surface scans of GaN samples etched in Cl<sub>2</sub>/He (top), Cl<sub>2</sub>/Ar (middle), and Cl<sub>2</sub>/Xe (bottom) at 750 W ICP power, 250 W rf chuck power and 5 mTorr. The samples again show carbon and oxygen contamination due to exposure to air while being transferred from the ICP chamber to the AES chamber. The etched surfaces are chemically quite clean except for some slight chlorine contamination on the Cl<sub>2</sub>/Ar sample. Depth profiles showed that the surfaces remained stoichiometric, indicating equi-rate removal of both group III and V components.

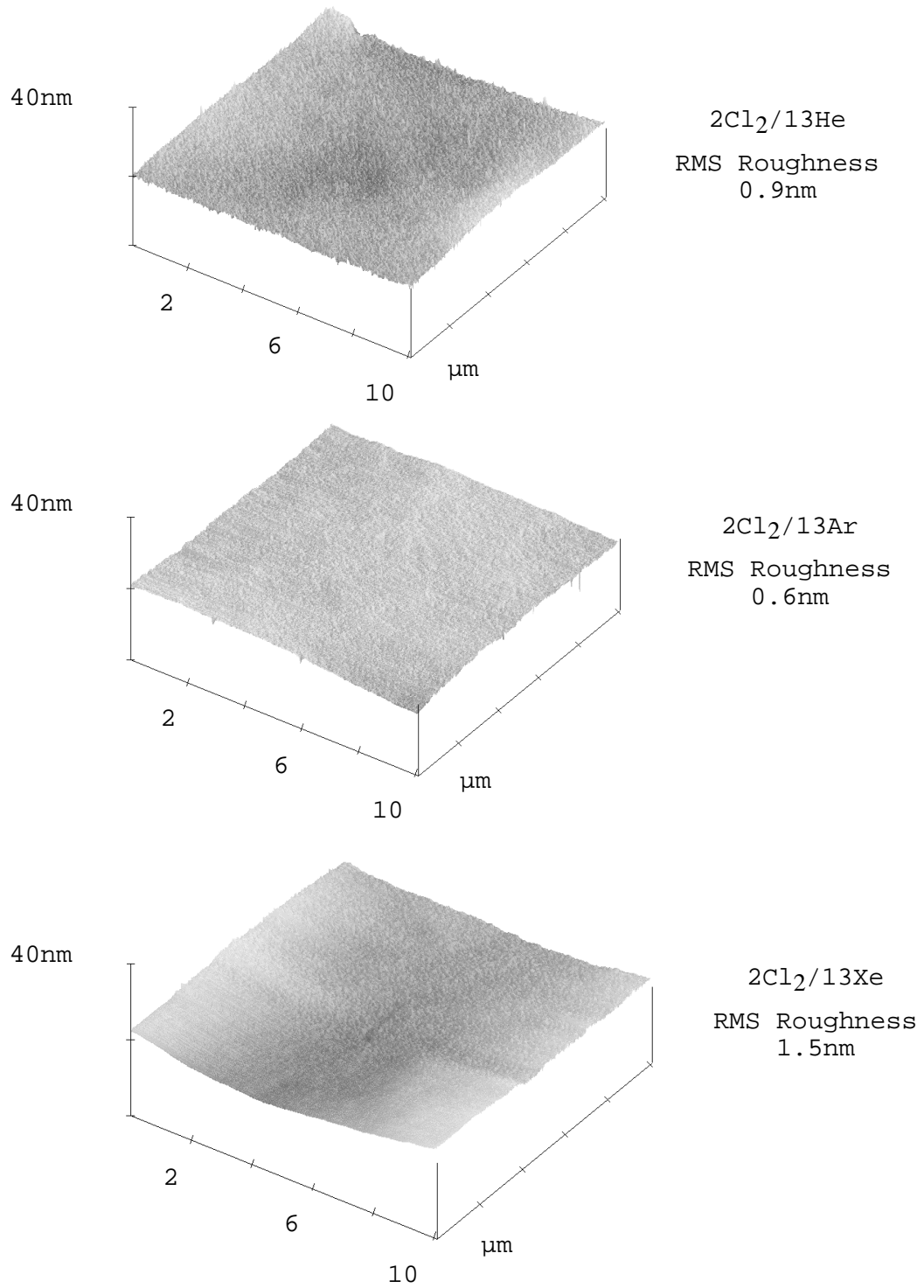


Figure 57. AFM scans of GaN etched with Cl<sub>2</sub>/He (top), Cl<sub>2</sub>/Ar (middle), and Cl<sub>2</sub>/Xe (bottom) at 750W source power, 250W rf chuck power, and 5mTorr

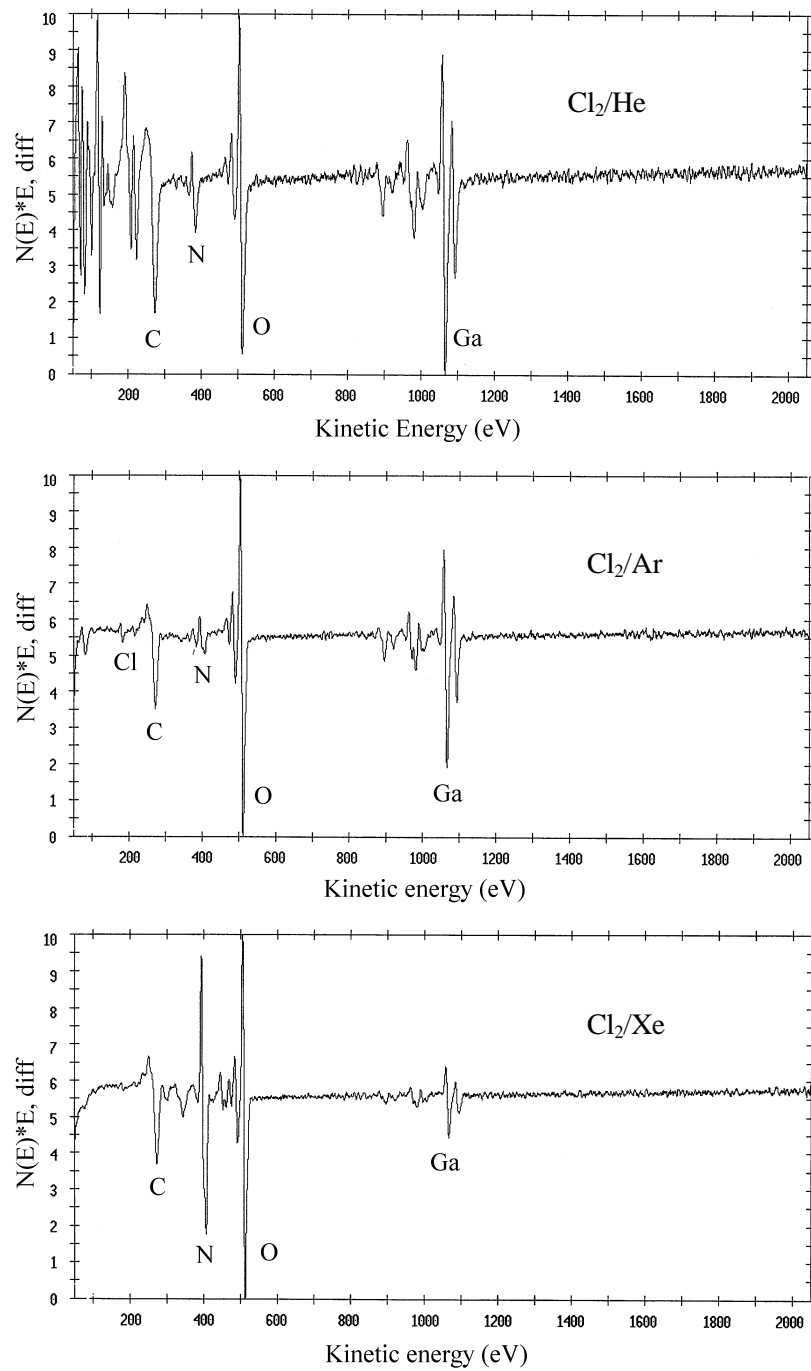


Figure 58. AES surface scans of GaN etched in Cl<sub>2</sub>/He (top), Cl<sub>2</sub>/Ar (middle), and Cl<sub>2</sub>/Xe (bottom) at 750W source power, 250W rf chuck power, and 5mTorr

## CHAPTER 6 HIGH RATE DRY ETCHING OF Si

### 6.1 Materials and Methods

The Si samples employed in these experiments were  $\frac{1}{4}$  of 4 inch diameter, (100), B-doped (10 cm) wafers. For etch rate determination a small section of each sample was masked with Apiezon wax, and the step height measured by stylus profilometry after the removal of the mask in acetone. Etching was performed in a Plasma Therm 790 series reactor. This consists of a 3-turn ICP source (2MHz, 1500W), a He backside-cooled, rf-biased (13.56MHz, 0-450W) sample chuck, and radial gas injection into the source through electronic mass flow controllers. In each case the gas load was left constant at 100 standard cubic centimeters per minute (sccm). Preliminary experiments showed the Si etch rates increased with pressure – for most of the work reported here the pressure was maintained at 35mTorr. This is the highest value at which plasma tuning was stable.

The etched surface morphology was examined by both Scanning Electron Microscopy (SEM) and Atomic Force Microscopy (AFM), while the near surface atomic composition was measured by Auger Electron Spectroscopy (AES). The dissociation of the feedstock gases in the ICP source was monitored by Optical Emission Spectroscopy (OES).

## 6.2 Results and Discussion

Figure 59 (top) shows the effect of ICP source power on Si etch rate for fixed process pressure (35mTorr) and without additional biasing of the sample chuck. In this case the ion energy is approximately equal to the plasma potential (roughly  $-25\text{eV}$  in this tool at these conditions as determined by Langmuir probe measurements). Since real micro-machining processes involve long exposures of the mask material to the plasma, it is necessary to minimize the ion energy to prevent erosion of the mask. There are significant differences in the Si etch rates achieved with the four different plasma chemistries, with  $\text{SF}_6$  providing for the fastest etch rates. It is instructive to compare the observed etch rate trends with the average bond energies for the gases, shown in Table 3. Note that there is a good correlation between weaker bond energy (i.e. easier dissociation to provide reactive fluorine neutrals) and higher etch rate, except for the case of  $\text{NF}_3$ . This gas should provide the highest etch rate, based on the assumption of a simple gas dissociation analysis of the process. The etch yields (defined as the number of Si atoms removed per incident ion) were calculated from a simple semi-empirical model that uses extrapolations of ion flux data obtained from Langmuir probe measurements. In  $\text{SF}_6$  and  $\text{PF}_5$  there is clearly a strong chemical component to the etching, with etch yields in the range 6-10.

The same experiments were repeated with 5W rf chuck bias, which corresponds to dc self-biases of  $-15$  to  $-30\text{V}$ . The average energy of incident ions is then the sum of this bias and the plasma potential mentioned earlier. The same basic trends in etch rate with ICP power were observed (Figure 60, top), and consequently in the etch yields (Figure 60, bottom).

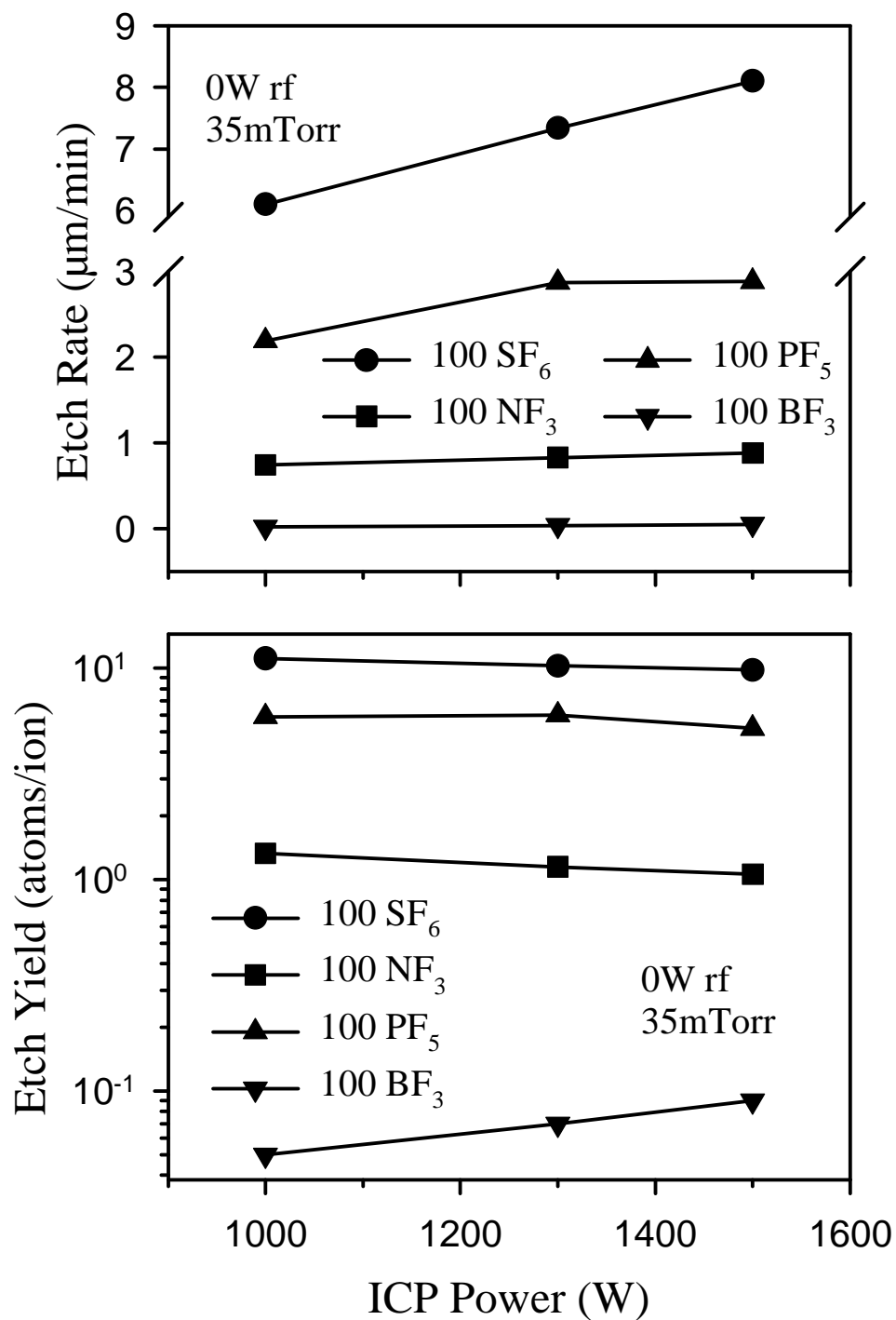


Figure 59. Si etch rate (top) and etch yield (bottom) as a function of ICP source power in pure  $\text{SF}_6$ ,  $\text{NF}_3$ ,  $\text{PF}_5$ , or  $\text{BF}_3$  discharges (35mTorr, 0W rf chuck power)

Table 3. Average bond energies for feedstock gases

<b>Gas</b>	<b>Avg. Bond Energy (kcal/mol)</b>	<b>Reference</b>
BF <sub>3</sub>	154	76
PF <sub>5</sub>	126	77
SF <sub>6</sub>	78.3	78
NF <sub>3</sub>	66.4	79

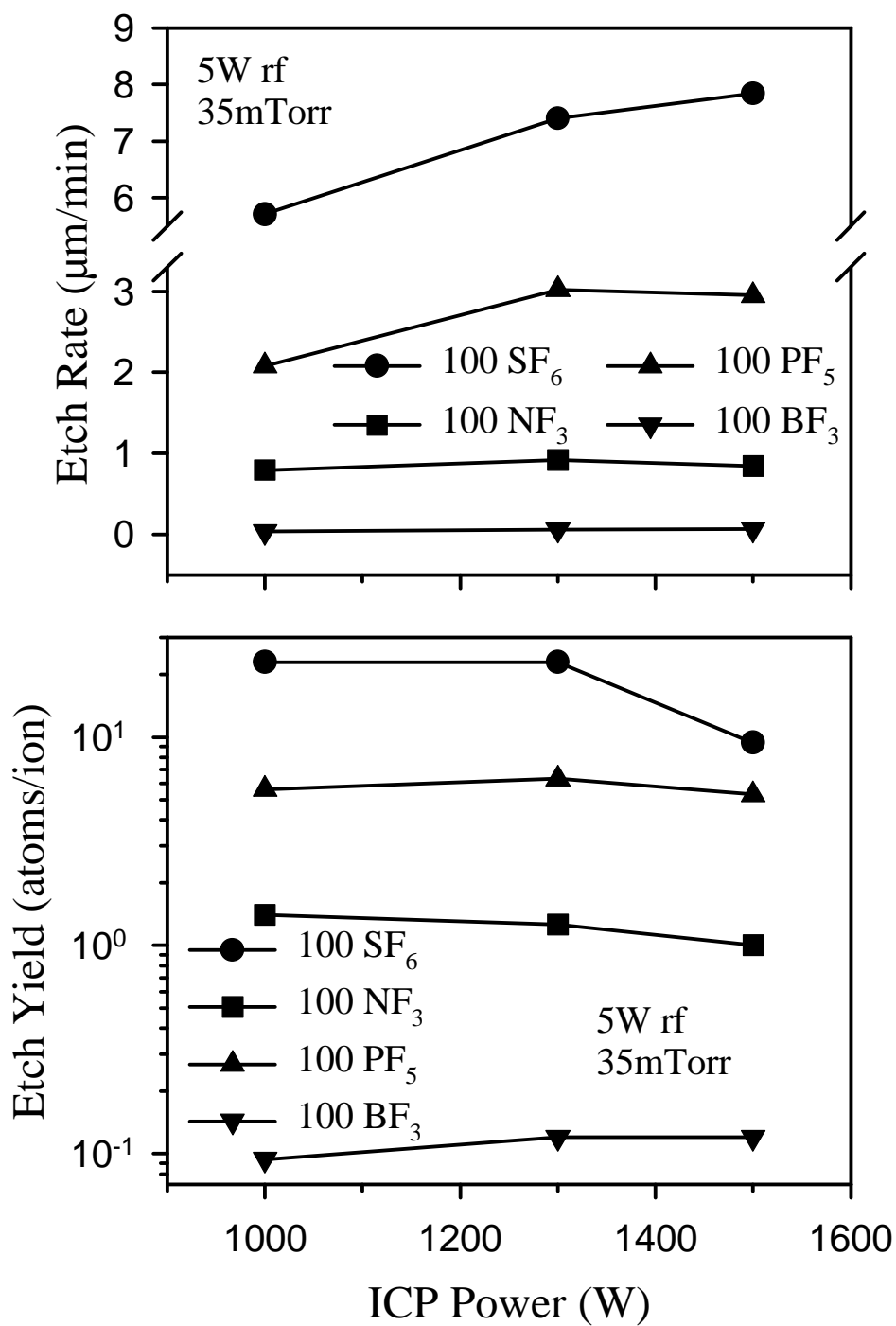


Figure 60. Si etch rate (top) and etch yield (bottom) as a function of ICP source power in pure  $\text{SF}_6$ ,  $\text{NF}_3$ ,  $\text{PF}_5$ , or  $\text{BF}_3$  discharges (35mTorr, 5W rf chuck power)

OES was used to examine emission from the various discharges during etching of Si. Figure 61 shows the spectra from  $\text{BF}_3$  and  $\text{PF}_5$  processes. In both cases there are clear signatures of the atomic fluorine lines between 680-800nm, and  $\text{SiF}_x$  etch products (around 450nm). The surprising result is shown in the OES spectra for  $\text{SF}_6$  and  $\text{NF}_3$  in Figure 62. The  $\text{SF}_6$  also produces strong emission from atomic fluorine and the  $\text{SiF}_x$  etch products, while the  $\text{NF}_3$  spectrum has the strongest  $\text{F}^0$  emission intensity of all the gases, as expected from its average bond energy. However, consistent with the etch rate data, we observed only a tiny peak due to the  $\text{SiF}_x$  etch products.

SEM micrographs of the Si surfaces after 2 min etches in the four different plasma chemistries are shown in Figure 63. The surfaces after  $\text{PF}_5$  or  $\text{BF}_3$  etching are featureless at this magnification (x1000), while the  $\text{SF}_6$ -etched surface shows the presence of small pits. We should point out that the human eye does not detect any morphology on this surface and it appears mirror-like. We assume that the high chemical component involved in the  $\text{SF}_6$  etching leads to delineation of crystal defects, which etch slightly faster than perfect Si. Note that this is the surface morphology after etching  $\sim 16\mu\text{m}$  with the  $\text{SF}_6$  discharge. By sharp contrast, the  $\text{NF}_3$ -etched surfaces appear cloudy to the eye, and the SEM reveals the presence of shallow pits and linear defects. This is the surface morphology after etching  $\sim 1.5\mu\text{m}$  with the  $\text{NF}_3$  discharge.

A more quantitative measure of surface is obtained from the AFM data. Figure 64 shows the Si surfaces before and after etching in the four different plasma chemistries. While the  $\text{PF}_5$  and  $\text{BF}_3$  produce little change in root-mean-square (RMS) roughness of the Si surface, there is significant roughening with the other two chemistries. As seen in the microstructure, this is due to the delineation of shallow pits in the case of  $\text{SF}_6$ , whereas

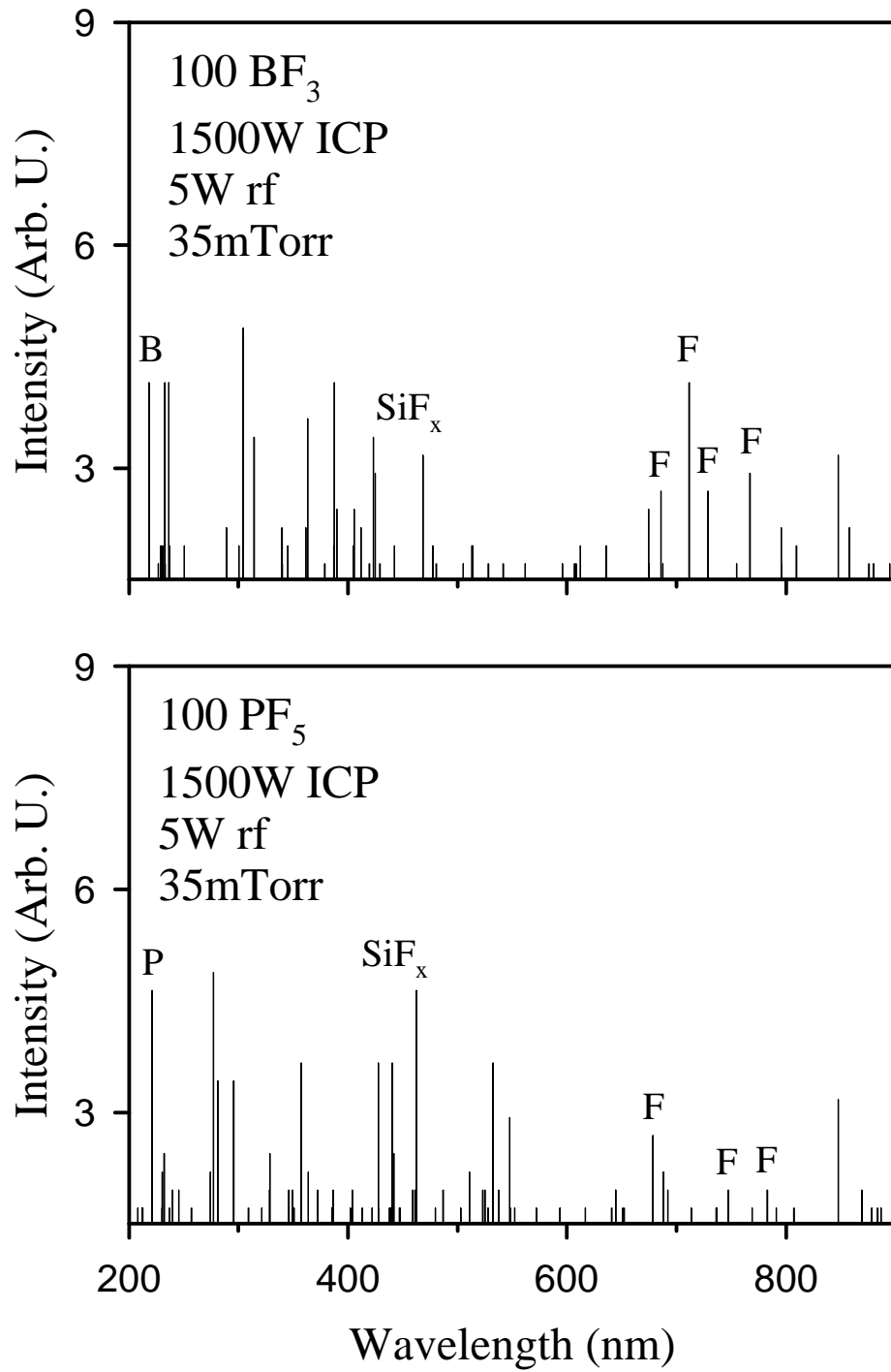


Figure 61. OES spectra from  $\text{BF}_3$  (top) and  $\text{PF}_5$  (bottom) discharges during etching of Si

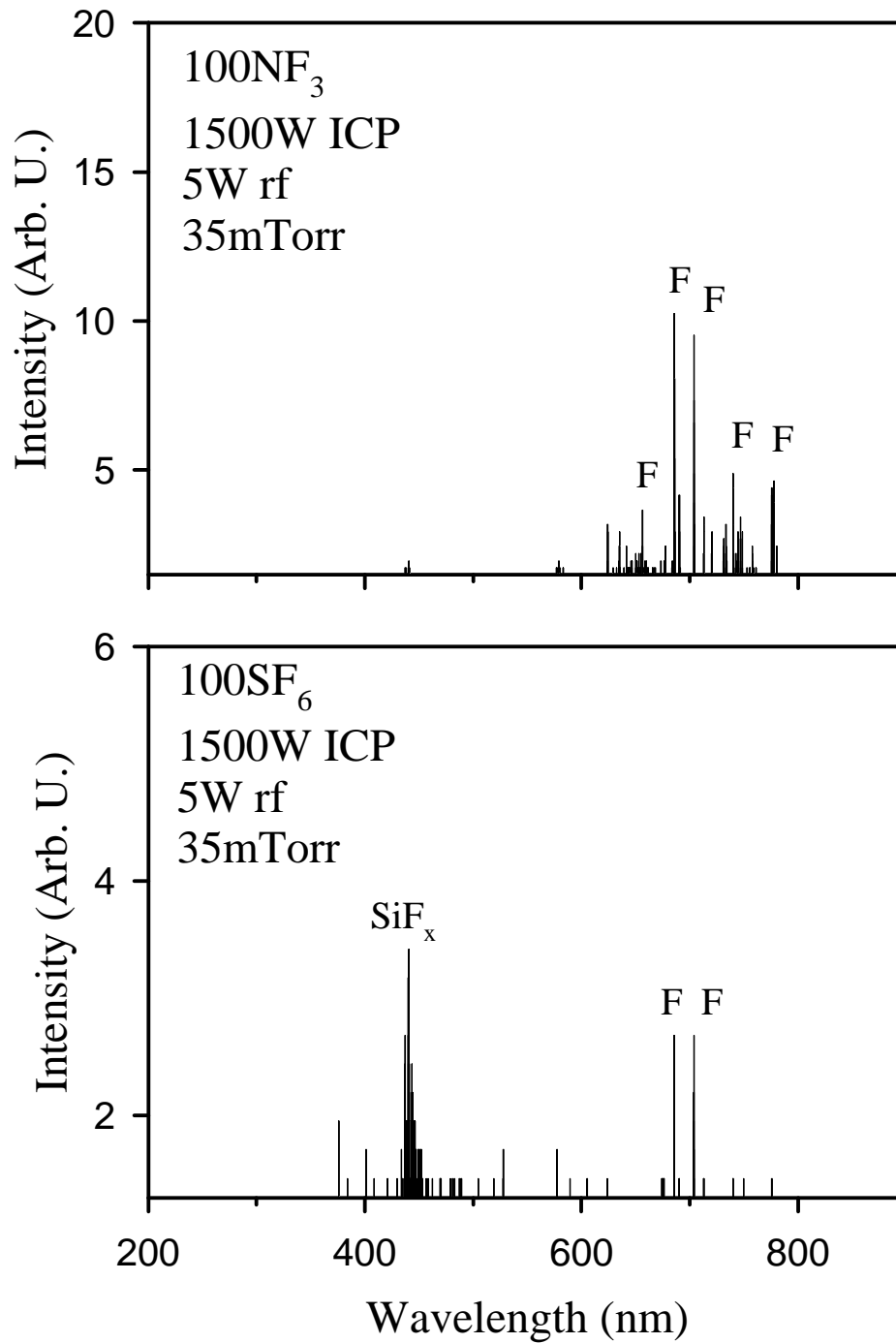


Figure 62. OES spectra from  $\text{NF}_3$  (top) and  $\text{SF}_6$  (bottom) discharges during etching of Si

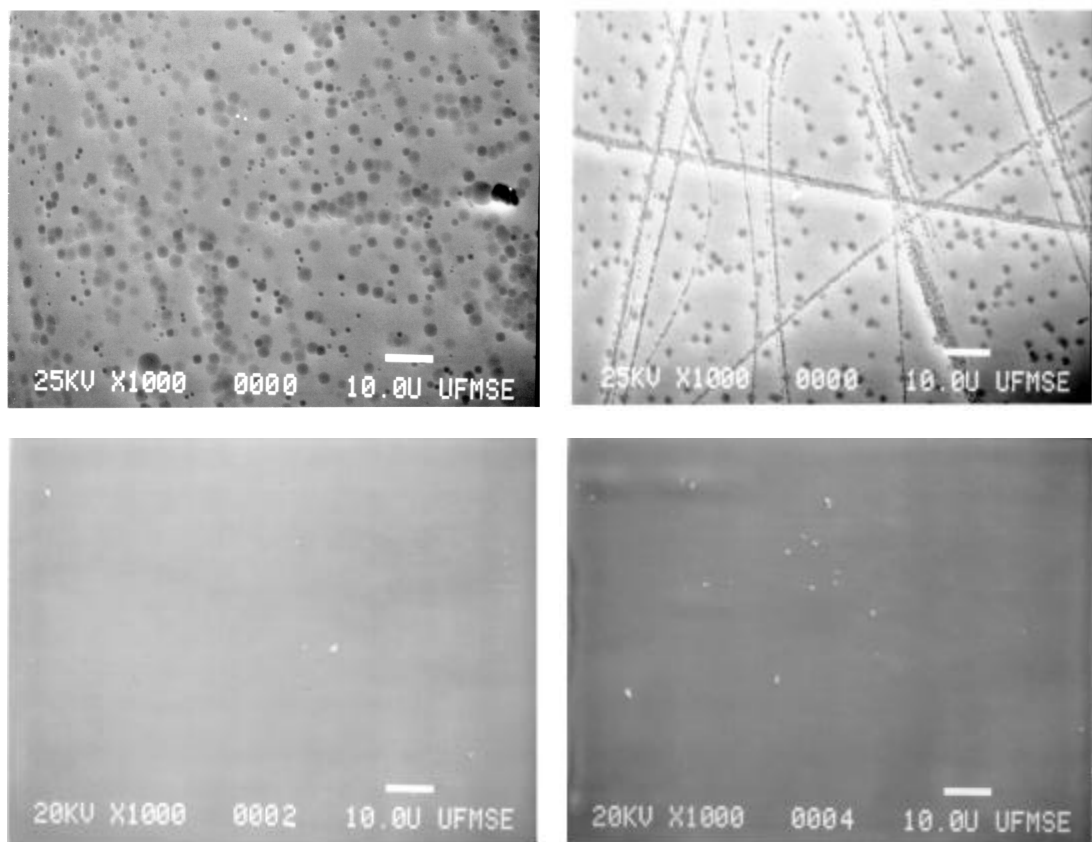
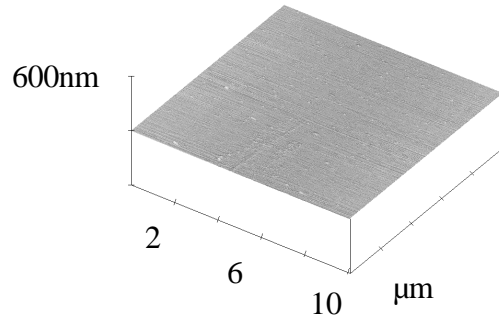
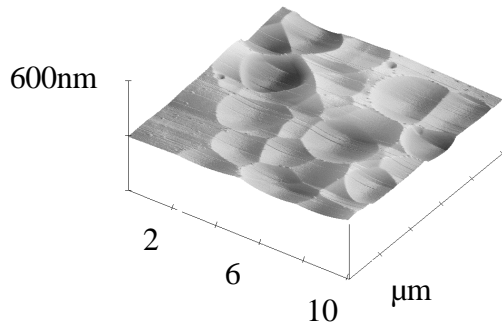


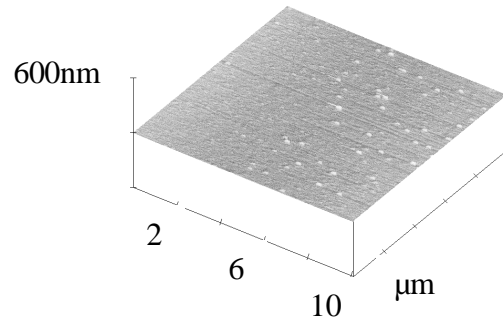
Figure 63. SEM micrographs of Si surfaces after etching in SF<sub>6</sub> (top left), NF<sub>3</sub> (top right), PF<sub>5</sub> (bottom left), and BF<sub>3</sub> (bottom right)



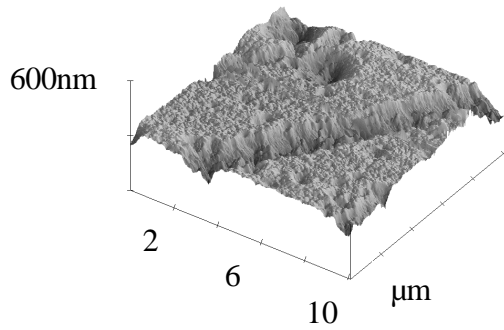
Silicon Control  
RMS Roughness = 1.1nm



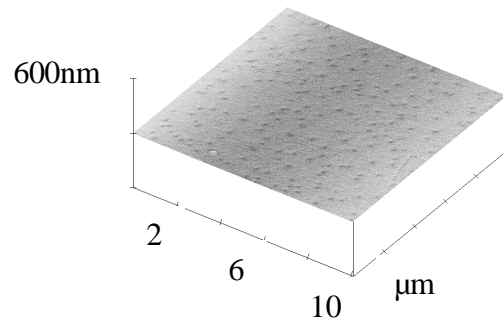
100SF<sub>6</sub>, 1500W ICP, 0W rf, 35mTorr, 2min.  
RMS Roughness = 23.2nm



100PF<sub>5</sub>, 1500W ICP, 0W rf, 35mTorr, 2min.  
RMS Roughness = 1.4nm



100NF<sub>3</sub>, 1500W ICP, 0W rf, 35mTorr, 2min.  
RMS Roughness = 67.1nm



100BF<sub>3</sub>, 1500W ICP, 0W rf, 35mTorr, 2min.  
RMS Roughness = 1.2nm

Figure 64. AFM scans of Si surfaces before and after etching  
in SF<sub>6</sub>, NF<sub>3</sub>, PF<sub>5</sub>, and BF<sub>3</sub>

AFM data for the  $\text{NF}_3$  surface is clearly much rougher on a micro-scale. The RMS values for the etched surfaces are shown in Figure 65 as a function of ICP source power for the four plasma chemistries. Note that the roughness of surfaces etched in  $\text{SF}_6$  increases much more rapidly with source power than does etch rate (compare with Figure 59). This indicates that the etch pits become more obvious above a certain source power, i.e. above certain  $F^0$  densities.

The surprising result in all of these experiments is that  $\text{NF}_3$  does not produce the fastest etch rates. One cause might be the formation of a heavily fluorinated (or nitrated) surface layer that prevents reaction of adsorbed fluorine neutrals to form the volatile etch products. We examined the etched surfaces with AES, and surface scans of the  $\text{SF}_6$  and  $\text{NF}_3$  processed samples are shown in Figure 66. In both cases they look similar to the etched control sample. However, we did notice a small F-residue signal present on the  $\text{NF}_3$ -etched sample during the first few passes of the scan. These residues were desorbed by the electron probe beam during the analysis, but do not appear in the scan of Figure 66 because that represents the average of 10 consecutive passes of the beam (a standard method when presenting AES data). Note that we did not observe any N-related residues on the  $\text{NF}_3$ -etched surfaces.

If indeed some type of selvedge layer is the cause of the lower-than-expected Si etch rates in  $\text{NF}_3$  discharges, we might expect that a reduction in the  $F^0$  neutral flux might actually enhance the etch rate. The neutral flux can be altered by changing either the process pressure or ICP source power, while an increase in dc self-bias would provide more efficient sputter-desorption of adsorbed reactants and etch products. Figure 67

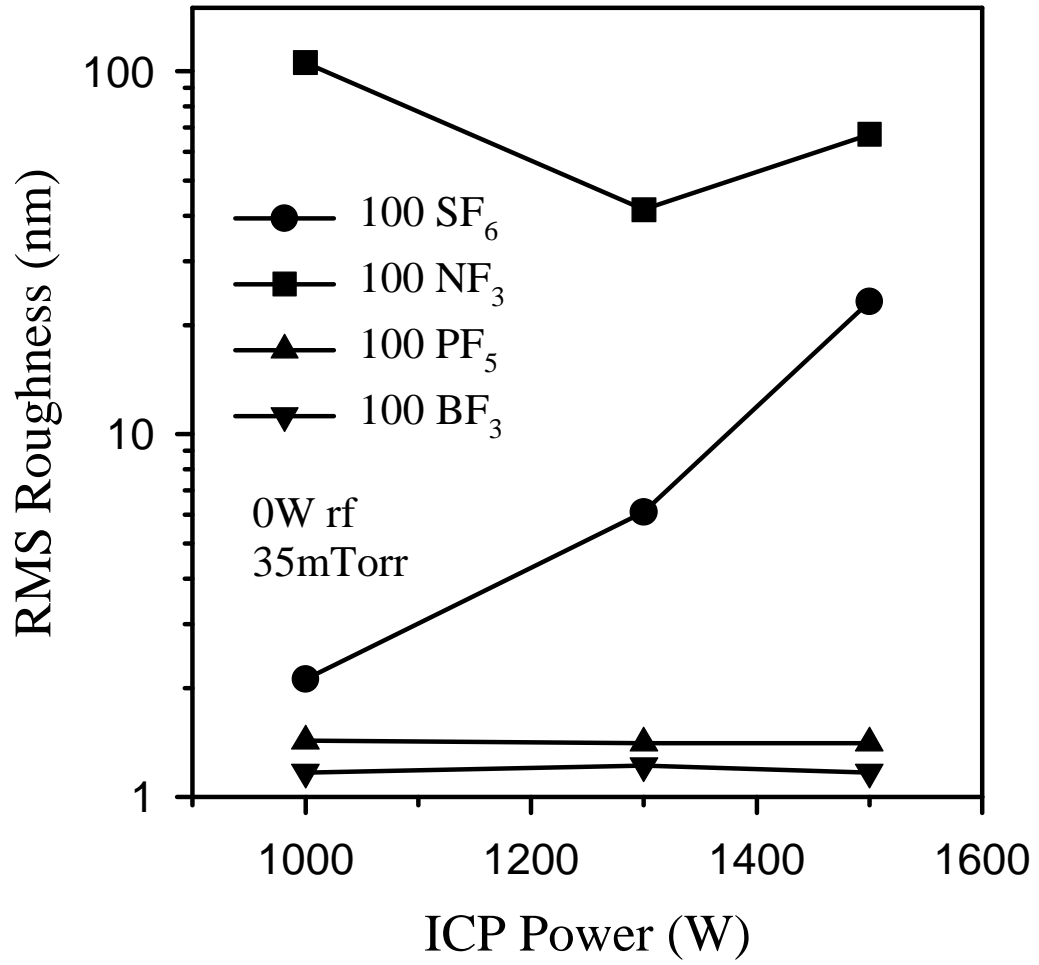


Figure 65. RMS roughness of Si surfaces after etching in SF<sub>6</sub>, NF<sub>3</sub>, PF<sub>5</sub>, and BF<sub>3</sub>

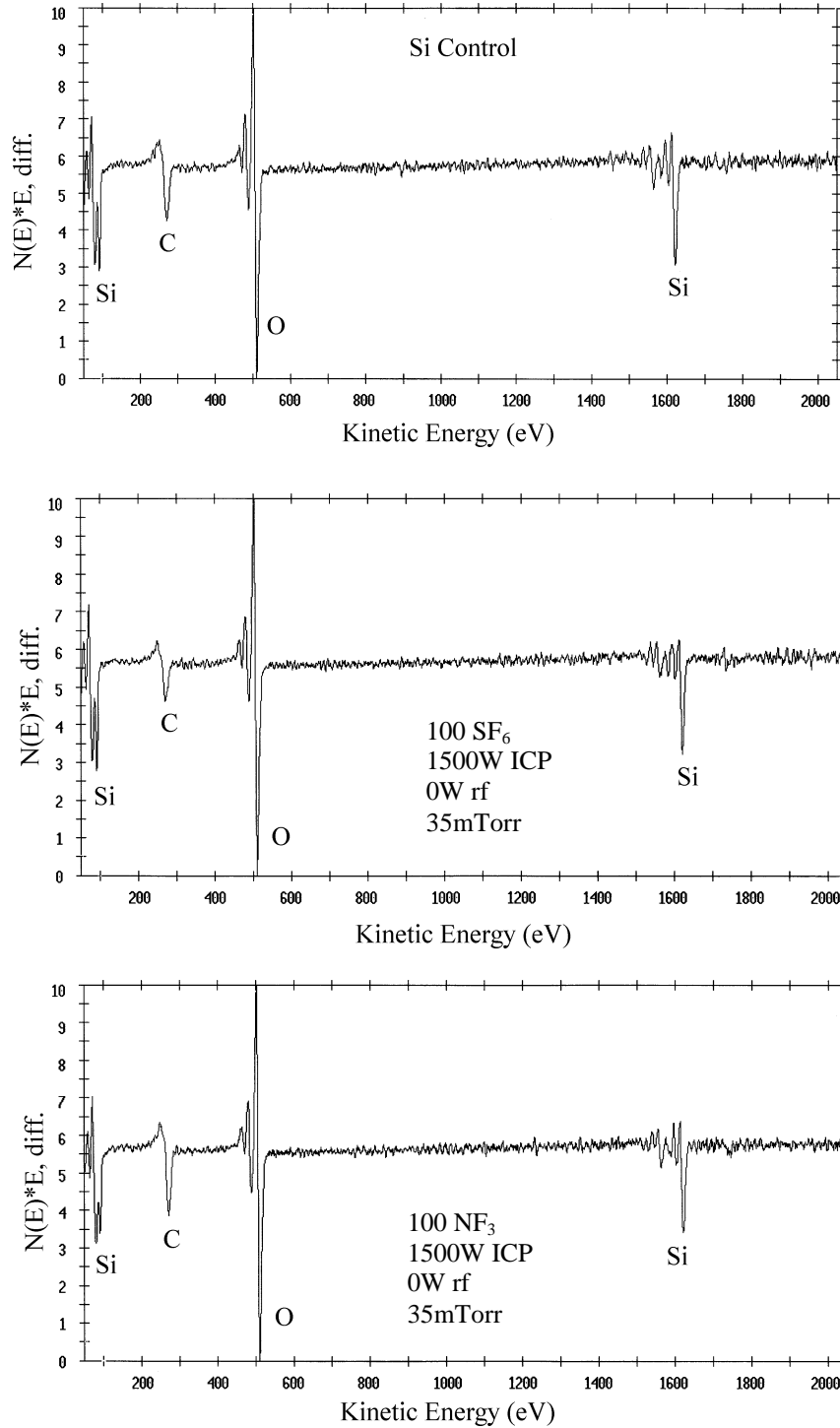


Figure 66. AES surface scans of Si before (top) and after SF<sub>6</sub> (center) or NF<sub>3</sub> (bottom) etching

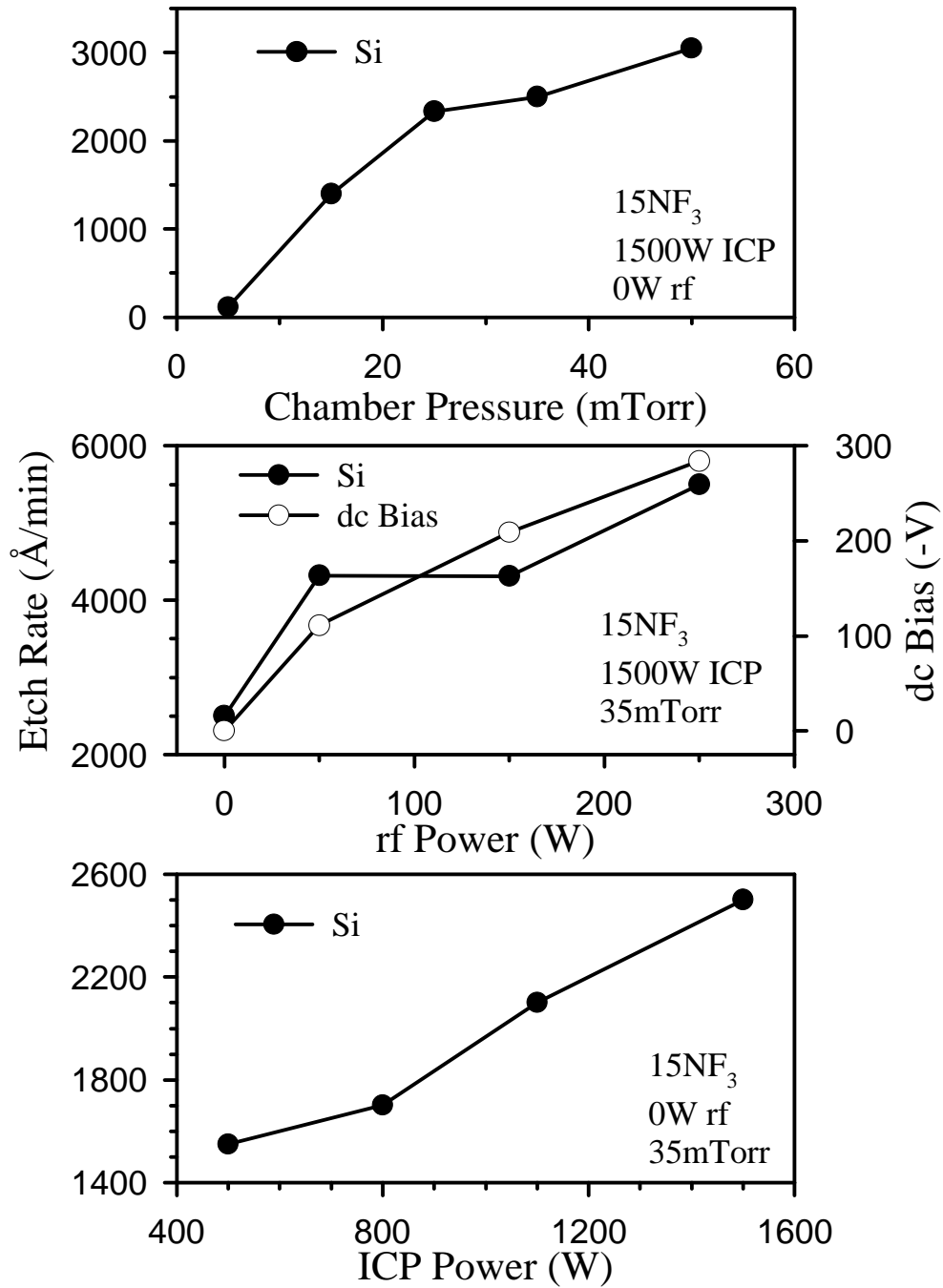
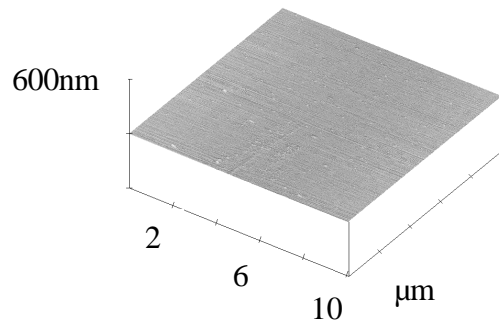
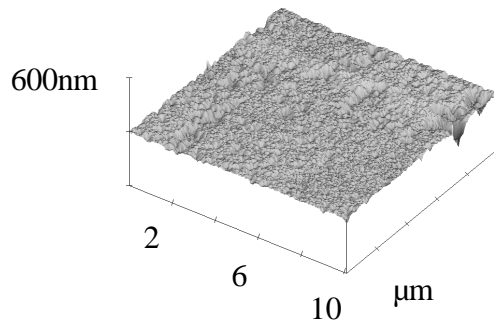


Figure 67. Si etch rate as a function of Pressure (top), rf power (middle), and ICP power (bottom) in  $\text{NF}_3$  discharges

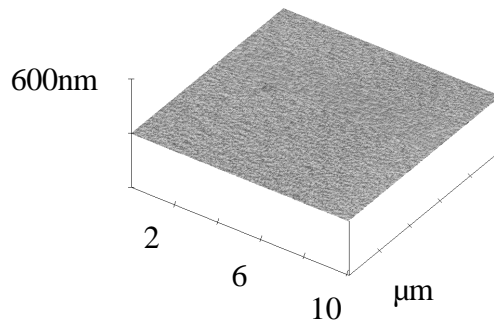
shows the Si etch rate in  $\text{NF}_3$  discharges as a function of each of these parameters. Note that under no set of conditions do we achieve etch rates approaching those obtained with  $\text{SF}_6$  (or  $\text{PF}_5$ ). One clear effect of increasing ion energy through higher rf chuck power was a transition from rough morphology to smooth surfaces on  $\text{NF}_3$ -etched samples, as shown in the AFM data of Figure 68. This would be expected through an enhanced physical contribution to the etch mechanism, with the angular dependence of ion milling producing faster etching of sharp surface features.



Silicon control  
RMS Roughness = 1.1nm



15NF<sub>3</sub>, 1500W ICP, 0W rf, 35mTorr, 2min.  
RMS Roughness = 24.3nm



15NF<sub>3</sub>, 1500W ICP, 250W rf, 35mTorr, 2min.  
RMS Roughness = 1.3nm

Figure 68. AFM scans of Si surfaces before (top) and after (center and bottom) NF<sub>3</sub> etching without (center) or with (bottom) rf biasing of the chuck position

## CHAPTER 7 SUMMARY

The etching characteristics of GaAs and AlGaAs were studied in citric acid/hydrogen peroxide etching solutions over a wide range of compositions. Selectivity of GaAs over AlGaAs reaches a peak of 71 using a 2citric acid:1H<sub>2</sub>O<sub>2</sub> solution at 21°C. For the GaAs-based system, careful measurement of the citric acid/H<sub>2</sub>O<sub>2</sub> ratio is necessary in providing the correct etch rate and selectivity, as a slight change in volume ratio can result in a large change in etching characteristics (compare volume ratios 2.0 and 3.0 for GaAs). For ratios beyond 6:1, both GaAs and AlGaAs have about the same etch rate, providing a uniform (nonselective) etchant. At low ratios of citric acid:H<sub>2</sub>O<sub>2</sub>, the AlGaAs appears to be diffusion limited but makes a transition to reaction limited for high volume ratios. The GaAs was reaction rate limited for all volume ratios. In summary, selective wet etching using citric acid/H<sub>2</sub>O<sub>2</sub> solutions provides a reasonably simple, safe and reliable process for GaAs/AlGaAs heterostructure device fabrication.

While ICP reactors produce much higher etch rates than capacitively-coupled tools, as expected, etch selectivity for the GaAs/AlGaAs and GaAs/InGaP systems is generally lower under ICP conditions relative to conventional RIE because of the more efficient sputter-assisted desorption of the etch products that produce the etch-stop reactions, i.e. AlF<sub>3</sub>, InF<sub>3</sub>, and InCl<sub>3</sub>. BCl<sub>3</sub>/SF<sub>6</sub> is a superior choice to BCl<sub>3</sub>/NF<sub>3</sub> in terms of achieving higher selectivities in both semiconductor systems. ICl, IBr, and BBr<sub>3</sub> produce essentially non-selective etching of GaAs/AlGaAs and GaAs/InGaP. BI<sub>3</sub> produces good

selectivity ( $\sim 60$ ) for InGaP/GaAs obviating the need for  $\text{CH}_4/\text{H}_2$  based chemistries for this application. An obvious strategy to improve selectivity is simply to shut off the source power toward the end of the etch process and remove the last few hundred angstroms of material using RIE conditions.

In contrast to the GaAs/AlGaAs and GaAs/InGaP systems, the maximum selectivities for InN/GaN and InN/AlN are obtained in moderate source and rf chuck powers and moderate pressures, rather than low power and high pressures. These differences reflect the need to have fairly high ion fluxes in order to achieve practical etch rates for the nitrides. The results for ICl and IBr are superior to those achieved with the  $\text{Cl}_2$  based chemistries. The selectivities of InN over GaN are greater than those of InN over AlN in both ICl/Ar and IBr/Ar discharges, with the lone exception of high IBr concentrations. For the  $\text{Cl}_2$  based discharges, the influence of the additive gases was highly dependent on the particular III-nitride material. In general, argon produced higher selectivities than helium or xenon as an additive. The InN etching was dominated by physical sputtering while the GaN and AlN etching was limited by initial breaking of the III-nitrogen bond.

Four different  $\text{F}_2$ -based plasma chemistries have been compared for the goal of achieving high etch rates for Si. The fastest Si etch rate was obtained in  $\text{SF}_6$ , with peak rates of  $\sim 8\mu\text{m}/\text{min}$ . The simple picture of the Si etch rate being limited by the supply of reactive fluorine neutrals would favor the choice of  $\text{NF}_3$ , since it is the least strongly bound. However, experimentally it is observed that  $\text{NF}_3$  discharges produce relatively slow Si etch rates, even though the gas is efficiently dissociated in the ICP source. The cause of these low rates is not clear. We have previously observed that SiC is etched

more rapidly in  $\text{NF}_3$  than in  $\text{SF}_6$  discharges. It will probably be necessary to employ some form of in-situ analysis of the  $\text{NF}_3$ -etched surfaces in order to firmly establish the reason why the etch rates are not higher than observed.

## LIST OF REFERENCES

1. See for example High Electron Mobility Transistors and Heterojunction Bipolar Transistors, ed F. Ali, Artech House, Dedham, MA.(1991); also, Topics in Compound Semiconductors, S. J. Pearton, C. R. Abernathy, and F. Ren, (World Scientific, Singapore 1996)
2. M. Tong, D. G. Balleger, A. Ketterson, E. J. Roan, K. Y. Cheng and I. Adesida, J. Electron. Mater., 21, 9(1992).
3. K. Hikosuka, T. Miamura and K. Joshin, Jap. J. Appl. Phys., 20, L847(1981).
4. S. Salimian, C. B. Cooper III, R. Norton and J. Beam, Appl. Phys. Lett., 51, 1083 (1987).
5. J. -H. Kim, D. H. Lim and G. M. Yang, J. Vac. Sci. Technol., B16, 558 (1998).
6. G. C. DeSalvo, W. F. Tseng and J. Comas, J. Electrochem. Soc., 139, 831 (1992).
7. R. Zhao, W. S. Lao, T. C. Chong and M. F. Li, Jap. J. Appl. Phys., 35, 22 (1996).
8. C. Juang, K. J. Kuhn and R. B. Darling, J. Vac. Sci. Technol., B8, 1122 (1990).
9. D. H. Lim, G. M. Yang, J. -H. Kim and H. J. Lee, Appl. Phys. Lett., 71, 1915(1997).
10. S. J. Pearton, Int. J. Mod. Phys., B8, 1781 (1994).
11. S. J. Pearton, W. S. Hobson, C. R. Abernathy, F. Ren, T. Fullowan, A. Katz and A. Perley, Plasma Chem. Plasma Proc., 13, 311 (1993).
12. K. L. Seaward, N. J. Moll, D. J. Coulman and W. F. Stickle, J. Vac. Sci. Technol., B6, 1645 (1988).
13. K. L. Seaward, N. J. Moll, D. J. Coulman and W. F. Stickle, J. Appl. Phys., 61, 2358 (1987).
14. A. Seabaugh, J. Vac. Sci. Technol., B6, 77(1988).
15. C. M. Knoedler, L. Osterling and H. Shtrickman, J. Vac. Sci. Technol., B6, 1573 (1988).

16. S. J. Pearton, W. S. Hobson, U. K. Chakrabarti, A. B. Emerson, E. Lane and K. S. Jones, *J. Appl. Phys.*, 66, 2137 (1989).
17. C. B. Cooper III, S. Salimian, and H. F. MacMillan, *Appl. Phys. Lett.*, 51, 2225 (1987).
18. S. J. Pearton, U. K. Chakrabarti and W. S. Hobson, *J. Appl. Phys.*, 66, 2061 (1989).
19. A. A. Ketterson, E. Andideh, I. Adesida, T. L. Brock, J. Baillargen, J. Caskar, K. Y. Cheng and J. Kolodzey, *J. Vac. Sci. Technol.*, B7, 1493 (1989).
20. W. H. Guggina, A. A. Ketterson, E. Andideh, J. Hughes, I. Adesida, S. Caracci and J. Kolodzey, *J. Vac. Sci. Technol.*, B8, 1956 (1989).
21. W. Beinstingl, R. Christarell, J. Smoliaer, C. Wirner, E. Gosnik, G. Weimann and W. Schlapp, *Appl. Phys. Lett.*, 57, 177 (1990).
22. M. Joseph, F. E. G. Guimaraes, J. Kraus and F. –J. Tegude, *J. Vac. Sci. Technol.*, B9, 1456 (1991).
23. S. Nahamura, M. Senoh, S. Nagahama, N. Iwasa, T. Yamada, T. Matsushito, H. Kiyoku and V. Sugimoto, *Jap. J. Appl. Phys.* 35, L74 (1996).
24. Y. F. Wu, S. Keller, P. Kozodoy, B. P. Keller, P. Parikh, D. Kapolneck, S. P. De Baars and U. K. Mishra, *IEEE Electron. Dev. Lett.* 18, 290 (1997).
25. M. A. Khan, Q. Chen, M. S. Shur, B. T. McDermott, J. A. Higgins, J. Burn, W. J. Scharff and L. F. Eastman, *Electron. Lett.* 32, 357 (1996).
26. O. Aktas, Z. Fan, S. N. Mohammad, A. Botcharev and H. Morkoc, *Appl. Phys. Lett.* 69, 25 (1996).
27. A. A. Ayon, R. A. Braff, C. C. Lin, H. H. Sawin, and M. A. Schmidt, *J. Electrochem. Soc.*, 146, 139 (1999).
28. R. J. Shul, C. G. Willison, and L. Zhang, *SPIE*, 3511, 252 (1998).
29. R. J. Shul, C. G. Wilson, C. T. Sullivan, S. H. Kravitz, and T. E. Zipperian, *Electrochemical Society Proceedings*, Vol. 98-2, 564 (1998).
30. C. Seung-Bok Lee, S. Han, N. C. Macdonald, *Solid State Sensor and Actuator Workshop*, 45 (June, 1998).

31. P. A. Clerc, L. Dellman, F. Gretillat, M. A. Gretillat, P. F. Indermuhle, S. Jeanneret, Ph. Luginbuhl, C. Marxer, T. L. Pfeffer, G. A. Racine, S. Roth, U. Staufer, C. Stebler, P. Thiegeud, and N. F. de Rooij, *J. Micromech. Microeng.*, 8, 272 (1998).
32. W. D. Lang, *Mat. Sci. Eng. R.*, 17, 1 (1997).
33. See for example <http://www.mdl.sandia.gov/sensors> which gives an overview of microsensor R&D at Sandia National Laboratories (February 1999).
34. H. Jansen, H. Gardeniers, M. de Boer, M. Elwenspoek, and J. Fluitman, *J. Micromech. Microeng.*, 6, 14-28 (1996).
35. C. P. D'Emic, K. K. Chan, and J. Blum *J. Vac. Sci. Technol.*, B10, 1105 (1992).
36. M. Francou, J. S. Danel, and L. Peccoud, *Sensors and Actuators A*, 46-47, 17 (1995).
37. C. Linder, T. Tschan, and N. F. de Rooij, *Transducers*, 91, 524 (1991).
38. G. S. Oehrlein and Y. Kurogi, *Mat. Sci. Eng. R.*, 24, 153 (1998).
39. S. Tachi, K. Tsujimoto, and S. Odukaira, *Appl. Phys. Lett.*, 52, 616 (1988).
40. S. Tachi, K. Tsujimoto, S. Arai, and T. Kure, *J. Vac. Sci. Technol.*, A9, 796 (1991).
41. Robert Bosch GmbH, patents 4,855,017 and 4,784,720 (USA) and 4241045C1 (Germany).
42. J. W. Coburn and E. Kay, *IBM J. Res. Dev.*, 23, 33 (1979).
43. Z. H. Walker and E. A. Ogryzlo, *J. Appl. Phys.*, 69, 548 (1991).
44. Z. H. Walker and E. A. Ogryzlo, *J. Appl. Phys.*, 69, 2635 (1991).
45. S. K. Ghandi, VLSI Fabrication Principles, Si and GaAs, Wiley, New York (1983).
46. C. I. H. Ashby, "*Etching of GaAs: an overview*," in Properties of Gallium Arsenide, third edition, INSPEC, London (1996).
47. R. Williams, Modern GaAs Processing Methods, Artech House, Inc., Massachusetts (1990).
48. H. H. Sawin, "*A Review of Plasma Processing Fundamentals*," *Solid State Technology*, 28 (4), 211-216, (1985).

49. S. J. Fonash, "Advances in Dry Etching – A Review," *Solid State Technology*, 28 (1), 150-158, (1985).
50. D. M. Manos and D. L. Flamm, Plasma Etching: An Introduction, Academic Press, Inc, Boston (1989).
51. C. J. Mogab, "Dry Etching," in VLSI Technology, S. M. Sze, Ed., McGraw-Hill, New York (1983).
52. B. El-Kareh, Fundamentals of Semiconductor Processing Technologies, Kluwer Academic Publishers, Boston (1995).
53. J. W. Coburn, *Plasma Etching and Reactive Ion Etching*, American Vacuum Society, New York, 1982.
54. J. J. Wang, Masters Thesis, University of Florida, 1998.
55. S. Broydo, "Important Considerations in Selecting Anisotropic Plasma Etching Equipment," *Solid State Technology*, (4), 159 (1983).
56. R. W. Berry, P. M. Hall, M. T. Harris, Thin Film Technology, Van Norstrand, New Jersey, 1968.
57. CRC Handbook of Chemistry and Physics, 70<sup>th</sup> Edition, CRC Press, Boca Raton, FL, 1990.
58. C. J. Mojab, *J. Electrochem. Soc.*, 124, 1262 (1977).
59. A. J. van Roosmalen, J. A. G. Baggerman and S. J. H. Broader, Dry Etching for VLSI, Plenum Press, New York, 1991.
60. S. J. Pearton and F. Ren, *J. Vac. Sci. Technol. B*11, 15 (1993).
61. D. L. Flamm, V. H. Donnelly and D. E. Ibbotson, *Basic Principles of Plasma Etching*, in *VLSI Electronics Microstructural Science* (Academic Press, New York 1984) pp. 189-251.
62. M. J. Vasile and F. A. Stevie, *J. Appl. Phys.* 50, 3799 (1982).
63. C. R. Abernathy, *Mat. Sci. Eng. Rep.*, R14 (1995).
64. W. S. Hobson, *Mat. Res. Soc. Symp. Proc.*, 300, 75 (1993).
65. J. Han, J. G. Fleming and D. M. Follstaedt, *Mat. Res. Soc. Symp. Proc.*, 512, 53 (1998).

66. R. J. Shul, S. P. Kilcoyne, M. Hagerott-Crawford, J. E. Parmeba, C. B. Vartuli, C. R. Abernathy and S. J. Pearton, *Appl. Phys. Lett.*, 66, 1761 (1995).
67. W. A. Harrison, Electronic Structure and Properties of Solids, Freeman, San Francisco, 1980.
68. J. W. Lee, J. Hong and S. J. Pearton, *Appl. Phys. Lett.*, 68, 847 (1996).
69. Y. B. Hahn and S. J. Pearton, unpublished work.
70. J. Burm, K. Chu, W. J. Schaff, L. F. Eastman, M. A. Khan, Q. Chen, J. W. Yang and M. S. Shur, *IEEE Electron. Dev. Lett.*, 18, 141 (1997).
71. S. M. Donovan, K. D. Mackenzie, C. R. Abernathy, S. J. Pearton, F. Ren, K. Jones and M. Cole, *Appl. Phys. Lett.*, 70, 2592 (1997).
72. F. Ren, C. R. Abernathy, S. J. Pearton and P. W. Wisk, *Appl. Phys. Lett.*, 64, 1508 (1994).
73. F. Ren, R. J. Shul, C. R. Abernathy, S. N. G. Chu, J. R. Lothian and S. J. Pearton, *Appl. Phys. Lett.*, 66, 1503 (1995).
74. R. J. Shul, G. B. McClellan, S. A. Casalnuova, D. J. Rieger, S. J. Pearton, C. Constantine, C. Barrat, R. F. Karlicek, Jr., C. Tran, and M. Schurman, *Appl. Phys. Lett.*, 69, 1119 (1996).
75. H. Cho, C. B. Vartuli, S. M. Donovan, K. D. Mackenzie, C. R. Abernathy, S. J. Pearton, R. J. Shul and C. Constantine, *J. Electron. Mat.*, 27, 166 (1998).
76. E. L. Muetterties, The chemistry of boron and its compounds, Wiley and Sons, New York, 1967.
77. D. E. C. Cornbridge, Phosphorous: An outline of its chemistry, biochemistry, and technology, Elsevier, New York, 1978.
78. H. J. Emelius, The chemistry of fluorine and its compounds, Academic Press, New York, 1969.
79. M. Stacey, J. C. Tatlow, and A. G. Sharpe, Advances in fluorine chemistry, Vol. 3, Butterworths, Washington D. C., 1961.

## BIOGRAPHICAL SKETCH

David Hays was born in Meridian, MS on December 20, 1968. After graduating from high school in 1988, he joined the United States Navy and served for six years. Soon after being honorably discharged from the military, he enrolled at the University of Florida to begin his college education. David received his bachelor's degree in Materials Science and Engineering in May, 1998 and continued his education as a graduate student. His research included developing selective dry etch chemistries for the GaAs/AlGaAs/InGaP and GaN/InN/AlN semiconductor systems, and developing high etch rate chemistries for Si MEMS processing. He will graduate in August, 1999 with a master's degree in Materials Science and Engineering. He has authored more than 25 technical papers and 2 conference papers, and is a member of TMS, AVS, MRS, and ECS.

